Microwave and optical spectroscopy of 8 and 12 mole % yttria stabilized zirconia

Aypar, Abidin

Aypar, Abidin (1971) *Microwave and optical spectroscopy of 8 and 12 mole % yttria stabilized zirconia*, Durham theses, Durham University. Available at Durham E-Theses Online: http://etheses.dur.ac.uk/8800/

MICROWAVE AND OPTICAL SPECTROSCOPY

OF

8 AND 12 MOLE % YTTRIA STABILIZED ZIRCONIA

by

Abidin Aypar

Presented in Candidature for the Degree of
Doctor of Philisophy
in the University of Durham

December 1971

ACKNOWLEDGEMENTS

The author is deeply indebted to Dr. J. S. Thorp for his supervision and for guidance throughout the work and Professor D. A. Wright for making many valuable suggestions.

A special word of thanks is due to Mr. J. S. Ross with whom he collaborated during part of the work.

The efforts of the Departmental Workshop staff headed by F. Spence are acknowledged with gratitude.

The author also wishes to thank the Turkish Atomic Energy Commission for their financial support.

Finally, my thanks are due to Mrs. A. Robinson who kindly and patiently typed this thesis.

Abidin Aunab.

ABSTRACT

During the work which forms the basis of this thesis, 8 and 12 mole % Yttria Stabilized Zirconia (YSZ) single crystals have been studied from the Electron Paramagnetic Resonance (e.p.r.) and Optical Spectroscopy points of view, in both the as grown state and after current blackening by current passage at several current densities. Experimental factors limited the range of current density used to between 0.1 -5 A/cm^2 for the study of optical spectroscopy and to between 1-25 A/cm^2 for e.p.r.

The e.p.r. study was made at 35 GHz, using a cavity spectrometer, at 293 ^{o}K and 77 ^{o}K. These measurements were difficult because of the low spin densities encountered and because of the cavity damping caused by blackened crystals. They showed in as grown material, the presence of an "F-Centre," (e^- + $(O)^{\bullet\bullet}$ + Y ion). This complex was also seen in blackened crystals. In addition, in both as grown and blackened crystals a second line was observed due possibly to Zr^{3+} or Y^{2+}. A third line, appearing only after current passage seemed to be more likely to arise from conduction electrons than from colour centres or paramagnetic ions.

From optical absorption spectra the band gap energies were calculated to be 4.50 ev and 4.45 ev, at 293 ^{o}K for the 8 and 12 mole % as grown YSZ respectively. Attempts made to fit the absorption curves to the conventional formulae for semiconductors showed that the only near fit was for an indirect allowed transition and this only held for the tail region of the absorption edge. For absorption spectra of differently blackened samples, two methods (transmission-transmission and reflectivity-transmission) were applied at 293 °K. They showed that the absorption curves shifted non-linearly beyond 1.0 micron as compared with the absorption edge position for the as grown samples. An explanation of this is suggested as due to scattering of light from colloidal metallic Zr particles.

From transmission spectra, made at 293 °K for both 8 and 12 mole % as grown YSZ, the Debye temperatures were calculated to be 660 ± 12 °K and 666 ± 12 °K respectively. Reflectivity and refractive index measurements were also made.

Some general conclusions are given.

INTRODUCTION

INTRODUCTION

As will be realized from the general review, previous work on Yttria-Stabilized-Zirconia (YSZ) has been concentrated on the problems related to the determination of the conductivity mechanism, in particular to separating the ionic and electronic contributions to the conductivity and to the temperature, oxygen partial pressure and crystallographic structure dependencies involved.

The magnetic and the optical properties of YSZ have not been studied before. Very few electron paramagnetic resonance (e.p.r.) measurements have been reported up to now, Casselton et al.(1971), perhaps because single crystal material is not readily available and because explanations of the crystalline stability, mechanical and electrical properties are still at an exploratory stage.

In the present work 8 and 12 mole % YSZ as grown and d.c. blackened single crystals were studied by Microwave and Optical Spectroscopy, in order to seek an answer to the nature of the changing character of the current blackened crystals as compared with as grown ones.

The structure on which the thesis was based on can be summarized as follows:

After the presentation of the general review of the previous studies, the first three chapters discuss e.p.r. and the second three the optical properties of YSZ, in both as grown single crystals and d.c. blackened forms. For each group separate chapters give the related background theory, the experimental techniques, and the results and discussions.

The thesis finishes with some general conclusions.

Some of the supplementary experimental data is presented in appendices.

Part of the e.p.r. work was undertaken jointly with another research student, Mr. J. S. Ross.

CONTENTS

GENERAL REVIEW

GENERAL REVIEW

G.1 Historical review of Yttria-Zirconia system

In this general review, we review progress made in the study of Yttria-Zirconia solid solutions since the first discovery by Nerst (1900).

Unstabilized zirconia (ZrO_2) is little used in high temperature technology, as Ruff and Ebert (1929) showed that it undergoes a monoclinic-tetragonal phase change around 1100°C. This problem can be overcome by forming solid solutions with certain recommended stabilizing additives. The addition of these forms cubic modifications which are closely related to the fluorite structure. Examples are Y_2O_3 Duwez et.al. (1951) and CaO Duwez et.al. (1950) etc. (see also review books of Alper (1970), Weber (1964) and Ryschkewitch (1960) for other additives). The cubic stabilized systems so formed do not undergo phase changes such as occur in unstabilized zirconia. We shall return later to the doubts, still not cleared up, about the complete stabilization process and the order-disorder problem.

Chronologically the earliest usage of yttria and zirconia compositions was for observation of the high temperature electrolyte characteristics. This was first observed by Nerst (1900) who qualitatively detected the evolution of oxygen from a rod of composition $(Y_2O_3)_{0.15}(ZrO_2)_{0.85}$. More recently Weininger and Zemany (1954) made quantitative measurements of the electroytic evolution of oxygen and found that 7-80% of the current could be accounted for by ionic conduction depending on temperature, current flow and previous history of the material.

Schottky (1935) discussed the problem of solid electrolytes from the theoretical point of view.

Two years later, Baur and Preis (1937) constructed the first solid oxide-electrolyte fuel cell in the form of a ceramic tube of $(ZrO_2)_{0.85}(Y_2O_3)_{0.15}$, a material which Nerst had previously shown to possess a relatively high ionic conductivity.

Wagner (1943) proposed that oxide solid solutions of the type $(Y_2O_3)_x(ZrO_2)_{1-x}$ contain vacant oxygen ion sites, one vacancy occurring for two Y^{3+} ions substituted for Zr^{4+} ion in the fluorite-type crystal structure. He assumed that this would lead to high oxygen ion conductivity.

Hund (1951) showed the consistency of this oxygen ion vacancy model, for these oxides by correlating X-Ray and pycnometric density data.

Kiukkola and Wagner (1957) have obtained high temperature data using a galvanic cell with an electrolyte of zirconia containing calcia and demonstrated that conduction was purely ionic.

Strickler and Carlson (1964) have estimated the oxygen ion transfer number from the conductivity measurement of a sample of $(Y_2O_3)_{0.09}(ZrO_2)_{0.91}$ as greater than 0.99.

Bray and Merten (1964) have found that maximum electrical conductivity occurs close to the monoclinic-cubic solid solution phase boundary.

Dixon et.al.(1963) and later Strickler and Carlson (1965) showed that the maximum conductivity in M_2O_3 - ZrO_2 solid solutions increased as the ionic radius of the substituted cation was reduced.

Loup et.al. (1965), Anthony (1965) and Foex et.al.(1967) have made several conductivity measurements in the region of composition of the samples used here.

Robert et.al. (1967) showed that the conductivity in several 8 mole M_2O_3 - (Zr, Hf, Th) O_2 solid solutions increased rapidly with decreasing lattice parameter.

Caillet et.al. (1968) suggested the presence of two types of complexes, such as $(2\ Y_{Zr}, Vo)^x$, neutral, and $(Y_{Zr}, Vo)^{\bullet}$, ionized, in order to explain the existence of the two transitions in the Lnσ- 1/T curve.

Casselton (1970a) found that the complexes mentioned above were not inconsistent with the experimental data if concentration dependent mobility due to lattice strains was also considered.

Bauerle et.al. (1969) proposed two mechanisms for the two observed transitions in the Lnσ- 1/T curve for polycrystalline YSZ as "oxygen vacancy trapping by Yttria ions" and "Yttria rich grain boundary conduction."

Casselton (1970a), however, concluded that, according to the comparative measurements made on 8.3 mole % YSZ single and 8.5 mole % YSZ polycrystalline samples, the grain boundary conduction mechanism mentioned above was likely to be insignificant.

Pace et.al. (1969) discuss the crystalline stability of our two kinds of as grown samples. The Debye temperature is around 600°K, derived from the elastic constants extrapolated to 0°K.

Bauerle (1969) showed, by a complex admittance method, the presence of three polarization regions of YSZ. This is also verified in Casselton's articles mentioned below dated

1968 et seq, by Fisher (1970) and by Gokhshtein (1970).

Because of their importance in the present context previous studies on d.c. blackening of YSZ and its consequences are listed briefly below:

Weininger et.al.(1954) pointed out that YSZ shows a characteristic black colour, initiating at the cathode, when high current density is applied.

Karpachev et.al.(1966) and Kleitz (1968) have examined the conditions of blackening.

Jacquin et.al. (1967) explained that the enhanced conductivity during the blackening was due to electronic contribution.

A series of articles by Casselton (1968a, 1968b, 1968c, 1970a) contribute much to our understanding of the black YSZ. Repeated reference is made to them in the text. Casselton postulates that current blackening is due to trapped electrons in anion vacancies, an effect which is similar to that observed when YSZ is heated to a high temperature in vacuum. We shall see in Chapter 3 that e.p.r. results obtained here support these two postulates.

The activation energy drops to a $\simeq$ 0.2 ev for "black" YSZ compared with $\simeq$ 0.7 - 0.9 ev in the "as grown" material which indicates that the pseudo band gap decreases. This is verified by the shift of the absorption edge to higher wavelengths as will be seen in Chapter 6.

Friability and loss of weight have also been reported for current blackened samples. This mechanical weakening is attributed to a structural transformation by Guillou et.al. (1968). Gokhstein (1970) suggests it is due to a monoclinic phase in the cubic structure. On the other hand, Adams et.al.

(1970) report that no monoclinic formation is observed. The lack of observation of the monoclinic phase, if there is any, by X-Ray powder methods may be explained due to the small quantity (less than 5%) of the different structure in the samples, Appendix 1.

G.2 The stabilization problem

G.2.1 Minimum content of yttria for stabilization

Beside the research of the conductivity kind the yttria zirconia system has been the subject of several phase equilibria studies of which the foremost is that of Duwez et al. (1951). According to their data a minimum of 8 mole % yttria is required to achieve complete stabilization of zirconia at a temperature of 2000°C.

Fu-kang et.al.(1963) suggested that the amounts of yttria stabilizer required were very dependent on firing temperature, reporting that 15 mole % yttria is required at 1750°C and a minimum of 7 mole % at 2150°C. These results are in substantial agreement with those of Geller and Yavorsky (1945), Dietzel and Tober (1953) and of Strickler and Carlson (1964).

G.2.2 Structure

Associated with the studies of the determination of the minimum content of yttria needed to stabilize zirconia, two groups of ideas have been developed about the phase of YSZ.

Roth (1956) and Collongues et.al.(1961) have indicated that a pyrochlore phase $Y_2Zr_2O_7$ may exist in the system of yttria-zirconia. However as Y^{3+} and Zr^{4+} have similar scattering factors, the detection by X-Ray techhiques would be most difficult. But Fu-Kang et.al.(1962 and 1963) re-opened the question of the existence of a pyrochlore structure for YSZ. Although Duwez et.al.(1951) and Hund (1951) found no evidence for this system in their phase equilibria studies. The works of Roth (1956) and Stricler and Carlson (1964) have detected a fluorite structure. Lastly Smith (1966) gave convincing evidence for a fluorite-type structure based on neutron diffraction analysis.

Our 8 and 12 m/o YSZ "as grown" and "blackened" crystals have been indexed as fluorite-type structures. The details of the calculations of lattice parameters are given in Appendix 1.

G.2.3 Doubts about complete stabilizations

In the review paper in (1968) Barker discusses the stability of zirconia with M_2O_3 type additives by reference to collected data.

There are two groups of ideas:

1. "The substoichiometric fluorite related phases are formed by the random creation of anion vacancies (Hoch (1964), Hund (1952), Hund (1965), Wagner (1943)). Thus it has been assumed that the cation lattice remains virtually unchanged, that the two or more cation species or single cation species in two valence states are distributed at random and occupy all the normal cation sites and the deviations from stoichiometry are compensated by the random removal of anions from the anions lattice."

2. An increasing number of workers consider the above model to be a grossly oversimplified (Briss et.al.(1967), Roberts et.al.(1967), Bevan et.al.(1965), Hoch et.al.(1967)) because it ignores the effect of interaction between defects. For example, at least one in eight of the anion sites may be vacant in some representative systems in terms of this model (Brisse et.al.(1967), Bevan et.al.(1965), Collongues et.al. (1965)). Even from a simple consideration of electrostatic

repulsion some degree of ordering of these point defects would be expected in order to minimize the interaction of the point charges so created. The true nature of the fluorite-related phases and specifically the structural principle relating the known ordered intermediate compounds, which correspond to a series of closely related arrays of generic formula MnO_{2n-2} Sawyer et al (1965), constitutes one of the major unresolved problems in the field of the solid state chemistry of metal oxide systems.

G.3 The uses of yttria stabilized zirconia

Yttria stabilized zirconia has been widely utilized in various high temperature refractory applications.

Because of their rather unique electrical properties and considerable potential, these stabilized zirconia based solid solutions are also used as solid electrolytes in galvanic and fuel cells Kiukkola et.al.(1957), Weissbart (1962).

Also cubic YSZ makes a promising electrode material for use in Magnetohydrodynamic (MHD) generators. This has been shown by Hepworth et.al.(1963), and arises because ZrO_2, rather than Hafnia for economic reasons, is oxidation resistant, has a high conductivity at 2000°C and low vapour pressure at these temperatures (being in this respect similar to Yttria, Ackermann (1964)) and extending stability down to room temperature.

CHAPTER 1

ELECTRON PARAMAGNETIC RESONANCE (EPR) PHENOMENA

CHAPTER 1

ELECTRON PARAMAGNETIC RESONANCE PHENOMENA

1.1 Introduction

Electron Paramagnetic Resonance (EPR) may be defined as a class of spectroscopic methods for examining fairly localized paramagnetic centres, in our case in a crystalline environment, such that an absorption of energy may be recorded as a function of the strength of an externally applied field, while the microwave frequency is kept constant. The spectra obtained are interpreted in terms of transitions between the energy levels of an Effective spin Hamiltonian which contains parameters relating to the interactions of the centres with their environment. The magnitude and angular dependence of these parametres can give considerable detailed information about the nature of the centre.

From the above it follows that EPR concerns only materials having unpaired electrons. However there are some classes of materials in nature such as transition metal ions, (rare earths) having incomplete d-shells (f-shells) which fulfil this requirement. The experimentally determined EPR data for these materials have been extensively tabulated in three review articles of Bowers and Owen (1955), Orton (1959), Low and Offenbacher (1965) and the books of Pake (1962), Al'tschuler and Kozyrev (1964), since its discovery by Zavoisky (1945).

Apart from transition group ions, electronic dipoles may arise in a number of ways; of these two concern us closely as quoted below.

Point defects, such as an electron occupying a negative ion vacancy (F-centre), or conduction electrons in YSZ as a probable result of the creation of colloidal particles by current passage at high current densities.

A prominent feature of nearly all these cases is that we are dealing with single electrons with just unpaired spin and almost no orbital momentum. The observed g-factor is very close to the free spin value of 2.0023.

In Chapter 3, both as grown and current blackened single crystals of 8 and 12 mole % YSZ have been investigated by EPR and from resulting spectra, interpretation of the parameters in the proposed Effective Spin Hamiltonian has been made. The tensors indicating the Spectroscopic Splitting factor related to the paramagnetic centres are studied and their angular behaviour with respect to the rotation of the applied magnetic field are examined.

Chapter 2 is devoted to the experimental techniques.

In the remainder of this Chapter we shall give the classical basic theory of EPR and then turning to the quantum mechanical approach, we shall mention the interaction energy terms with their forms modified by the strong crystalline field in the total energy Hamiltonian. In particular the usefulness of an effective spin Hamiltonian for describing the energy levels and hence its application concerned to the EPR spectrum will be emphasized, mainly concerned with orbitally quenched $4d^{1,2}$ - palladium group ions to which yttria stabilized zirconia belongs, or s-electrons in the cases of F-centres, conduction electrons etc.

1.2 Free spin in a static magnetic field

The total angular momentum of electrons in crystalline lattices may be considered as almost entirely due to the spins only; because of their quenched orbital angular momentum $\hbar \underline{s}$ and the magnetic dipole moment $\underline{\mu}$ are two coincident vectors which may be written as

$$\underline{\mu} = \gamma \hbar \underline{s} \qquad 1.1$$

where γ is called the magnetogyric ratio and $\hbar$ is Planck's constant divided by 2π.

When we put the crystal in a steady magnetic field $\underline{H}$ unpaired spins will experience a couple which is equal to the rate of change of their spin angular momentum Pake (1962)

$$\text{couple} = \underline{\mu} \wedge \underline{H} = \hbar \frac{d\underline{S}}{dt} \qquad 1.2$$

substituting $\underline{s}$ from equ. (1.1) to (1.2)

$$\frac{d\underline{\mu}}{dt} = \gamma \underline{\mu} \wedge \underline{H} \qquad 1.3$$

This is the so called "equation of motion" of the dipole moment and its solution, $\underline{H}$ being laid along the z-axis of a system of cartesian co-ordinates, represents uniform precession of the vector $\underline{\mu}$ at a fixed angle about a constant vector $\underline{H}$ at a frequency called "Larmor precession frequency" which is given by

$$\underline{\omega}_L = -\gamma \underline{H} \qquad 1.4$$

the negative sign means that the precession is in the direction of a left handed screw advancing along $\underline{H}$ if γ is positive or vice versa.

The component of $\underline{\mu}$ along $\underline{H}$ remains fixed in magnitude so that the energy of the dipole in the field $\underline{H}$ is written classically

$$E = -\underline{\mu} \cdot \underline{H}$$

In terms of the quantum mechanical Hamiltonian the above equation becomes (as we shall see in section 1.8)

$$\mathcal{H} = g\beta H s_{z'} \qquad 1.5$$

Where $\beta = \frac{eh}{2ms}$ is the Bohr Magneton; g is called the "Spectroscopic splitting factor" or more commonly in atomic spectra the "Lande factor," and its value for a free spin is 2.0023; $s_{z'}$ is the component of spin operator $\underline{s}$ along the magnetic field. The eigenvalues of this Hamiltonian are simple, being only multiples $g\beta H$ of the eigen values of $s_{z'}$. Therefore allowed energies are

$$E = g\beta Hm \qquad 1.6$$

where m is the eigenvalue of $\underline{s}$ and takes 2s + 1 values e.g. for an electron s = 1/2 and m = $\pm 1/2$ so only two values are possible. By substituting m values in equ.(1.6) we can find that the two energy levels are separated by an energy of

$$\Delta E = g\beta H \qquad 1.7$$

One should hope to be able to detect the presence of such a set of energy levels by a net energy absorption from an applied external source, if excitation energy is just equal to the energy difference given by equ.(1.7)

$$h\nu = g\beta H \qquad 1.8$$

This is so called EPR resonance condition, where $h\nu$ is the energy quantum of the radiation applied to the crystal.

1.3 The effect of the r.f. field

The application of a rotating magnetic field $\underline{H}_1(t)$ perpendicular to the static magnetic field $\underline{H}$, of the form, Slichter (1963)

$$\underline{H}_1(t) = H_1 (\underline{i} \cos\omega t + \underline{j} \sin\omega t) \qquad 1.9$$

may satisfy the resonance condition given by equ.(1.8) where

$\underline{i}$ and $\underline{j}$ are the unit vectors along the x- and y-axes respectively and ω is the angular frequency of rotating field along the z-axis.

The equation of motion, equ.(1.3), can be written, including the effects both of the $\underline{H}_1(t)$ and of the static field $\underline{H}$

$$\frac{d\mu}{dt} = \mu \wedge \gamma \left[\underline{H} + \underline{H}_1(t)\right] \qquad 1.10$$

In this equation the time dependence of $\underline{H}_1(t)$ can be eliminated by using a co-ordinate system which rotates about $\underline{H}$ with an angular frequency $\underline{\omega}$; in such a reference frame $\underline{H}_1$ will be constant, since the axis of rotation coincides with the $\underline{H}$. $\underline{H}$ will also be constant and equ.(1.10) becomes

$$\left(\frac{d\mu}{dt}\right)_R = \gamma \mu \wedge \left[(H - \frac{\omega}{\gamma})\, \underline{k} + H_1 \underline{i}\right] \qquad 1.11$$

where R is for the reference rotating frame. It may be seen from the comparison of equ.(1.3) and equ.(1.11) that in the rotating frame, the spins process in a cone of fixed angle about an effective static field given by

$$\underline{H}_e = (H - \frac{\omega}{\gamma})\, \underline{k} + H_1 \underline{i} \qquad 1.12$$

at an angular frequency γH_e.

The resonance condition equ. (1.8) can only be satisfied when the rotating field $\underline{H}_1(t)$ has the Larmor precession frequency $\underline{\omega}_e$ and hence the effective field in the rotating frame is just $H_1 \underline{i}$ which produces rotation of μ in the yz-plane, if $\underline{H}_1(t)$ is in the x-direction for example. So far, the classical-mechanical analysis of magnetic resonance has been given. However it is shown by Rabi et.al. (1954) that detailed correlations between the classical and quantum mechanical approaches can be given.

1.4 Transition probabilities

When an oscillating r.f. field $\underline{H}_1(t)$ is applied to the crystal in the plane normal to $\underline{H}$, the system may be expressed by an energy Hamiltonian

$$\mathcal{H}' = \mathcal{H}_0 + \mathcal{H}_1(t) \qquad 1.13$$

where $\mathcal{H}_0$ represents the time independent part of the Hamiltonian given by equ.(1.33) and $\mathcal{H}_1(t)$ is the time dependent term due to the rotation of r.f. field. Since the perturbation is an oscillatory one time dependent perturbation theory is used, as long as $\mathcal{H}' \gg \mathcal{H}_1(t)$ so that the Schrodinger equation of motion becomes

$$i\hbar \frac{\partial|\Psi\rangle}{\partial t} = \mathcal{H}'|\Psi\rangle \qquad 1.14$$

The solution of equ.(1.14) can be found in Abragam and Bleaney (1970), p.99 (and also for the case of $s = \frac{1}{2}$ in Rabi (1937)). It is entirely quantum mechanical and shows that an oscillatory type perturbation $\mathcal{H}_1(t)$ induces transitions between the eigenstates of the system with a transition probability for a spin initially in state $|M\rangle$ to find itself in state $|M\pm1\rangle$ given by

$$\text{probability} = \frac{\pi}{2}(H_1)^2\langle M\pm1|\mathcal{H}_1(t)| M\rangle^2 g(\omega) \qquad 1.15$$

where $|M\rangle$ is the eigen state of the angular momentum operator J_1 and the quantity $g(\omega)$, known as the "shape function" is normalized by the condition

$$\int_0^\infty g(\omega)\, d\omega = 1 \qquad 1.16$$

On the other hand, the radiation theory dictates that since the probabilities of these two opposite processes are equal, the net energy transfer will be zero and no EPR absorption will be available.

From the EPR point of view, the lower lying energy state must therefore be more populated than the other. The Maxwell-Boltzmann distribution law shows that at equilibrium the lower lying state is in fact more populated by a factor

$$N_L/N_U = \exp\,(h\nu/kT) \qquad 1.17$$

than the higher lying state.

The power absorption, per unit volume of the paramagnetic material in the transition from the level M to M′ is obtained Al'tschuler and Kozyrev (1964)

$$\text{Power} \propto (N_M - N_{M'})(\gamma H_1)^2 \langle M' | \mathcal{H}_1(t) | M \rangle^2 g(\omega) \qquad 1.18$$

Since the static magnetic susceptibility (Van Vleck (1932)) is

$$\chi_0 = \text{const.}\ (N_M - N_{M'}) \langle M' | \mathcal{H}_1(t) | M \rangle^2$$

equ.(1.18) becomes

$$\text{Power} \propto \chi_0 (\gamma H_1)^2 g(\omega) \qquad 1.19$$

The study of the behaviour of substances in steady magnetic fields is characterised by the static susceptibility. However, using also the time dependent magnetic field $H_1(t)$ allows us to define a complex susceptibility

$$\chi = \chi' - i\,\chi'' \qquad 1.20$$

That, part of the magnetization which changes in phase with the field is determined by the dynamic susceptibility χ', while the absorption of the energy, from the periodic field by the paramagnetic sample, is determined by χ''. The general relation between χ' and χ'' is given by the Kramers-Kronig equations Kramers (1927), Kronig (1926). These dispersion formulae give a relation between the magnitude of χ'' and the line shape function $g(w)$.

$$\chi(w) = \text{const.}\chi_0\, g(w) \qquad 1.21$$

As has been mentioned before the shape function is found experimentally to be either a Gaussian or a Lorenzian type function.

By the comparison of equ.(1.19) and equ.(1.21) the power absorbed by the sample may be written as

$$\text{Power} = \text{const.}\ \chi'' \qquad 1.22$$

On the other hand in experiments, a curve for the dependence of the derivative form of absorbed power $\propto \frac{d\chi''}{dH}$ on static magnetic field $\underline{H}$ is recorded.

1.5 The crystal field

When a paramagnetic ion is inserted into a crystalline structure its free ion energy levels are modified due to the environmental interactions. Ideally it is hoped to solve the Schrodinger equation for the ions of the entire crystal, this of course is not yet possible. However, there are some theories e.g. "crystal field theory" which can suggest solutions on the lowest and the excited energy levels of an ion situated in a crystal of a given symmetry and modified by the crystalline surroundings.

Crystal field theory gives a model which is quite good for rare earth salts, but for 3d electrons and even more 4d or 5d electrons, the model is incomplete.

The crystal field theory assumes that the paramagnetic ion resides in a crystalline electric potential whose sources are point charges, lying wholly outside the paramagnetic ion.

Interaction with this additional potential is thus added to the Hamiltonian of the free ion in order to find the modified new energy levels. The crystalline field should have the symmetry of the array of ligand ions and this symmetry determines the properties of the paramagnetic ionic energy states. The group theoretical methods have served as useful techniques for analyzing this problem since Bethe (1929) introduced them.

We shall not go into the details of surveying group theory, calculation of the energy states and ground state properties of paramagnetic $4d^1$, $4d^2$ ions or special case of ions, s-electrons, for F-centres. There are several reasons for this.

1. In Yttria stabilized zirconia crystals, the paramagnetic ions might be Zr^{3+}, Zr^{2+}, Y^{2+} for which no specific theoretical work has been done, even more so for experiments. The only theory has been given for some 3d and 4d, 5d ions in strong crystal fields, is generally applied to other ions.

   Chronologically the paramagnetic properties of the iron group cyanides in terms of a strong ligand field was first given by Van Vleck (1935). The contributions from the orbital magnetic moments, including the effect of spin-orbit splitting, were calculated by Kotani (1949) for octahedral symmetry. The theory was extended by Kamimura (1956), Bleaney and O'Brien (1956), Kotani (1960), Tanabe (1960) and Sugano (1960) and, especially for 4d, 6d ions, by Kamimura et.al.(1960).

2. The effective spin Hamiltonian, which is used to describe EPR experiments, can often be used to make

predictions from the simple symmetry and physical considerations without knowing the detailed crystal field calculations.

The effective spin Hamiltonian is introduced in section (1.7). We shall write down for resonance experiments an effective spin Hamiltonian containing only the spin operators. The inclusion of certain kinds of interaction terms, magnitudes and angular dependence of these interactions may be determined by the experiment. This is given in section (1.8).

1.6 Basic interactions and total Hamiltonian of free ion

We will now concern ourselves only with the interactions which are well known from the atomic spectroscopy Racah (1942a, 1942b, 1943) within the free ion. The interaction terms will be considered in order of diminishing interaction energies in the Hamiltonian and the ligand interaction (strong crystal field) will be introduced at the appropriate point as a sequence of interactions, internal to the paramagnetic ion.

1. Electronic energy (10^5 cm^{-1}, optical region)

This arises from interaction of an electron with the coulomb field of the nucleus modified by the repulsive field of the other electrons. In the non-relativistic approximation it is given by

$$\mathcal{H}_1 = \sum_i P^2/2m - \sum_i Ze^2/r_i + \sum_i e^2/r_{ik} \qquad 1.23$$

with a suitably averaged electronic field with central symmetry. This Hamiltonian results in the electronic levels being grouped into configurations. For example a ground configuration $3d^3$ lies 10^5cm^{-1} below the first excited configuration $3d^2 4s$. The resultant mutual electrostatic repulsion of the electrons, give rise to Russells-Saunders coupling.

2. Crystal field energy, $\mathcal{H}_2$, ($10^4 cm^{-1}$ infrared or optical region

4d-electrons are valence electrons for which the ligand interaction is much stronger than the spin-orbit coupling (Hund's rule is not obeyed). In the strong ligand field limit single electron states must be used, giving splittings large compared with those due to the spin orbit coupling. The electrostatic crystal field and spin-orbit coupling within the atom are included subsequently. 4d ligand complexes have, most predominantly, cubic symmetry and have interaction energies of $\simeq 10^4$ cm^{-1} or more. The residual parts of the ligand interaction, representing departures from exact cubic symmetry are smaller in magnitude ($\simeq 10^2$ to 10^3 cm^{-1}) and their effects are often considered as the spin-orbit interactions.

3. The next important interactions are magnetic in origin. The coupling between the electron spins $\underset{\sim}{s}_i$ with the orbital momentum $\underset{\sim}{l}_j$ can be expressed as

$$\mathcal{H}_3 = \sum_{ij} (a_{ij}\underset{\sim}{l}_j\cdot\underset{\sim}{s}_i + b_{ij}\underset{\sim}{l}_i\cdot\underset{\sim}{l}_j + c_{ij}\underset{\sim}{s}_i\cdot\underset{\sim}{s}_j) \qquad 1.24$$

where a_{ij}, b_{ij}, c_{ij} are constants. The first term is the so called spin-orbit coupling. In the strong crystal field limit, our formula must be expressed in terms of single electron states, for example:

$$\mathcal{H}_{3a} = \zeta\ (\underset{\sim}{l}\cdot\underset{\sim}{s}) \qquad 1.25$$

The third term is for spin-spin interactions, which was first considered by Pryce (1950) and for which one possible form is

$$\mathcal{H}_{3b} = \sum_{i>j} 4\beta^2 \left\{ \frac{s_i \cdot s_j}{r_{ij}^3} - \frac{3(\underline{r}_{ij} \cdot \underline{s}_{ij})(\underline{r}_{ij} \cdot \underline{s}_{ij})}{r_{ij}^5} \right\} \qquad 1.26$$

This plays a small but not altogether insignificant role in some magnetic problems (interaction energy is usually < 1 cm^{-1}).

4. Hyperfine interaction (0-10^{-2} cm^{-1})

If the nucleus has a spin $\underline{I}$, the hyperfine interaction is given by

$$\mathcal{H}_4 = 2\gamma_N \beta \beta_N \left[\sum \left\{ \frac{(\underline{l}_i - \underline{s}_i)\cdot \underline{I}}{r_i^3} + \frac{3(\underline{r}_i \cdot \underline{S}_i)(\underline{r}_i \cdot \underline{I})}{r_{ij}^5} \right\} + \frac{8\pi}{3} \delta r_i (\underline{s}_i \cdot \underline{I}) \right] \qquad 1.27$$

where β_N and γ_N refer to the nuclear magneton and nuclear gyromagnetic ratio. In the strong field considerations the above equation is reduced to

$$\mathcal{H}_4 = 2\beta \left({}^{\mu_I}/\underline{I} \right) \langle r_c^{-3} \rangle \left(\sum_i \underline{I} \cdot \underline{S}_i \right) = \underline{S} \cdot \underset{\sim}{T} \cdot \underline{I} \qquad 1.28$$

because of the cases for orbitally quenched or s-electrons for which the spin density outside the nucleus has spherical symmetry which is only found for $l = 0$, where $\langle r_l^{-3} \rangle$ is a measure of the spin density at the nucleus. This "contact" interaction is due to unpaired s-electron spin density and arises due to exchange interaction of unfilled shell electrons with filled ones. This term can also contribute to the hyperfine structure splitting of F-centres.

5. Quadrupole energy (0-10^{-2} cm^{-1})

The electrostatic interaction of the quadrupole moment with the nuclear moment of the nucleus will contribute an additional energy given by

$$\mathcal{H}_5 \quad \frac{e^2 Q}{2\underline{I}\cdot(\underline{I}+1)} \left[\sum_i \frac{\underline{I}(\underline{I}+1)}{r_i^3} - \frac{3(\underline{r}_i \cdot \underline{I})^2}{\underline{r}_i^5} \right] \qquad 1.29$$

Up to now we have considered the interaction energy terms in the absence of the external steady magnetic field. However if we go on in the foregoing non-relativistic treatment and introduce magnetic field we would not come across any term for the spin magnetism, when the Hamiltonian is derived. Relativistic corrections given by Dirac (1930) for the kinetic energy of the electrons can only give the interaction terms of orbital and spin magnetic moments with the magnetic field.

6. Spin-Zeeman energy (0-1 cm^{-1})

In the strong ligand field limit, the Spin-Zeeman interaction energy term is given by

$$\mathcal{H}_6 = \beta \underline{H} \cdot \sum_i (\underline{l}_i + g_s \cdot \underline{s}_i) \qquad 1.30$$

where the sum is over all electrons in partly-filled shells and where g_s is the free spin g-value. In the d-group, the strong cubic ligand field "quenches" the orbital momentum partly when it leaves an orbital triplet as the ground state and the magnetic effects are due almost entirely to the spin degeneracy remaining in this state. These statements are valid for $4d^1$ and $4d^2$ and even more so for s-electrons in F-centres. In the spin Hamiltonian the term

$$\mathcal{H}_{6a} = \beta \underline{H} \cdot \underset{\sim}{g} \cdot \underline{S} \qquad 1.31$$

is used which considers the local symmetry as well as the magnetic field. The shift from g_s is attributed to the orbital contribution to the spin.

7. Nuclear-Zeeman energy (0-10^{-3} cm^{-1})

Direct interaction of the nucleus with the external magnetic field $\underline{H}$ is given by

$$\mathcal{H}_7 = \gamma_N \beta_N \underline{H} \cdot \underline{I} \qquad 1.32$$

The general Hamiltonian describing the paramagnetic ion can be written considering all the above possible interactions together

$$\mathcal{H} = \mathcal{H}_1 + \mathcal{H}_2 + \cdots\cdots \qquad 1.33$$

The calculation of energy eigen values and then eigen functions of the total Hamiltonian $\mathcal{H}$ is found following perturbation theory which gives an approximate value but is still very complicated. The computation of the resulting eigen functions becomes complicated because of the mixture of ground and excited states after the third and fourth perturbations.

1.6 Effective Spin Hamiltonian

Abragam and Pryce (1951) however developed a perturbation method to calculate the energy splittings of the ground level of a paramagnetic ion. —

In their opinion, the ground level of the free ion is so far separated from the higher energy levels that EPR may be expected between $2s' + 1$ energy levels of the ground level which could only be responsible for EPR. The quantity s' is called, the "effective spin" which describes the system in its ground state; it may or may not be equal to the free ion spin quantum number, s. —

The general Hamiltonian, constructed in the previous section, may be shortened to the form of

$$\mathcal{H} = \underline{S}\cdot\underset{\sim}{D}\cdot\underline{S} + \beta\underline{H}\cdot\underset{\sim}{g}\cdot\underline{S} + \underline{S}\cdot\underset{\sim}{T}\cdot\underline{I} + \mathcal{H}_5 + \mathcal{H}_7 \qquad 1.31$$

The first term represents splittings due to crystal fields and was introduced by Van Vleck (1940). The operators referring to $\underline{S}$ and $\underline{I}$ are treated as non-commuting algebraic quantities. An expression involving the components of operators is called the "Spin Hamiltonian" and the energy levels can then be derived as the eigen values of this operator.

The Spin Hamiltonian has been obtained on entirely theoretical grounds and is used to give an shorthand formulation of the experimental results. If the tensoral parameters, that is, the g-factor, the initial splitting D, and hyperfine structure constant $\underline{T}$ etc. are measured experimentally, they can then be used to find a model of a crystal field and also to calculate the energy levels of the ion.

The Hamiltonian equ.(1.31) is reduced to the simple form of

$$\mathcal{H} = \beta \cdot \underline{H} \cdot \underset{\sim}{g} \cdot \underline{S} \qquad 1.32$$

because of our observed EPR spectra and the following reasons

1. The term S D S = 0 for $4d^{1}$, $S = \frac{1}{2}$ (for Y^{2+}, Zr^{3+})
2. The last three terms are also zero because there was no hyperfine interaction, quadrupole (Q = 0 for both yttrium and zirconium nuclei) interaction and nuclear Zeeman interaction.

The Hamiltonian equ.(1.32) is also valid for F-centres Markram (1966) and for conduction electron spin resonance see Yafet (1963).

As we have seen in the previous sections the unknown tensoral parameter $\underset{\sim}{g}$ in equ.(1.32) depends on the magnitude and symmetry properties of the crystalline electric field. It therefore follows that a more general form, which takes into account "anisotropy" of this kind is expressed by equ. (1.32) which is shorthand notation for

$$\mathcal{H} = \beta(g_{xx}H_x s_x + g_{yy}H_y s_y + g_{zz}H_z s_z$$
$$+ g_{xy}H_x s_y + g_{yx}H_y s_x + g_{yz}H_y s_z$$
$$+ g_{zy}H_z s_y + g_{zx}H_z s_x + g_{xy}H_x s_y) \qquad 1.33$$

The quantities $g_{xy} = g_{yx}$,..... etc. The off-diagonal elements of the g-tensor can then be eliminated by a co-ordinate transformation of the (xyz)-axes to (x'y'z')-axes system, (known as the principal axes), yielding a simpler form for equ.(1.33).

$$\mathcal{H} = \beta(g_{x'x'}H_{x'}s_{x'} = g_{y'y'}H_{y'}s_{y'} + g_{z'z'}H_{z'}s_{z'}) \qquad 1.34$$

If the magnetic field H is applied in a direction with cosines (l, m, n) with respect to these principal axes, the energy levels are given by equ.(1.6) with a g-value of

$$g^2 = l^2 g^2_{x'x'} + m^2 g^2_{y'y'} + n^2 g^2_{z'z'} \qquad 1.35$$

The resonance condition is again given by equ.(1.8).

1.8 Application of the effective Spin Hamiltonian

The local symmetry may be cubic in which case g-factor is isotropic $g_{x'x'} = g_{y'y'} = g_{z'z'}$. It may be axial in which case the spectrum axially symmetric in the plane perpendicular to the field direction, i.e. $g_{x'x'} = g_{y'y'} = g_{\perp}$, and $g_{z'z'} = g_{\parallel}$. Where $g_{\parallel}$ and $g_{\perp}$ are the components of g when H lies along and perpendicular to the crystal field direction.

Bleaney (1951) has given formulae for the angular dependence of the Hamiltonian for the case of axial fields. The Hamiltonian given by equ.(1.34) takes the form of

$$\mathcal{H} = g\beta H s_{z'} \qquad 1.36$$

The energy levels are simply given by $\pm\frac{1}{2}g\,H$, where

$$g = (g_{\parallel}^{2}\ \cos^{2}\theta + g_{\perp}\sin\,\theta)^{\frac{1}{2}} \qquad 1.37$$

and θ is the angle between H and the axial crystal field direction.

Consequently, in a crystal whose symmetry axis is known or seen by eye (e.g. c-axis of Ruby), the spectroscopic splitting factor-g given by equ.(1.37) may be determined from the observed spectra along and normal to the symmetry axis. If, however, the symmetry axis is not known it is necessary to observe the EPR spectra in some different planes, say (100)-planes, so that, the anisotropy in g can be examined with respect to the rotation angle of the applied magnetic field and as a result, their principal values may be found.

Guesic and Brown (1958) give a straightforward method for obtaining the principal components and principal axes of the g-tensor for $S = \frac{1}{2}$, $I = 0$; this can perfectly be applied to analysis of our spectra, as will be outlined below in short.

It can be shown that experimental g(exp)-values in three different planes about (xyz)-axes for a given (xyz) orthogonal crystalline co-ordinate system, for the magnetic field directions making angles ϕ_x, ϕ_y, ϕ_z with the y, z, x axes respectively are related to the nine components of the (g^2)-tensor, which is going to be diagonalized, as given below.

$$g(\exp)^2 = (\underset{\sim}{g}^2)_{yy}\mathrm{Cos}^2\phi_x + (\underset{\sim}{g}^2)_{zz}\mathrm{Sin}^2\phi_x + 2(\underset{\sim}{g}^2)_{yz}\mathrm{Cos}\phi_x\mathrm{Sin}\phi_x$$
$$g(\exp)^2 = (\underset{\sim}{g}^2)_{zz}\mathrm{Cos}^2\phi_y + (\underset{\sim}{g}^2)_{xx}\mathrm{Sin}^2\phi_y + 2(\underset{\sim}{g}^2)_{zx}\mathrm{Cos}\phi_y\mathrm{Sin}\phi_y$$
$$g(\exp)^2 = (\underset{\sim}{g}^2)_{xx}\mathrm{Cos}^2\phi_z + (\underset{\sim}{g}^2)_{yy}\mathrm{Sin}^2\phi_z + 2(\underset{\sim}{g}^2)_{xy}\mathrm{Cos}\phi_z\mathrm{Sin}\phi_z$$

1.38

The corresponding matrix $(\underset{\sim}{g}^2)$ can then be diagonalized in order to obtain the principal components of $(\underset{\sim}{g}^2)$. The square roots of these components give the principal components of the g-tensor. The direction cosines of the principal components can also be given with respect to the reference frame (xyz).

CHAPTER 2

EXPERIMENTAL TECHNIQUES

CHAPTER 2

EXPERIMENTAL TECHNIQUES

2.1 Introduction

The single crystals of 8 and 12 mole % YSZ used in our EPR and optical experiments were grown by W.& C. Spicer Ltd., using electrofusion methods. The starting material was the mixture of the pure powdered oxides.

In the following subsections the preparation of the samples and the EPR techniques used are studied.

2.2 Crystal preparation

2.2.1 Crystal orientation and cutting process

As will be seen in Chapter 3, in order to determine the principal magnetic directions for an observed EPR spectrum and relate them to the crystallographic axes one needs samples to be oriented and cut appropriately.

The as grown 8 and 12 mole % YSZ crystals varied in appearance from transparent yellowish brown to black and almost opaque. They were attached with durofix to the goniometer. Orientation determinations were carried out using X-Ray back-reflection methods. Exposures were about 30 minutes, using copper radiation without a filter and Ilford "Industrial G" X-Ray film. The normal procedures were followed in order to develop the films. The positions of the required direction were obtained to within $\pm 1^{\circ}$. The photographs taken in the (100), (111), (110) were similar for both kinds of YSZ. From these series of photographs the following conclusions were derived.

1. Both the two single crystals have got nearly perfect structure.
2. Evidence for a cubic structure, additional to the powder photo results was obtained.

The samples were cut with a diamond wheel cutting machine, without causing fragmentation, as cubes having (100) surfaces. Long rod samples (1 x 1 x 10 mm^3) were also prepared for several current blackening, vacuum reduction or heat treatment processes.

2.2.2 Purity of the samples

The presence of certain impurities in the material, which could exert a profound influence on particular properties, might result in an incorrect interpretation being made. For this reason several analysis results of both as grown YSZ crystals are listed below.

1. Qualitative spectroscopic analysis was performed by R. A. Mostyn and Dr. Conduit, Chemical Inspectorate, Headquarters Building, Royal Arsenal, Woolwich, London, S.E.18. The results are shown in Table (2.1).

TABLE (2.1)

major	zirconium
minor	yttrium
heavy trace	silicon, hafnium 0.01%
trace	magnesium, tin

2. The quantitative X-Ray Fluorescence analysis for certain trace elements, made by Dr. Holland, Durham University, Department of Geology, is given in Table (2.2).

TABLE (2.2)

Elements sought	8 m/o YSZ (ppm)	12 m/o YSZ (ppm)
lead	0	0
nickel	760	990
copper	not detected	not detected
zinc	25	27
strontium	not detected	not detected
manganese	150	150
rubidium	not detected	not detected
chromium oxide	45	384

3. On the other hand, twenty-six zirconias from different places of the world including the Spicer Ltd. products, from where we purchased our experimental crystals, had been examined with emission mass spectroscopic and chemical analysis Heffelfinger et.al. (1964). The elements detected at more than 10 ppm are shown in Table (2.3).

TABLE (2.3)

Elements:	Al	Ba	Ca	Hf	k	Mg	S	Si	Ti
(ppm) :	30	30	100	2200	50	20	30	20	300
Elements:	N	Ne	Cl	Se	Ta				
(ppm) :	60	30	15	40	300				

Comparison of the analysis results given above leads to the following conclusions.

Because Table (2.3) excludes the analysis for yttria, we cannot compare its results directly with Tables (2.1) and (2.2). However they are in substantial agreement. On the other hand, comparison of Tables (2.1) and (2.2) is not also possible: because the elements sought are not the same. So we should consider all three analysis results.

2.2.3 The current passage process

The current passage treatment was carried out in a vertical tube furnace. The silica glass tube which contained the fixed sample assembly was inserted and clamped in the hottest zone.

The samples, of (1 mm)^2 cross-section and approximately 10 mm long, were attached to the platinum wire electrodes with platinum paste. Wet argon gas was directly applied to the silica tube and at the exit end the gas was bubbled through silicone liquid, to prevent air backstreaming into the apparatus.

The temperature was measured with a Pt-12% Rh thermo couple. The d.c. currents between 10 mA (1 A/cm^2) and 250 mA (25 A/cm^2) were passed at a fixed temperature of 800^{o}C, which was controlled to within $\pm 5^o$C, for times ranging from 3 minutes to 1 hour.

When the current passage process was finished the current leads and thermocouple wires, the pipe of the argon gas and clamps etc. were disconnected and the silica tube was immediately withdrawn out of the furnace. Both ends of the tube were then closed so that the sample was left to cool down, dropping to a temperature of 400^{o}C in two minutes.

After current passage the crystals became very friable. A silvery conducting layer was observed which had been reported to be due to creation of zirconium oxynitride Casselton (1968a) and as has been suggested by Loup et.al. (1965) it was not an essential product of blackening. The silvery conducting layer was removed by boiling in phosphoric acid for a few minutes at around 70^{o}C. This process was repeated several times to improve the Q-quality factor of the cavity when loaded with a blackened sample.

The crystals heat treated in oxygen turned white and translucent and also showed cracking. Detailed heat treatment results under several temperature conditions and oxygen flow rates are given in Appendix 2.

2.3 Electron paramagnetic resonance techniques

In the previous chapter we mentioned an energy absorption between the energy levels of a paramagnetic sample excited by microwave radiation in a steady magnetic field. In order to perform this in practice, the basic components which we may need are: first a microwave energy source (klystron) of the correct frequency range, secondly a cavity which concentrates this energy onto the sample and thirdly a detection system which will detect the amount of absorption and then display this as the spectra of the paramagnetic centre.

The resonance condition given by equ.(1.8) is satisfied in practice as a display of energy absorption spectrum by keeping the microwave frequency constant and changing the magnetic field slowly. In other words, the EPR spectrum can be obtained graphically by plotting the changes in absorbed microwave energy which appears as the output of the detecting system versus d.c. magnetic fields $\underline{B}$, (say in Tesla).

The block diagram of the Q-Band spectrometer used during the course of this work is shown in Figure (2.1).

The power reaches the cylindrical cavity, which has been designed for the TE_{012} mode, from a klystron. This cavity, which contained the sample under investigation, could be tuned in each of two ways; coarse, which is produced by changing the length of the cavity and fine, which is produced with a quartz rod controlled from the top of the waveguide assembly by means of a micrometer so that there is a minimum reflection of the microwave energy in the absence of a d.c. applied magnetic field. The vertical movements of the tapered teflon (which was controlled by means of a micrometer similar to that used for the quartz rod and positioned just above the cavity-waveguide coupling hole), were also effective in reducing these reflections.

When the magnetic field is applied and varied slowly through the point at which EPR occurs there is a small change in the reflection from the cavity, i.e. a net absorption of energy by the sample. To detect this change, an a.c. modulation field at 160 kHz, which is necessary for the display of a permanent spectrum on a CRO or to record on a chart, is superimposed with the applied magnetic field. As the magnetic field passes through the resonance points, the detecting system receives a signal, at 160 kHz, which is amplified and compared in phase with the original waveform using a phase shifter, and phase sensitive detector. The resulting first derivative form of power absorption $\propto \frac{d\chi''}{dB}$ of the paramagnetic sample versus magnetic field, B, is recorded on the X-Y chart recorder as an EPR spectrum.

2.3.1 Determination of the crystal orientation in the cavity

In order to know the orientation of the crystal in the cavity under EPR conditions and to relate this to the external magnetic field direction, a two stage process was applied.

In the first stage involved relating the crystal orientation, e.g. [100], to the small, angles engraved on a brass cavity scale which was firmly attached to the plunger of the cavity, functioning as an alignment aid. A travelling

Fig. (2.1)

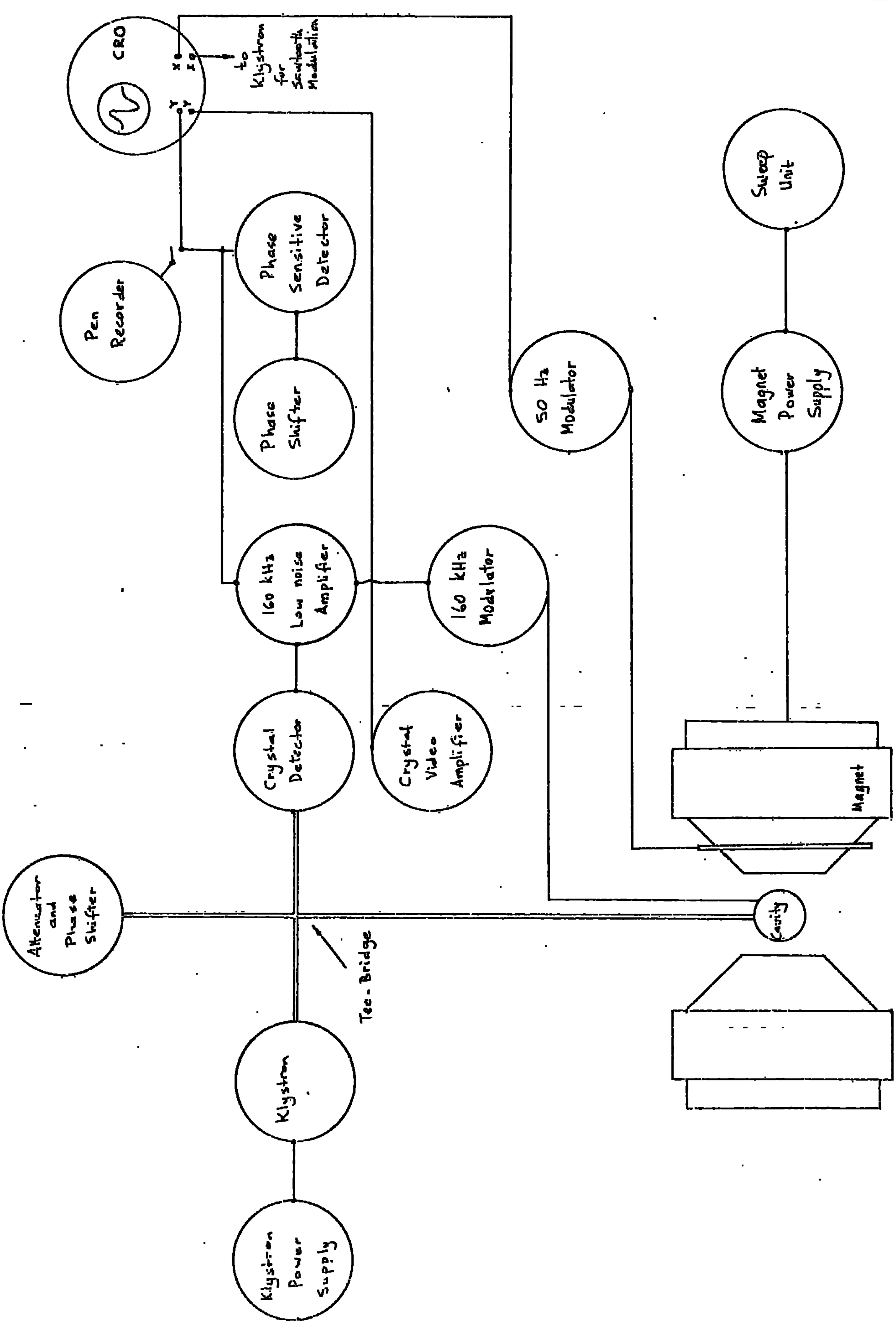

Fig. (2.1) Block Diagram of the Q-Band EPR Spectrometer.

microscope with a large depth of focus was used for this. One of its cross wires was first set parallel to the direction of travel using a sheet of graph paper. Employing the cross wire and choosing a particular face of the crystal, two readings differing by 180^{o} read from the scale.

The plunger assembly was then inserted into the microwave cavity barrel and tuned for the EPR condition.

The second stage involved relating the cavity scale of the plunger to the turntable of the magnet. This was done by using a piece of fine twine stretched underneath the plunger, its ends being terminated at fixed points. Two more scale readings differing by 180^{o} were obtained from the datum line. In a previous experiment, the datum line (stretched twine) had been related to the magnet scale reading as M_o being parallel to the pole pieces.

In Appendix 3, a derivation of the conversion formula is given between the two scales being used in the determination of the crystal orientations versus external magnetic field directions for EPR polar plots.

Uncertainty on the alignment of the magnetic field along a given crystal direction was about less than 2^{o}.

2.3.2 Measurement of magnetic field value

The measurement of magnetic field value at resonance could easily be made by using the g-marker, the DiPhenyl Picryl Hydrazyl (DPPH) as a reference in conjunction with the calibrated sweep; accordingly DPPH was always mounted within the cavity beside the sample under investigation. For an accurate g-value Al'tschuler and Kozynev (1964), Chapter 7, may be consulted.

The X-Y recorder graph papers were calibrated for several sweep amplitudes and sweep times in the magnetic field range that the EPR Spectra of YSZ occurred. All the EPR recordings were made at a 11.3 mT in^{-1} (113 gauss in^{-1}) sweep rate with 100 % sweep amplitude and a 2 minutes sweep time. This conversion factor helped for the measurements of the magnetic field value of line since reading the distance between the standard DPPH and the position where the EPR spectra were recorded was easy. The measurement of the microwave frequency, with a wavemeter by the help of calibration chart, coupled with this absolute magnetic field value allowed the g-factor to be calculated.

2.3.3 Sensitivity of the spectrometer

In order to estimate the sensitivity of the Q-band spectrometer, a ruby crystal (0.05% Cr_2O_3 in Al_2O_3) was used as a calibrator. The sensitivity was calculated following the formula given by Assenheim (1966), p.76.

$$\text{sensitivity} = \frac{(\text{no. of spins}) \times (\text{power})^{\frac{1}{2}} \times (\text{time constant})^{\frac{1}{2}}}{(\text{line width}) \times (\text{signal to noise ratio})}$$

The sensitivity was calculated from the following experimental conditions:

no. of Cr^{3+} spins	:	1.58×10^{16}
power	:	10.6 mW
time constant	:	3 sec
line width	:	1407 Am^{-1} (at sweep amplitude 10%)
signal to noise ratio	:	3×10^3

So the sensitivity becomes of the order of 2×10^{12} spins per mT for a power of 1 mW with a time constant of 1 sec.

2.3.4 The low temperature experiments

In order to perform the EPR spectrum down to liquid nitrogen temperature (77 °K) the dewar assembly is fixed to the permanently mounted rack above the magnet.

After sticking the thermocouple wire to the same level as the sample, the cavity assembly was inserted into a stainless steel can whose top end was then covered with selotype in order to ensure that when the nitrogen was poured into the inner helium space of the crystostat, none entered the cavity.

The inter space of the dewar was evacuated with a diffusion pump and the pressure was monitored with vacustat gauge. The temperature was monitored with a constanten-copper-constanten thermocouple using a potentiometer.

CHAPTER 3

EPR EXPERIMENTAL RESULTS AND DISCUSSIONS

CHAPTER 3

EPR EXPERIMENTAL RESULTS AND DISCUSSIONS

3.1 Introduction

Most of the EPR experiments have been made at room temperature with some at liquid nitrogen temperatures ($77^{o}K$). The frequency was 35.5 GH_z and the spectrometer employed 160 kHz modulation, using a phase sensitive detection system as outlined in Chapter 2. The sweep amplitude and time constant were 100% and 2 minutes respectively.

The angular variations, intensities and line shapes of the observed resonance patterns were characterised by three types of line.

For as grown crystals two types of EPR spectra were recorded: "type-A" and "type-B". Current blackened specimens showed an extra isotropic line called "type-C."

The type-A lines were anisotropic and symmetrical. Four lines were seen in some directions. The lines were less intense than and on the higher magnetic field side of the type type-B line. The anisotropy shows that these centres are located in a distorted tetrahedron having a crystalline field along a [111] body diagonal direction of the unit cell. Also, comparison of the effects of annealing and d.c. blackening, vacuum reduction and oxygen heat treatment strongly suggested that type-A lines are due to free electrons trapped in oxygen ion vacancies (F-centres). The centres disappeared after the crystals had been stored several months.

Type-B line: this was slightly anisotropic and asymmetrical. It was uneffected by heat treatments in argon, air or oxygen atmospheres. The periodicity of the anisotropy indicates the existence of distorted oxygen ligands with seven-fold and six-fold co-ordinations. For assignment several possibilities are discussed. Either Y^{2+} or Zr^{3+} or both seem more likely.

Type-C line: this was isotropic and almost overlapped the type-B line. An intensity increment was observed with increasing applied d.c. current density.

No extra spectra or change of the ones recorded at 290 °K were observed at 77 °K.

3.2 Crystal structure - EPR

The crystal structure of YSZ is based on a f.c.c. unit cell and described by the space group Fm3m. However, there are two subunits which may be the basic units in the EPR study, see Figure (3.1).

1. Tetrahedral (space group T_d^2)
   Ligand (metal) ions at alternate corners are missing so that ligands form a regular tetrahedron.
2. Cubic (space group O_h^5)
   Eight oxygen ions being at the corners form a regular cube.

However, in practice, it is found that the cubic oxygen symmetry is distorted due to the charge compensation. Barker's (1967) statistical analysis on yttria stabilized zirconia showed that seven-fold and six-fold oxygen co-ordinations (one or two corners truncated from cubes) are the most likely symmetries. In the latter case two adjacent oxygens are missing which gives rise to octahedral symmetry.

Fig.(3.1) Two possible co-ordinations of anions and cations in fluorite structure.

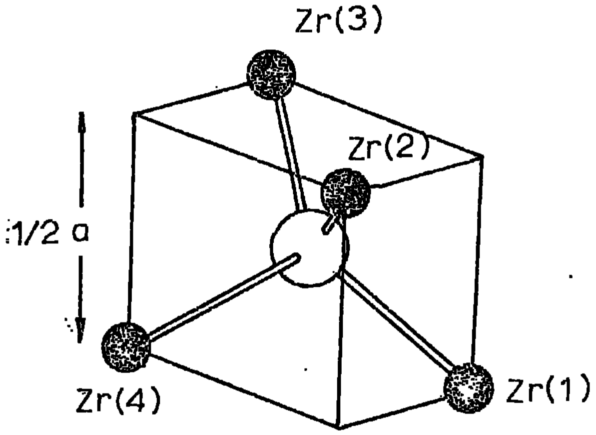

TETRAHEDRAL

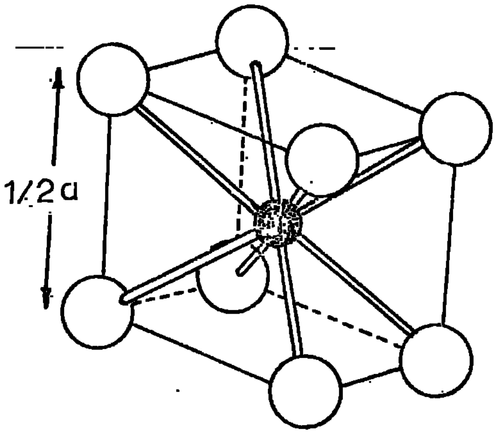

CUBIC

Fig.(3.1) Two possible coordinations of anions and cations in fluorite structure.

● CATION(Zr,Y) ○ ANION(O)

The expected EPR spectra in relation to the ligand symmetries may be listed as below:

1. An isotropic EPR spectrum could be observed with cubic symmetry where charge compensation must be remote, or if six ligand ions form a regular octahedron in which case the symmetry is again similar to cubic and spectrum should be isotropic.

   For example, for the type-C centre one of the above ligand symmetries may be an explanation.

2. An anisotropic EPR could be observed if the tetrahedron symmetry is distorted in any way, the axial field being body diagonal [111]. Some possibilities are discussed in section (3.3.1) for the explanation of the anisotropic behaviour of type-A centres.

3. For the slightly anisotropic behaviour of type-B line, the superposition of two spectra having ligands with one and two corners truncated from simple cubes seems the most probable explanation.

3.3 EPR spectra of as grown crystals

3.3.1 EPR spectra of type-A lines and discussions

Different rotation experiments have been performed to analyse the anisotropy in the tensor elements of the spectroscopic splitting factor g of the type-A lines.

The crystal was first mounted in the (100)-plane and the magnetic field was rotated about the sample cavity in 10° steps from 0° to 180°. The spectra observed in this plane consisted of two lines in almost all directions. Only one line was observed when the magnetic field was along [010].

The recorded EPR spectra for two overlapped and resolved cases are shown in Figure (3.2) and in Figure (3.3). The widths are 12.4, 17, and 10.2 mT respectively. One point worth mentioning here is that the width increment is observed when the peak position goes to higher magnetic field values. This is maybe due to inhomogeneity of the magnet sweep unit, so the comparison of the line widths is not meaningful. In order to reach a conclusion, however, comparison of the intensities, measuring the areas under the derivative form of the peaks with a planometer, showed that the areas of the overlapped and non-overlapped lines has the ratio of nearly 2 : 1.

The positions of the lines, which were measured with respect to the g-marker (DPPH) mentioned earlier, were plotted with respect to the rotation angle of the magnetic field (also the crystal orientation) in (100)-plane, as shown in Figure (3.4).

Secondly the crystal was mounted in the (010)-plane and again two lines were observed for all directions. The lines overlapped at the magnetic field direction ⟨100⟩ and they had maximum separation from each other, at the magnetic

---

Fig.(3.2) The overlapped position of the type-A lines in derivative form for the magnetic field parallel to the [100]-axis in the (100)-plane. As grown 8 mole % YSZ (1A10a), 35.5 GHZ, 290 $^{\circ}$K.

Fig.(3.3) The separated positions of the peaks mentioned in Fig. (3.2). Magnetic field 10 degrees from the [110] direction.

Fig.(3.4) Angular dependence of positions of the type-A lines with the magnetic field lying in the (100)-plane. As grown 8 mole % YSZ (1A10a), 35.5 GH_2, 290 $^{\circ}$K.

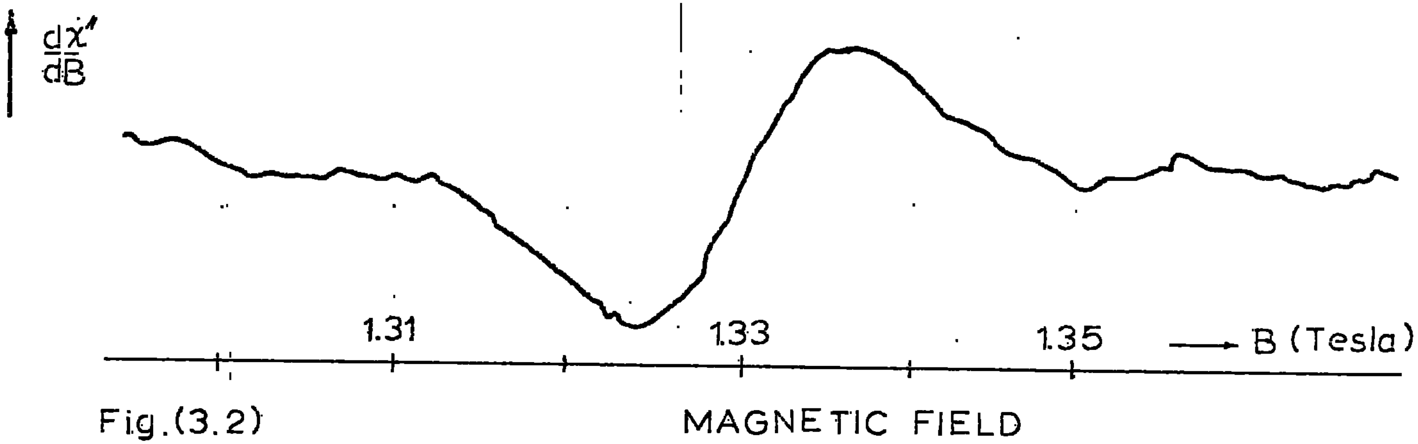
$\frac{d\chi''}{dB}$
1.31
1.33
1.35
→ B (Tesla)
MAGNETIC FIELD

Fig.(3.2)

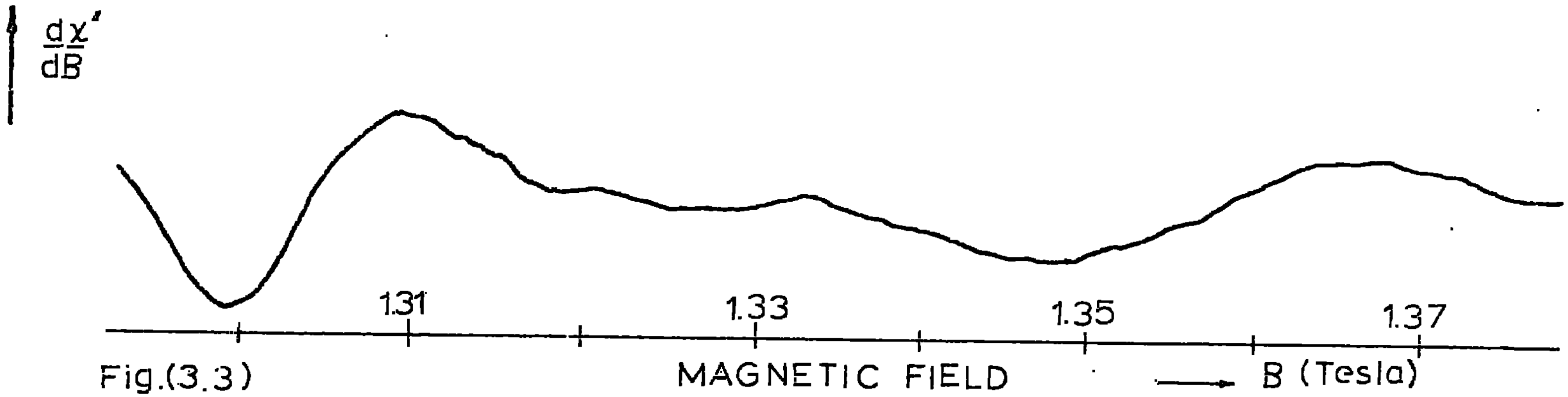
$\frac{d\chi''}{dB}$
1.31
1.33
1.35
1.37
MAGNETIC FIELD
→ B (Tesla)

Fig.(3.3)

Fig.(3.4)

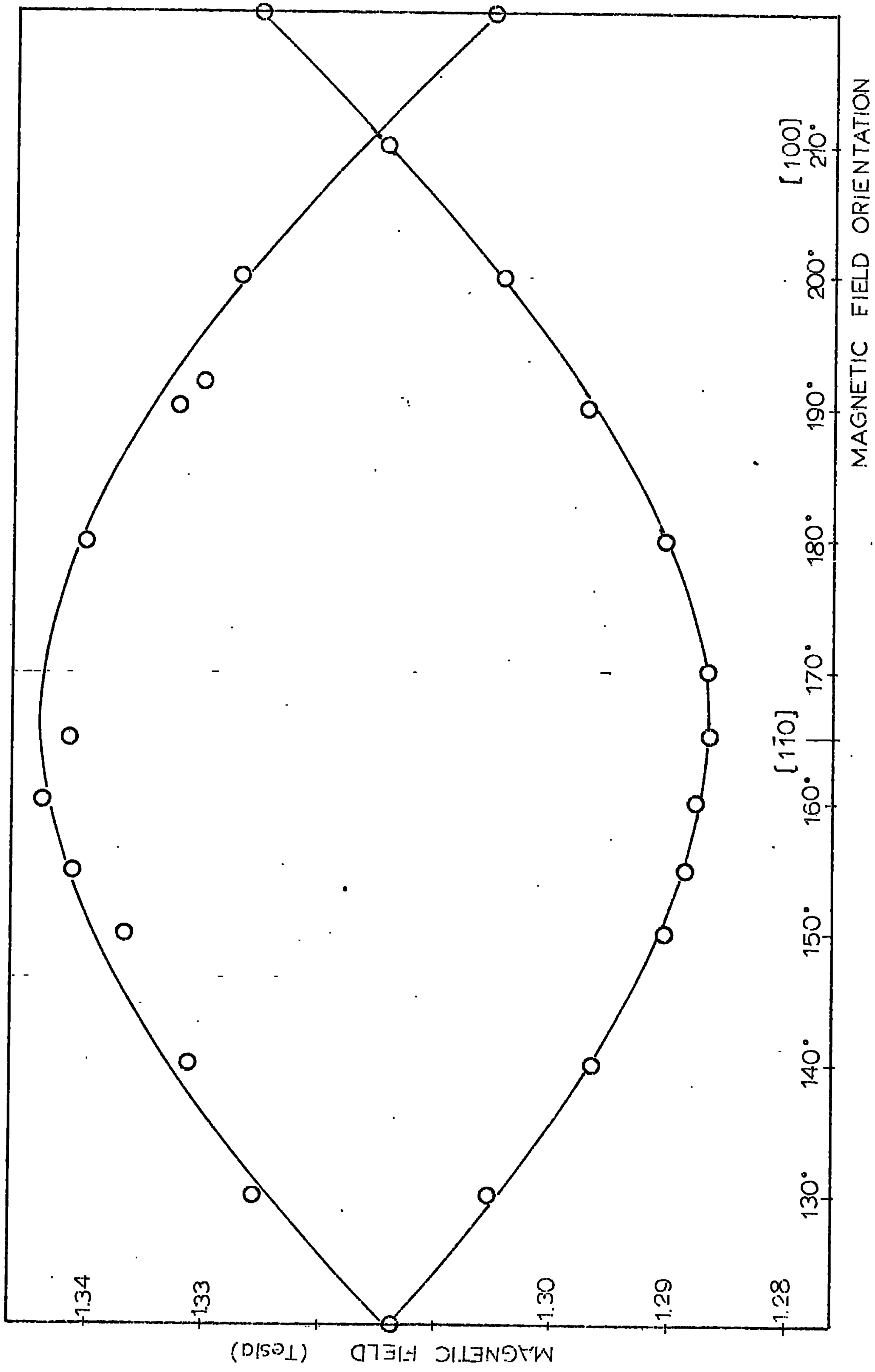
1.34
1.33
1.30
1.29
1.28
MAGNETIC FIELD (Tesla)
130°
140°
150°
160°
[1$\bar{1}$0]
170°
180°
190°
200°
[100]
210°
MAGNETIC FIELD ORIENTATION

field direction ⟨100⟩. The spectra obtained in this plane (010) and the anisotropy of the lines are shown in Figure (3.5).

From these two rotation experiments it was tentatively concluded that the ⟨111⟩ direction could be the axial symmetry axis. The EPR spectra would coincide and have the highest g-value for the magnetic field orientation along the ⟨111⟩ direction. Figure (3.6) shows that this is the case within the experimental uncertainties which are due to the obstructing position of the type-B line. A line(___) was inserted for comparison in order to show the position of free spin having g = 2.0023 which is almost equal to $g_{\parallel}$ as will be shown below.

The angular variation of the experimental g-values of type-A lines for both two (100) and the (010) planes are given in Figure (3.7). The data and the details of the calculations can be seen in Appendix 4. The full and open circles show the experimental g-values. The overlapping of the two experimental g-values has been performed with the choice of two g-values belonging to different planes but

---

Fig.(3.5) Angular dependence of positions of the type-A lines with the magnetic field lying in the (010)-plane. As grown 8 mole % YSZ (1A10a), 35.5 GHZ, 290 ^{o}K.

Fig. (3.6) Angular dependence of positions of the type-A lines with the magnetic field direction lying in the (111)-plane. As grown 8 mole % YSZ (1A10a), 35.5 GHZ, 290 ^{o}K.

Fig.(3.7) Variation of g-value for two A-type lines with polar angle, (open circles, measured in (010)-plane; full circles, measured in (100)-plane.

Fig.(3:5)

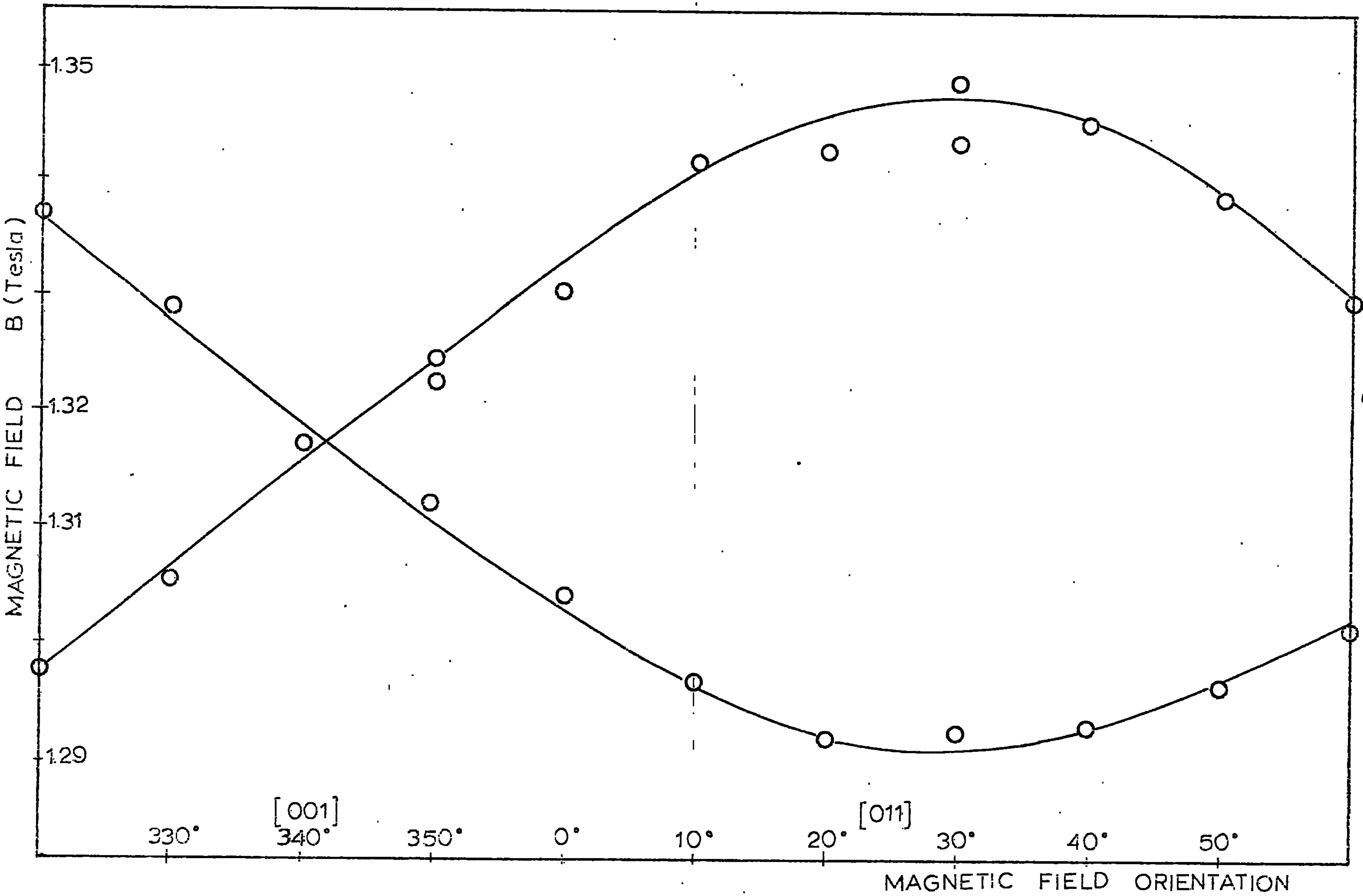
1.35
1.32
1.31
1.29
MAGNETIC FIELD B (Tesla)
[001]
[011]
330°
340°
350°
0°
10°
20°
30°
40°
50°
MAGNETIC FIELD ORIENTATION

Fig.(3.6)

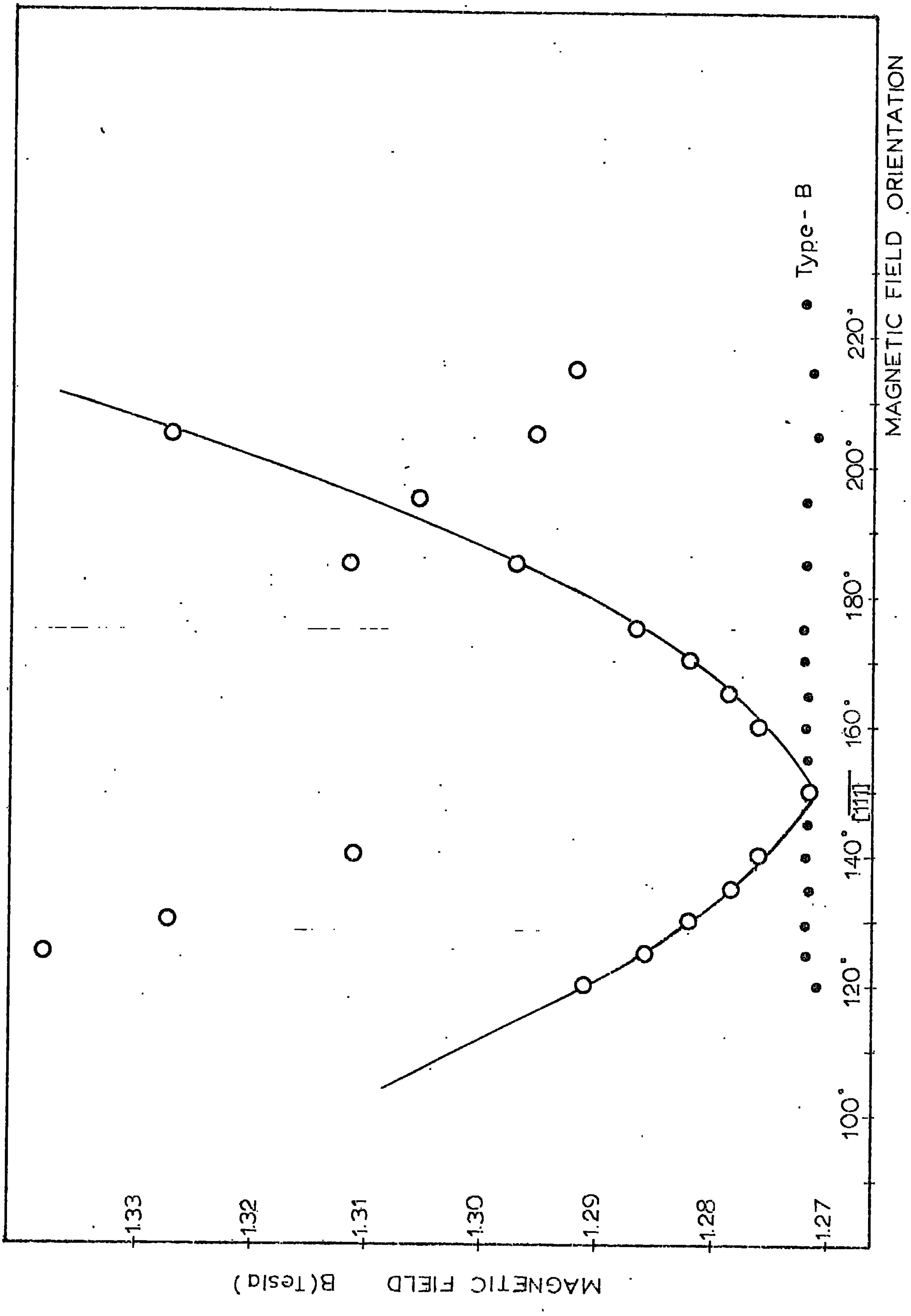
MAGNETIC FIELD ORIENTATION
100°
120°
140°
[111]
160°
180°
200°
220°
• Type - B
1.27
1.28
1.29
1.30
1.31
1.32
1.33
MAGNETIC FIELD B(Tesla)

Fig.(3.7)

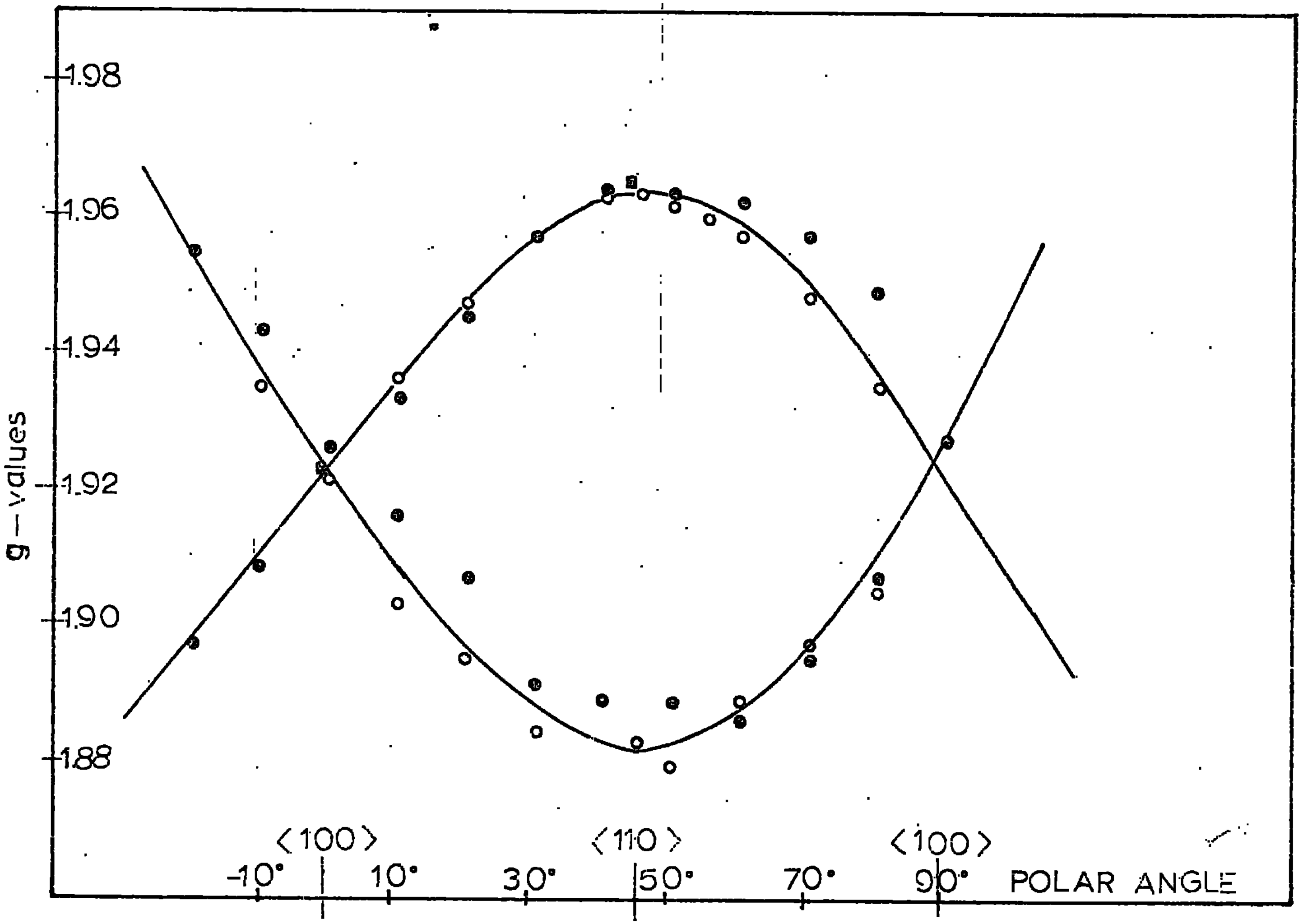
g – values
1.98
1.96
1.94
1.92
1.90
1.88
〈100〉
〈110〉
〈100〉
-10°
10°
30°
50°
70°
90°
POLAR ANGLE

at the same crystal orientation, (e.g. ⟨100⟩) which is known experimentally.

As will be seen in section (3.3.2) of this Chapter, when the experimental g-values are used to diagonalise the g-tensor, it is found that the ⟨111⟩ axis is really the axial symmetry axis with g-value components of $g_{\parallel} = 2.003$ and $g_{\perp} = 1.880$. All the other g-values range between these values for any direction of the magnetic field.

For the time being, leaving the reason of how the axial symmetry arises and the nature of the paramagnetic centre, the EPR spectra of type-A may be explained in the following way:

The observed type-A lines are in fact four lines, resulting from the EPR absorption of centres with axes of axial symmetry positioned along the four possible ⟨111⟩ directions. The value of the g-factor of each separate line is given by (1.37)

$$g^2 = g_{\parallel}^2 \cos^2\theta + g_{\perp}^2 \sin^2\theta$$

θ is being the angle between $\underline{H}$ and the ⟨111⟩ axis. For the three orientations of the crystal relative to the magnetic field H, it is found that:

1. H //⟨100⟩, every $[11\bar{1}]$ axis forms an angle of 54.7° with H and we may expect the lines of all centres to coincide due to the above equ.(1.37).
2. H //⟨110⟩, the ⟨111⟩ axes form two pairs of axes making angles 35.3° and 90° with H respectively in this case, the lines in each pair coincide and this results in different g-values for each pair.
3. H //⟨111⟩, the other ⟨111⟩-axes make an angle of 72° with H direction, grouping the lines into one and three.

We now pass on to the explanation of the axial field:

In tetrahedral co-ordination, the negatively charged oxygen ion is surrounded by a cage of four postively charged Zr^{4+} ions. If these four ligand ions form a regular tetrahedron, ions are placed alternately on the corners of the cube, the symmetry is similar to cubic. In many cases however small distortions occur.

If a line is drawn from the centre through one of the Zr^{4+} ions of the tetrahedron, the direction becomes the direction cosine [111] with respect to the four-fold [100] axis of the unit cell and if the ion on this line is at a slightly different distance compared with the other three, or has a different charge, an axial crystal field results. The symmetry is preserved around this axis so that g-values remain constant without being dependent on the magnetic field direction.

The best possibility for creation of the axial field along [111] is the substitution of Y^{3+} (ionic radius = 0.92A°) with Zr^{4+} (ionic radius = 0.79 A°), Pauling (1927), because of the different ionic radii.

As will be seen in Figure (3.1) replacement of Y^{3+} with any of the Zr^{4+} ions numbered Zr(1), Zr(2), Zr(3) and Zr(4) will always give rise to an unbalanced axial field along one of the body diagonal ⟨111⟩ directions. For the whole crystal it may well be possible to find four body diagonal ⟨111⟩ directions.

The other possible ions which may cause this axial field are Y^{2+}, Zr^{3+}, Zr^{2+}. The possibility of the existence of these ions and others will be discussed in section (3.3.3).

In all these cases, we consider two contributors to the creation of the axial crystal field; the "size" and the "charge" misfits.

The most probable explanation of type-A EPR centre is an electron trapped in the oxygen vacancy (an F-centre).

It has already been postulated by Casselton (1968b) from the conductivity measurements that "the electrolysis phenomenon observed at high current densities arises by electron injection from the cathode metal electrode into the ceramic. If the applied voltage is sufficiently large so that the rate of oxygen ion transport away from the cathode zone exceeds the supply from the surrounding atmosphere by the reaction

$$\tfrac{1}{2}O_2(\text{gas}) + Vo + 2e \longrightarrow O^{2-} \qquad 3.1$$

a large concentration of vacancies may be set up in the cathode zone sufficient to create a breakdown field that would overcome the metal-ceramic potential barrier, some of the injected electrons would be trapped in anionic vacancies, giving rise to color centres."

We have very convincing evidence based on the EPR results, in favour of this postulate. This evidence also allows us to assign the paramagnetic centre, causing the type-A line, to a trapped electron in an oxygen vacancy.

The series of EPR experiments explained below will show that the type-A centre disappears with heat treatment in oxygen and argon atmospheres but re-occurs again after the current blackening process; this may be explained according to the above equ.(3.1).

1. On the crystal 1A1On of 8 mole % YSZ, a rod having dimensions (1 mm^2 x 10 mm), the following treatments were made and EPR spectra were taken for comparison at

room temperature.

(a) Crystal $1A1On_1$ (as grown)

Result: type-A lines were present.

(b) Crystal $1A1On_2$ (annealed in the same conditions while crystal $1A1On_3$ was d.c. blackened in argon)

Result: type-A lines were not present.

(c) From the current blackened rod, under the following conditions of (1 A/cm^2, 10 m, 800^oC, in argon), two pieces of samples $1A1On_3$ and $1A1On_3'$ were examined.

Crystal $1A1On_3$: (majority of the sample piece was as grown with very little blackened part).

Result: type-A lines were present again.

The type-C line intensity observed was extremely weak; this may be due to the very small number of spins of the small blackened part which contribute to EPR.

Crystal $1A1On_3$: (a completely blackened piece was used).

Result: the type-A lines were much more intense than the one observed in the annealed specimen $1A1On_2$.

In addition an easily seen type-C line was present. The details of the type-C line will be given in section (3.4.2).

2. The following spectra were taken from 1A1Oq and $1A1Oq_3$ of which 1A1Oq was annealed and $1A1Oq_3$ was d.c. blackened in the conditions of (25 A/cm^2, 1 hr. 800^oC in argon).

(a) Crystal 1A1Oq (annealed in argon).

Result: type-A line was not present.

(b) Crystal 1A1Oq$_3$ (d.c. blackened).

Result: type-A lines were exist and type-C line was much more intense.

Casselton's (1968b) other postulate is based on the reverse reaction to the one given by equ.(3.1) and would be due to the heat treatment at a high temperature in an inert atmosphere. In this case the source of trapped electrons would arise due to the reaction

$$O^{-2} \longrightarrow \tfrac{1}{2}O_2(\text{gas}) + Vo + 2e \qquad 3.2$$

In order to increase the detectable number of spins and also to be sure to create centres (oxygen vacancies with single electrons) we first heated the sample in oxygen and then in vacuum.

As will be seen from the following results that second postulate is also verified for type-~~A lines~~.

1. Crystal 1A1.Oe (as grown) was recorded and type-A lines were observed.
2. The same crystal (as grown above) 1A1Oe was heated in O_2 at 1100 °C for 2.5 hrs., O_2 rate was 25 cc/min, cooled in O_2.

   Result: type-A lines were not observed.
3. The oxygen heated crystal was then vacuum reduced in the conditions of 10^{-3} torr at 1100°C for 3.5 hrs., cooled down to 200 °C over 6 hrs.

   Result: type-A lines were observed again although they had disappeared after oxygen heat treatment.

As it was shown before, like the current blackening process, vacuum reduction had re-created type-A lines.

We now see that Casselton's postulates about two reverse processes based on trapped electrons in oxygen vacancies are found to be satisfied for the type-A paramagnetic centres.

Previously reported F-centres in Alkali Halides are reviewed by Markham (1966) that they have g-values between 1.987 to 2.0029 and line widths 5 to 80 mT which also support our assignment of type-A lines as due to an F-centre.

The possibility of the assignment of either the type-A or type-B lines in as grown materials to any OH^- centre can immediately be rejected because, probably due to the growing process (electrofusion) of the crystals, (as will be seen in Chapter 6), no peak incorporating OH^- has been observed optically around 2.8 microns with either kind of YSZ. However it has been shown to occur in a number of materials grown as single crystals by flame fusion, for example, Y_2O_3 shows a very weak but sharp absorption band at 2.75 microns, Wickersheim et.al.(1961).

Any possibility of the assignment of type-A due to an electron-hole or a complex like $(Y_{Zr}', V_O^{\bullet})$, which has been proposed by Caillet (1968) on this basis of his conductivity data can also be rejected because of the non-observance of EPR spectra on the lower magnetic field side of free spin value. (According to Hund's rule the g-value is bigger than 2.0023 when the electronic shell is more than half full).

12 mole % YSZ (as grown)

With the same procedure as used for 8 mole % YSZ crystals, the EPR spectra of the 12 mole % YSZ as grown materials have also been recorded. They have not shown any differences at all on the type-A and type-B lines and no extra spectra have been observed.

The angular variation of type-A lines are shown in Figure (3.8), at room temperature.

Low temperature spectra of as grown YSZ

The investigation at 77 ^{o}K has shown no noticeable change of type-A and type-B lines, and no extra new spectra were observed.

The angular variations of type-A and type-B lines are shown in Figure (3.9) for crystal 1A10a.

3.3.2 Determination of the g-tensor for type-A lines

We have already mentioned in Chapter 1, section (1.8) that the principal g-values and their corresponding direction cosines may be determined from the experimentally found g-values.

We have also shown in Chapter 3, section (3.3.1) that the variation of the experimental g-values calculated from the EPR recordings (see figure (3.7)) with respect to the crystal axes in two perpendicular (100) and (010) planes of the as grown crystal 1A10a (8 mole % YSZ) at room temperature, perfectly overlapped if the ⟨100⟩ crystal axis is accepted as reference for this procedure.

A computer programme has been written in order to calculate the principal g-values and the principal axes

Fig.(3.8) Angular dependence of positions of the type-A lines with the magnetic field direction lying in the (100)-plane. As grown 12 mole % YSZ, 35.5 GHZ, 290 ^{o}K.

Fig.(3.9) Angular dependence of positions of the type-A and type-B lines with the magnetic field direction lying in the (100)-plane. As grown 8 mole % YSZ, 77 ^{o}K.

Fig.(3.8)

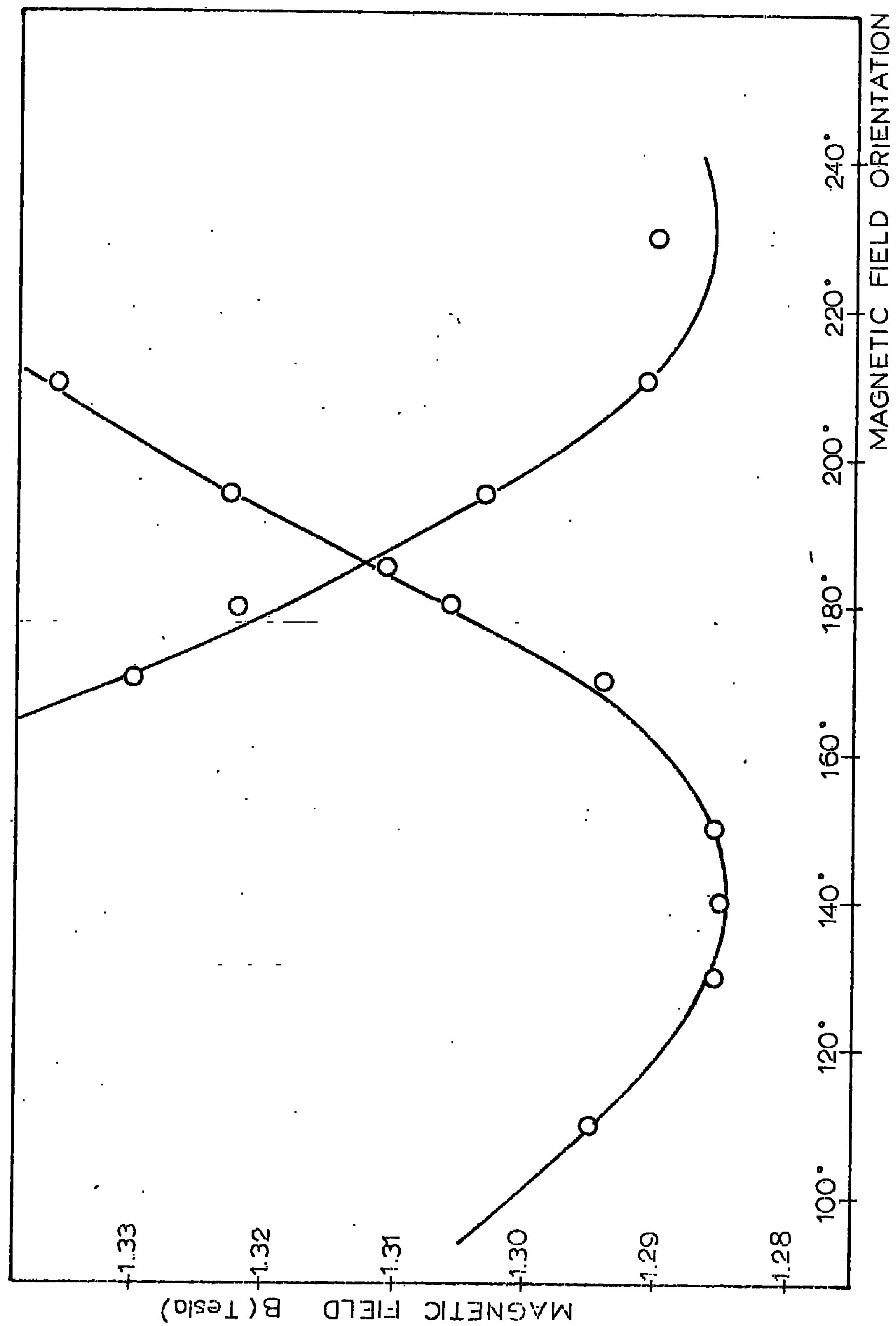
MAGNETIC FIELD B (Tesla)
1.33
1.32
1.31
1.30
1.29
1.28
MAGNETIC FIELD ORIENTATION
100°
120°
140°
160°
180°
200°
220°
240°

Fig.(3.9)

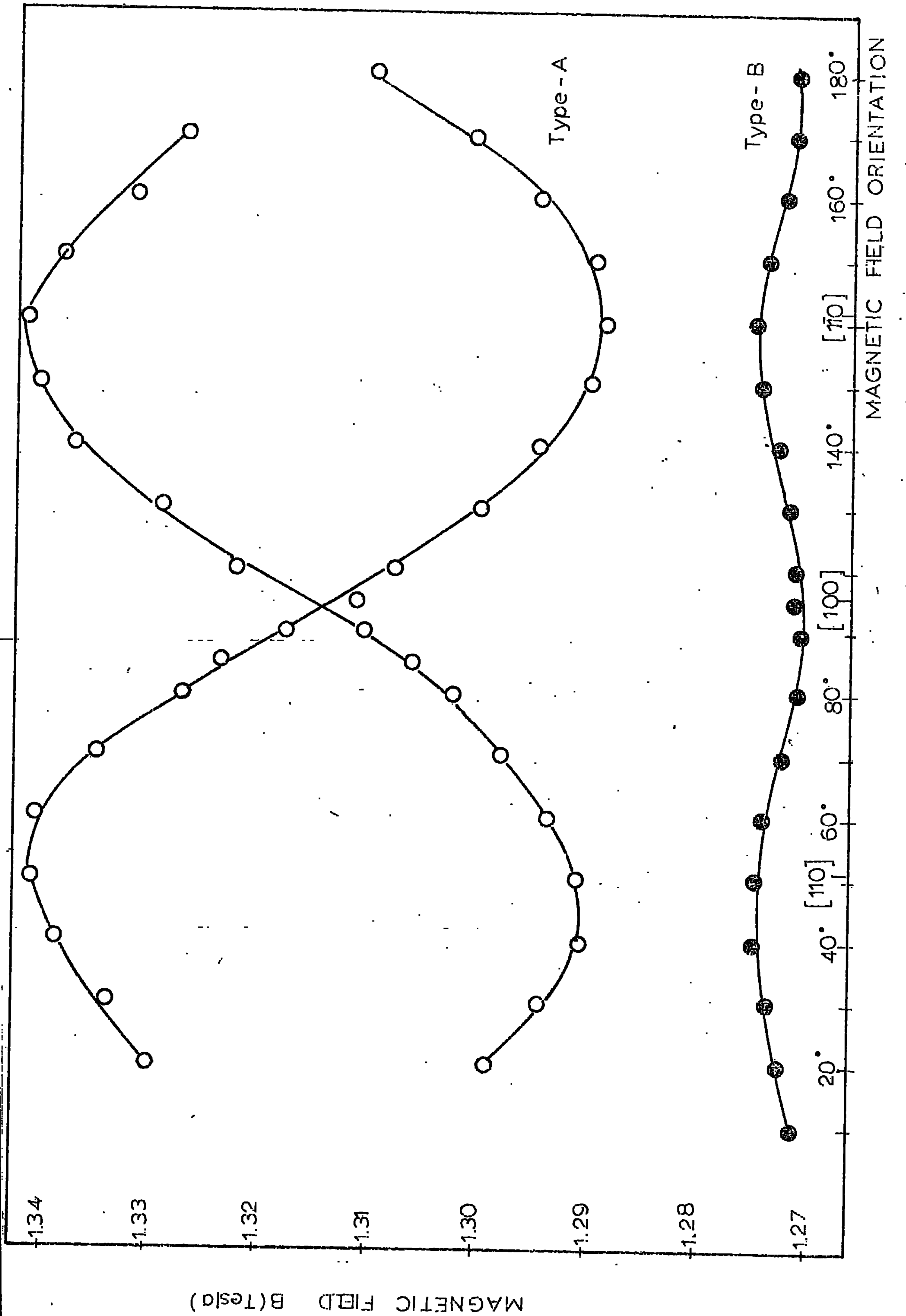
Type - A
Type - B
1.34
1.33
1.32
1.31
1.30
1.29
1.28
1.27
MAGNETIC FIELD B(Tesla)
20°
40°
60°
80°
140°
160°
180°
[110]
[100]
[1̄10]
MAGNETIC FIELD ORIENTATION

(direction cosines) of these principal values with respect to the crystal axes system as given below.

In order to run the computer programme three experimental g-values with their corresponding angles measured from a chosen reference crystal axis (e.g. ⟨100⟩), and the crystal plane numbers are used.

The simultaneous linear equations given below

$$g_{11}^2(\exp) = g_{xx}^2\cos^2\phi_{11} + 2g_{xy}^2\cos\phi_{11}\sin\phi_{11} + g_{yy}^2\sin^2\phi_{11}$$

$$g_{12}^2(\exp) = g_{xx}^2\cos^2\phi_{12} + 2g_{xy}^2\cos\phi_{12}\sin\phi_{12} + g_{yy}^2\sin^2\phi_{12}$$

$$g_{21}^2(\exp) = g_{yy}^2\cos^2\phi_{21} + 2g_{yz}^2\cos\phi_{21}\sin\phi_{21} + g_{zz}^2\sin\phi_{21}$$

$$g_{22}^2(\exp) = g_{yy}^2\cos^2\phi_{22} + 2g_{yz}^2\cos\phi_{22}\sin\phi_{22} + g_{zz}^2\sin\phi_{22}$$

$$g_{31}^2(\exp) = g_{xx}^2\sin^2\phi_{31} + 2g_{zx}^2\cos\phi_{31}\sin\phi_{31} + g_{zz}^2\cos^2\phi_{31}$$

$$g_{31}^2(\exp) = g_{xx}^2\sin\phi_{32} + 2g_{zx}^2\cos\phi_{32}\sin\phi_{32} + g_{zz}^2\cos^2\phi_{32}$$

are solved in conjunction with the *SSP subroutine programme called "SIM Q." The solutions g_{xx}^2, g_{xy}^2, g_{yy}^2, g_{xz}^2, g_{yz}^2, g_{zz}^2 etc. are components of the g^2 (3 x 3) symmetric tensor. It is necessary to diagonalise this so the * SSP subroutine "EIGEN" is used for this purpose. This gives a $(\underset{\sim}{g}^2)$-tensor whose off-diagonal elements are zero and the square roots of these diagonal components are the principal values of the g-tensor. The principal axes are also calculated.

The computer programme has been run for the experimental g-values, angles and plane numbers. These are tabulated with the corresponding calculated principal g-values and principal axes in Table (3.1).

```
   MTS-PROGRAMME EPR1
   TO DIAGONALISE THE G-TENSOR, IN ORDER TO FIND
   THE PRINCIPAL G-VALUES OF THE TYPE-A EPR LINE
   FOR THE CRYSTAL 8 MOLE% Y2O3 STABILIZED ZIRCONIA
  DIMENSION EG(6),IA(6),IP(6),R(3,3),AM(6,6)
  DIMENSION C(6),S(6)
  READ(5,20) EG
  READ(5,21) IA
  READ(5,22) IP
0 FORMAT(6F5.3)
1 FORMAT(6I3)
2 FORMAT(6I1)
  WRITE(6,30) EG
0 FORMAT(/,3X,16H EXP.G-VALUES:,6(3X,F5.3))
  WRITE(6,31) IA
1 FORMAT(//17H ANGLE(B,C.AXIS):,6(3X,I5))
  WRITE(6,32) IP
2 FORMAT(//,10X,16H PLANE:       ,6(I1,7X))
  DO 40 I=1,6
  DO 40 J=1,6
0 AM(I,J)=0.0
  DO 50 I=1,6
  EG(I)=EG(I)*EG(I)
  Y=3.1416/180.0
  C(I)=COS(Y*IA(I))
  S(I)=SIN(Y*IA(I))
  IF(IP(I)-2) 60,70,80
0 AM(I,1)=C(I)**2
  AM(I,3)=S(I)**2
  AM(I,2)=2.0*C(I)*S(I)
  GO TO 50
  AM(I,3)=C(I)**2
  AM(I,6)=S(I)**2
  AM(I,5)=2.0*C(I)*S(I)
  GO TO 50
  AM(I,6)=C(I)**2
  AM(I,1)=S(I)**2
  AM(I,4)=2.0*C(I)*S(I)
  GO TO 50
  CONTINUE
  CALL SIMQ(AM,EG,6,KS)
  IF(KS.NE.0) GO TO 90
  CALL EIGEN(EG,R,3,0)
  EG(1)=SQRT(EG(1))
  EG(3)=SQRT(EG(3))
  EG(6)=SQRT(EG(6))
  WRITE(6,100) EG(1),EG(3),EG(6),((R(I,J),J=1,3),I=1,3)
  FORMAT(//20H PRINCIPAL G-VALUES:,3(3X,F5.3),//,4X,16H PRINCIPAL AX
 1ES:,3(3X,F5.3),/,2(20X,3(3X,F5.3),/))
  GO TO 110
  WRITE(6,120)
  FORMAT('THE SIMULTANEOUS EQUATIONS ARE SINGULAR')
  STOP
  END
```

TABLE (3.1)

Exp. g-values :	1.963	1.880	1.963	1.880	1.963	1.880
Angle (H and ⟨100⟩-axis) :	45	135	45	135	45	135
Plane numbers :	1	1	2	2	3	3
Principal g-values :	2.003		1.880		1.880	
Principal axes :	0.577 0.577 0.577		0.390 -0.816 0.426		-0.717 0.021 0.696	

The principal g-values in Table (3.1) being 2.003, 1.880, 1.880 indicate the existence of an axial symmetry for the g-value of 2.003 with direction cosine 0.577; (arc cosine 0.577 = $54^{o}41'$ being the angle between the axial field and the [100] direction of the crystal).

With the use of the simple trigonometric relationships for a cubic structure, it is found that: the angle θ_1 (between ⟨111⟩ and ⟨100⟩) and θ_2 (between ⟨111⟩ and ⟨110⟩) are $54^{o}41'$ and $35^{o}21'$ respectively. Two conclusions can be derived from this.

1. The axial symmetry axis is the body diagonal ⟨111⟩ direction of the crystal.
2. If we re-write the equ.(1.37) mentioned in Chapter 1, section (1.8)

$$g = (g_{\parallel}^{2} \cos^{2}\theta + g_{\perp}^{2}\sin^{2}\theta)^{\frac{1}{2}}$$

and substitute the calculated $g_{\parallel} = 2.003$ and $g_{\perp} = 1.880$ values for the angles $\theta_1 = 54^{o}41'$ and $\theta_2 = 35^{o}21'$ one by one in the above equation, we find two g-values for the magnetic field directions along the ⟨100⟩ and ⟨110⟩. These are shown in Figure (3.7) with full squares and fit quite well with the experimental values.

For comparison the calculated and experimental values are given in Table (3.2)

TABLE (3.2)

Angle	g-values Calculated	 Experimental
$\theta_1 = 54^{\circ}41'$	1.922	1.921
$\theta_2 = 35^{\circ}21'$	1.964	1.963

3.3.3 EPR spectra of type-B line and discussions

The type-B spectrum of as grown crystals of YSZ has been recorded with the procedure explained in section (3.3.1). In Figure (3.10) the asymmetric type-B line seen in the (100)-plane is shown together with type-A lines for comparison.

The slightly anisotropic behaviour and the width change were observed as shown in Figure (3.9). The width changed between the values of 10±1 and 6±1 mT corresponding to the ⟨110⟩ and ⟨100⟩ directions of the unit cell. The g-values were also found to be 1.997 and 1.990 respectively at maximum ⟨100⟩ and minimum ⟨110⟩ positions.

The heat treatment of crystals (see Appendix 2) in argon and oxygen atmospheres or vacuum reduction seemed not to effect the type-B line. This result can be taken as an indication of the centre being a paramagnetic ion. The intensity of the line decreased quite noticeably over a year during which the specimen had been kept in room temperature in air.

Fig. (3.10) Spectra observed in as grown 8 mole % YSZ. Magnetic field 16 degrees from [100] direction in (001)-plane; 35.5 GHz, 290 °K.

Fig.(3.10)

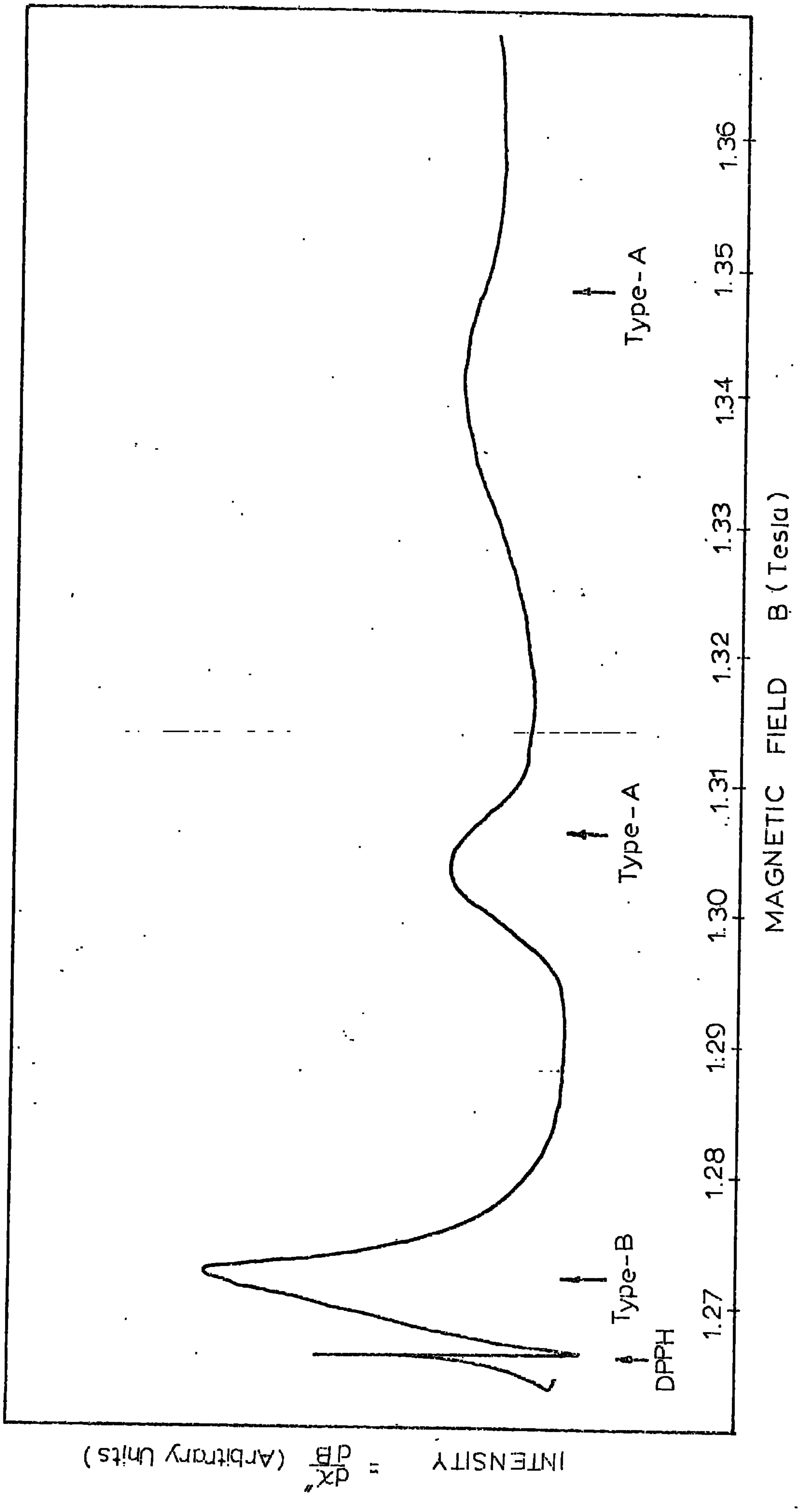
DPPH
Type-B
Type-A
Type-A
1.27
1.28
1.29
1.30
1.31
1.32
1.33
1.34
1.35
1.36
MAGNETIC FIELD B (Tesla)
INTENSITY = $\frac{d\chi''}{dB}$ (Arbitrary Units)

Discussions of EPR of type-B line

Why is the type-B line assigned to a cation?

1. The possibility of assignment of the type-B line to a cation arises because of the symmetry of the local ligand as has been explained in section (3.2).
2. As has been mentioned in section (3.3.1) assignment to an OH^- ion or to $(Y_{Zr}, V_O)^{\bullet}$ is not possible. Caillet (1968) has postulated that:

$$Y_{Zr}' + V_O^{\bullet\bullet} \longrightarrow (Y_{Zr}, V_O)^{\bullet} \qquad 3.3$$

   as is seen from Figure (3.1). Let us assume that substitution of Y^{3+} for Zr^{4+} causes an oxygen ion to vacate its place. This would act as if it had a double positive charge. Assume further that this makes $Y^{3+} \rightarrow Y^{4+}$ with a trapped hole of charge +1 at the centre of the tetrahedron. Under these assumptions if we say that type-B is due to Y^{4+}, we should have observed a "hole" resonance as well as on the lower field side of the free spin value according to Hund's Rule. But we have not seen such a "hole" resonance spectrum. Following the same argument the re-occurrence of the other V, U centres is also not expected. (For detailed discussion see for instance Low (1962)).
3. The unaffected behaviour of the type-B line due to heat treatment of the sample in various atmospheres at high temperature ($\simeq 1000\ ^{\circ}C$) may be considered as an indication of a paramagnetic ion rather than a colour centre Low (1962).

What is (or are) then this (these) cation(s)?

In order to give the most plausible identification of the type-B line, the possibilities are discussed in the following section.

In YSZ samples the possible paramagnetic ions (excluding the effect of the impurities mentioned in Chapter 2, section (2.2.2)) with their electronic configurations are:
$Zr^{5+}(3p^5)$, $Zr^{3+}(4d^1)$, $Zr^{2+}(4d^2)$, $Y^{4+}(3d^5)$, $Y^{2+}(4d^1)$.

1. The creation of Y^{4+} and Zr^{5+} ions during the growth process is not possible because as will be seen from Table (3.3) in both cases the ionization energies required to maintain charge neutrality would be excessive, since in every case the ionization required would be from a filled electron shell. In fact when Y_2O_3 is introduced into the ZrO_2 lattice the yttrium occupies normal lattice sites while a certain number of oxygen sites are left vacant, Hund (1951). This is preferable to the formation of either Y^{4+} or Zr^{5+} which would be required if all sites were to be filled. On the other hand the occurrence of a complete range of solid solution from the fluorite to the C-type body centred cubic lattice, through a progressively increasing number of oxygen vacancies, strongly support this; Coullough et.al.(1952), Bruner et.al.(1951).

TABLE (3.3)

Values of the ionization energies (in ev.) for zirconium and yttrium together with corresponding ionic radii (in A^o). The ionization values were reproduced from Griffiths (1963) p.379, Hester (1965), table 5.1, Cotton and Wilkinson (1962), table 30.1. The ionic radii were taken from Gmelins Handbuch-der Anargonishen Chemie 8. Auflage-Zirconium p.103.

	Ionization stages						
	0	1	2	3	4	5	6
Zirconium							
Ionization En:		6.84	13.13	22.98	34.3		99
Ionic radius:	1.58	1.33	1.11	0.93	0.80		
Yttrium							
Ionization En.:		6.38	12.23	20.5	77		

2. The ions Zr^{3+} and Y^{2+} are the best candidates for type-B single line rather than Zr^{2+} which should have given three lines.

The reduction energies (or ionization energy differences) for Zr^{4+} to Zr^{3+} is 11.32 ev and for Y^{3+} to Y^{2+} is 8.27 ev. These indicate that Zr^{4+} may be more easily reduced to Zr^{3+} than Y^{3+} to Y^{2+} Mott and Gurney (1948) p.102. However, as the ionization energies do not differ very much, we might expect both ions; Zr^{3+} and Y^{2+} to be created. The asymmetric appearance of the line might then be due to overlap of these two ions' contributions. (This assumption might also explain the fact of the directional broadening) as well as the distorted ligand effects.

The reported Y^{2+} EPR by O'Connor (1963) with $g = 1.994 \pm 0.005$ fits our mean g-value 1.993 closely. There is not any data for Zr^{3+} and very little for Zr^{2+} by Matamura (1963).

As pointed out by Ahrens (1952) "because the ionization energy differences between the ionization states are low, no low valence states of zirconium can be found in a geological environment. Because of this, the oxidation up to the quadrivalent state is always immediate." In fact, if type-B is due to Zr^{3+} only, the disappearance of the line after one year may be understood according to the fact just given above.

The 4d as well as the 5d transition metal ions are known to be more covalently bound than the 3d ions and this gives rise to a stronger crystal field. The strong field ground state of the $4d^1$ configuration is $(d\ )^1(t_2)$, $s = \frac{1}{2}$. The g-factor in the octahedral (6 co-ordination) symmetry can be written in terms of the orbital reduction factor k as $g = \frac{2}{3}(2k + 1)$ Griffiths (1961) p.365. From our results for Zr^{3+} or Y^{2+}, we obtain $k \doteq 0.994$ for $g = 1.993$. But the observed slight anisotropy for the type-B line indicates that the crystal field is not completely octahedral so the attempted fitting may be questionable.

<u>Why is the line shape asymmetric</u>?

1. It seems unlikely that the asymmetric shape is due to unresolved hyperfine structure. The only nucleus having nuclear spin other than zero is Zr^{91} which is only 11% abundant (Assenheim (1966) p.181) and is unlikely to be effective at this small level.
2. The asymmetric appearance due to overlap of the two Zr^{3+} and Y^{2+} ions' contributions has been mentioned before in order to explain the directional broadening of this line.
3. It seems however that distorted ligands due to oxygen vacancies are the most plausible explanation for this asymmetry; the slight anisotropy may be due to very well established oxygen deficient character of the crystal

structure.

3.4 EPR spectra of current blackened crystals

3.4.1 Review of conduction electron spin resonance in metals

Conduction electron spin resonance (CESR) studies, both experimental and theoretical, are extremely scarce compared to the usual EPR of localized spins.

The first CESR, observed by Griswold (1952), was due to very fine particles of sodium in paraffin wax. A resonance was obtained with a $g = 2.000 \pm 0.003$ and a line width of 78 gauss which was independent of temperature.

The first systematic work was that of Feher (1955). Some of the reported CESR results in metals are shown in table (3.4). Several reviews surveying the previous theoretical and experimental work on CESR are also given by Knight (1951), Yafet (1963).

TABLE (3.4)

CESR properties of metals

	Half width (T_2^{-1} (gauss)		Temp. dependant line width	reference
	minimum	room temp.		
Lithium	0.1	0.1	no	Gueron (1965)
Sodium	0.1	7	yes	Vercial (1964)
Potassium	0.15	12	yes	Walsh (1966a)
Rubidium	0.4	-	yes	Walsh (1966b)
Caesium	25	-	no-	Schultz (1966)
Copper	8	-	yes	Schultz (1965)
Beryllium	1.0	1.2	yes	Cousins (1965)
Magnesium	150		yes	Bowring (1971)
Aliminum				Schultz (1966)
Palladium Wolfram	no resonance observed			Feher (1955)

The observed spectra for the metals listed in Table (3.4) are sufficiently narrow, i.e. within the detection limit of the equipment. The CESR absorptions in metals investigated by Feher (1955) were with Li, Na, K, Be, Mg, Al, Pd, W but no resonances were observed in Mg, Al, Pd, or W. From the knowledge of the sensitivity (10^{16} spins per Oersted at room temperature) the spectrometer had put an upper limit to the spin-relaxation time of the above metals of $T_2 < 5 \times 10^{-10}$s.

According to Elliot (1954) the principal theory of CESR for metals can be summarized as follows:

The line width is related to the conduction electron spin relaxation time which in turn is dominated by electron-phonon interaction through the spin-orbit coupling. In materials which have short relaxation times and hence larger inherent line widths, the resonance will be more difficult to detect. Yafet (1963) gave more refined formulae concerning the relaxation time.

However, in the case of small particles Kubo (1962) pointed out that relaxation processes are likely to be significantly modified. Recently Holland (1966) has shown that the electron-phonon scattering should be strongly inhibited in particles which are sufficiently small (less than 100 A° diameter). As a consequence of this the spin-relaxation time should be increased by orders of magnitude, thus CESR should be more easily observed in small particles than bulk metal. For particles smaller than the 100 A° limit, he expects a temperature independent broadening and a shift of the resonance line. Then as the particle size increases, the line width narrows and a temperature-dependence of the width begins. Finally a further broadening with increasing size shows that the Elliot mechanism becomes dominant.

The line shape for CESR has been given by Dyson (1955) for bulk specimens where the sample dimensions are both greater and smaller than the microwave skin depth.

Some of the observed CESR due to metallic (colloid) particles in dielectric crystal matrices are given in

Table (3.5).

TABLE (3.5)

Some CESR and optical data on colloidal metallic particles.

Metallic particle	how created	line width (gauss)	g-value	optical absorption(A°)	Reference
Li (LiH)	Irra.UV	0.3	2.002	6500	Doyle (1959)
K (KBr)	additively	6	1.9997	7500	Jain (1968)

The detection of a CESR signal is a non-trivial problem since the number of effective spins is usually small due to the small skin depth in metals and further the lines are broad. Several original techniques have been used besides the classical methods; e.g. selective-transmission, Lewis et.al. (1964) or Bolometer detection, Schmidt et.al.(1966).

We could exclude reviewing the CESR made on semiconductors, (due to electrons in their conduction bands), because of dealing with an insulator such as YSZ. However, injection of the electrons during current passage introduces electrons to the conduction band of the crystal and some of them are trapped in the donor levels (oxygen vacancies) so the material may be considered a doped semiconductor in the blackened condition. The CESR in semiconductors is different in two ways from that in metals.

1. In order to populate the conduction band, shallow impurities are needed but the effect of the donors appearing as electron traps cannot be neglected Kodera (1964).
2. The possibility of varying the conduction electron concentration permits the Fermi level of the electron gas to be changed, Duncan et.al. (1964) p.1171.

The question arises, how can colloidal particles be recognized? Some possible methods are:

1. The temperature independence of the intensity of CESR. The susceptibility of conduction electrons is temperature independent in contrast to the approximate 1/T dependence for paramagnetic ions, Kittel (1966), p.446.
2. The closeness of the observed g-value to the free electron $g = 2.0023$ suggests three possibilities: CESR, an organic free radical or a transition metal ion whose orbital angular momentum is almost quenched.
3. The optical scattering and optical absorption bands observed in the visible range. These also show temperature independent behaviour as well as a shift to longer wavelengths which may be due growing particle sizes.
4. From nuclear magnetic resonance, measuring "knight shift." Evidence for the metallic character of the precipitates was obtained for instance by Levy (1956) measuring Knight Shifts for potassium and caesium precipitates in frozen liquid ammonia solutions.

3.4.2 The EPR spectra of current blackened samples and discussions

In the (100)-plane, the EPR spectra of current blackened samples showed that a symmetric spectrum (type-C) was observed in addition to the type-A and type-B lines, on the higher magnetic field side but almost overlapping with the type-B line. This is shown in Figure (3.11).

The isotropic position of the type-C line for two 8

Fig.(3.11) Spectra observed in current blackened 8 mole % YSZ. Magnetic field 5 degrees from [100] direction in (001)-plane; 35.5 GHz, 290 °K.

Fig.(3.11)

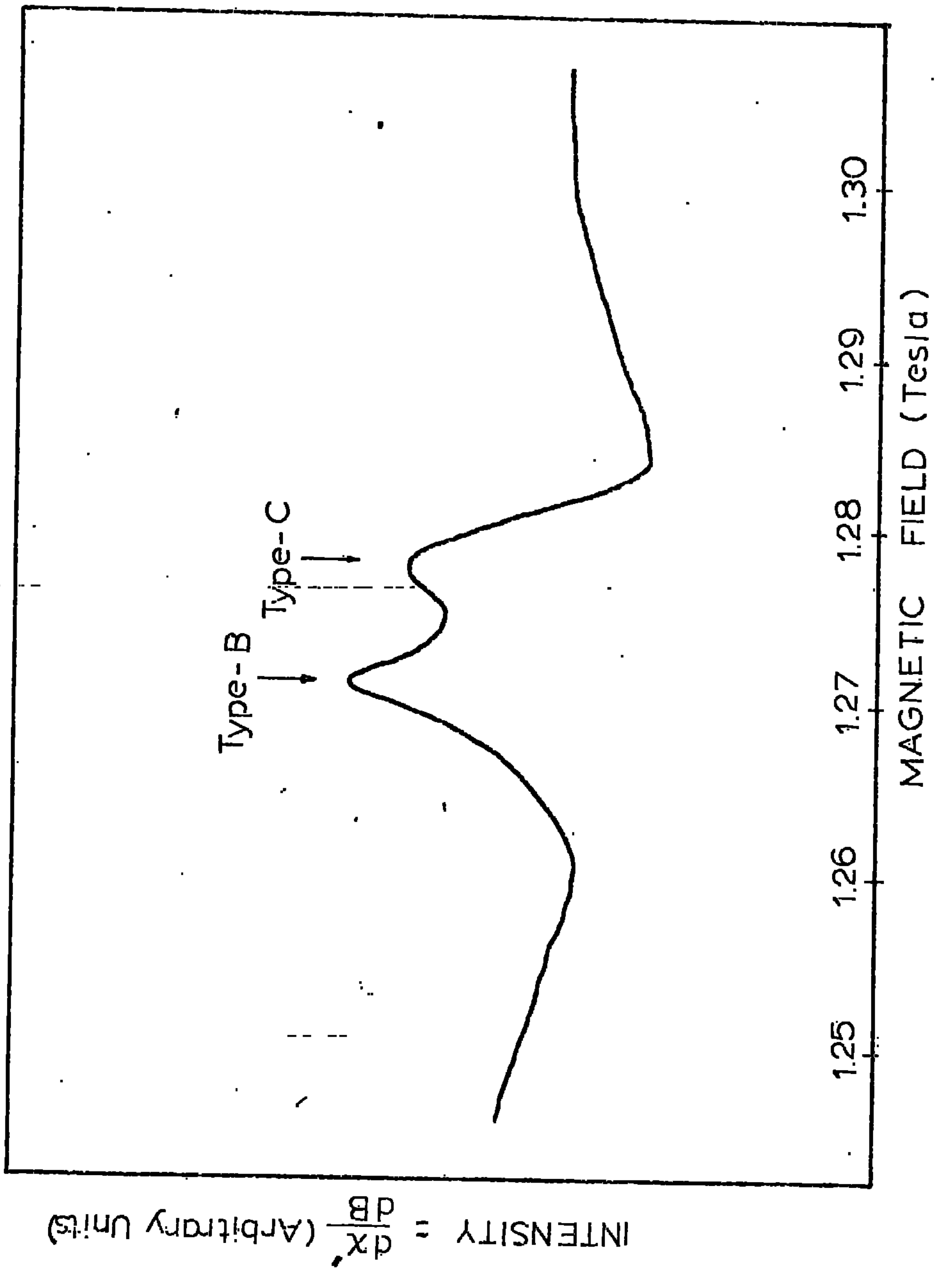
Type-B
Type-C
1.25
1.26
1.27
1.28
1.29
1.30
MAGNETIC FIELD (Tesla)
INTENSITY = $\frac{d\chi'}{dB}$ (Arbitrary Units)

and 12 mole % YSZ samples are shown in Figure (3.12) and Figure (3.13) respectively, including type-B and type-A lines.

The recorded EPR spectra showed that the line intensity increased with increasing applied current density. This had ranged from 1A/cm^2, the minimum for a detectable type-C EPR signal, to 25 A/cm^2, which was almost the upper limit firstly because of the friability of the sample during current passage and secondly due to almost complete lowering of the Q-factor of the cavity.

The line width was measured to be 5.0 ± 0.5 mT (50 ± 5 gauss) with the g-value of 1.986.

It seemed that the line has lost some of its intensity over a year in a sample which had been kept at room temperature, in air.

Fig.(3.12) Angular dependence of positions of the type-A, type-B and type-C lines with the magnetic field orientation. Current blackened 8 mole % YSZ; 35.5 GHZ, 290 $^{\circ}$K.

Fig.(3.13) Angular dependence of positions of the type-A, type-B and type-C lines with the magnetic field orientation in current blackened 12 mole % YSZ; 35.5 GHZ, 290 $^{\circ}$K.

Fig.(3.12)

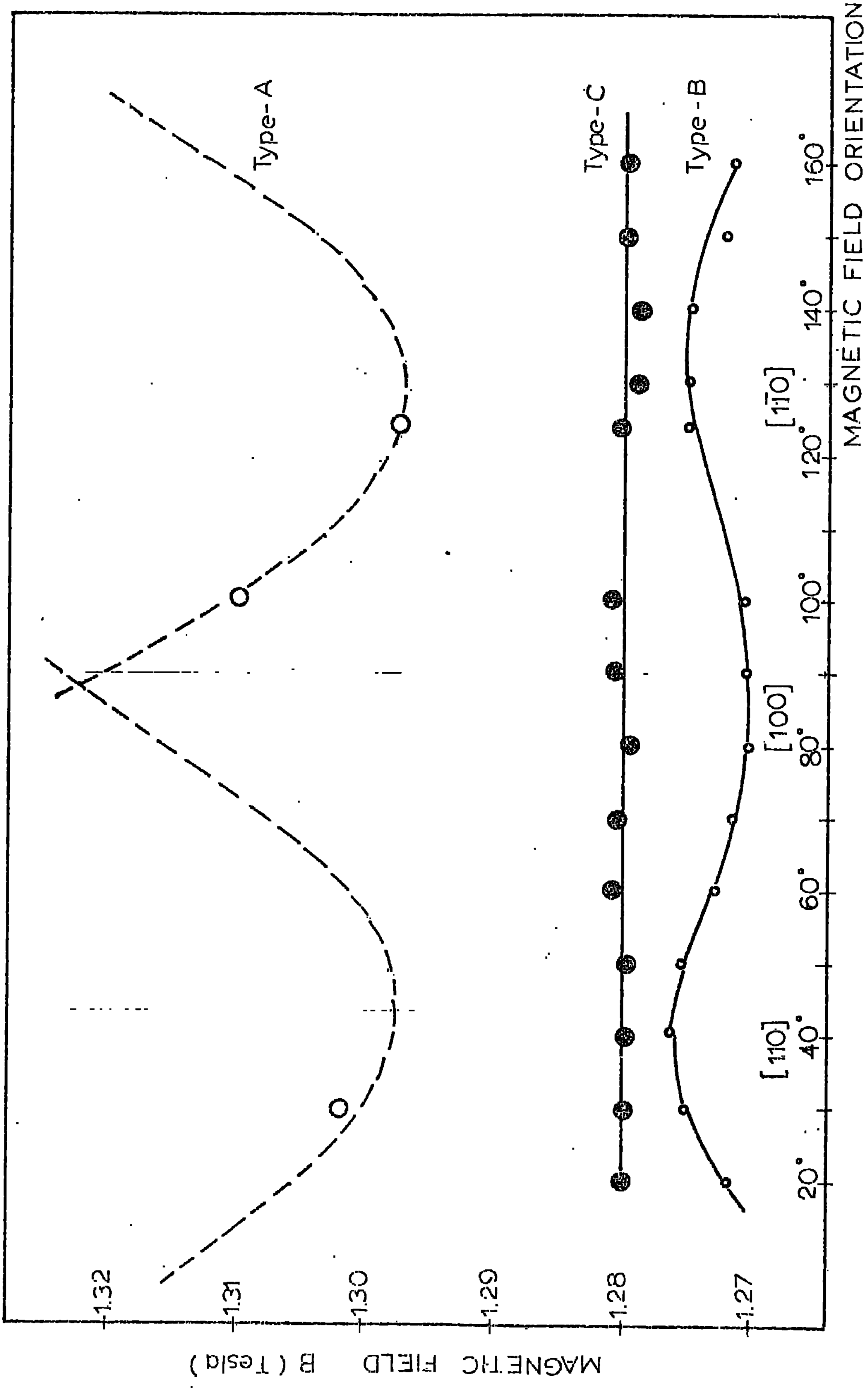
Type-A
Type-C
Type-B
[110]
[100]
[1̄10]
20°
40°
60°
80°
100°
120°
140°
160°
MAGNETIC FIELD ORIENTATION
1.32
1.31
1.30
1.29
1.28
1.27
MAGNETIC FIELD B (Tesla)

Fig. (3.13)

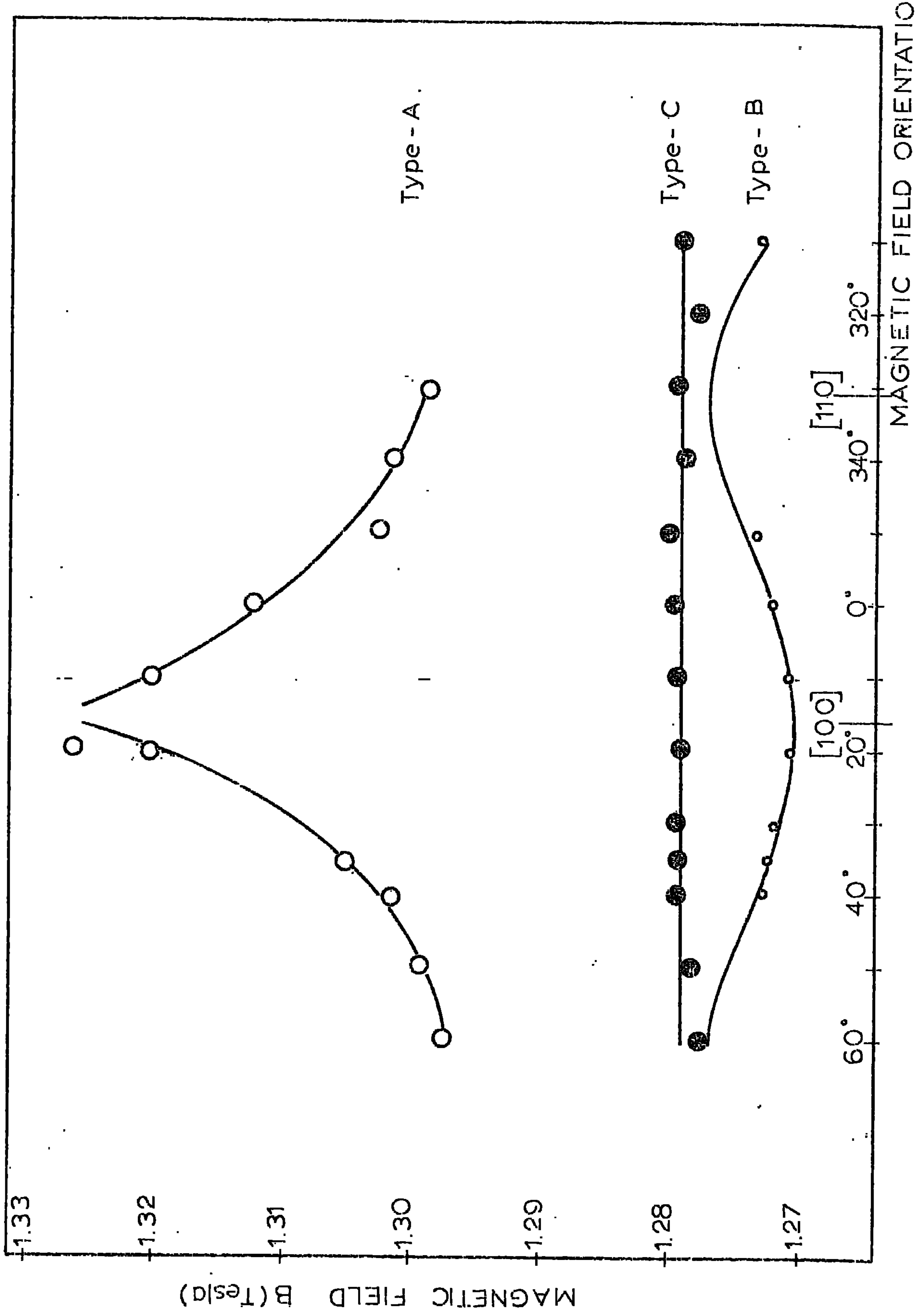
Type - A
Type - C
Type - B
MAGNETIC FIELD ORIENTATION
60°
40°
20°
[100]
0°
340°
[110]
320°
1.33
1.32
1.31
1.30
1.29
1.28
1.27
MAGNETIC FIELD B (Tesla)

The following factors may also be taken into account as a support of the assignment of type-C to conduction electrons of the colloidal metallic particles of zirconium.

1. Having a g-value of 1.986 very close to free spin g-value 2.0023.
2. When the spin-orbit coupling constant of Zr metal is compared with Cu see Table (3.6) for which CESR have been observed as seen in Table (3.4). It is found that because of the line width dependence on spin-orbit coupling (as has been explained in section (3.4.1)), it is possible to expect to observe CESR for Zr metal. It becomes more plausible when it is in the form of fine metallic particles.

TABLE (3.6)

Values of the one-electron spin orbit coupling parameter (in cm^{-1}) of Zr, Y, and Cu reproduced from McClure (1959), Table 8.

Element	electronic configuration	spin-orbit coupling (cm^{-1})
Cu	$3d^9 4S^2$	818
Y	$4d\ 5S^2$	225
Zr	$4d^2 5S^2$	355

3. If it was due to colloidal particles, because of the symmetry of the peak, the size of the particles is smaller than the microwave skin depth, (the skin depth for Zr metal is about 30 microns at 35.5 GHz). This does not conflict with the optical scattering data, from which a particle size in the range 10-50 millimicrons was estimated.

An alternative approach is suggested if we look at the situation from different angle and suppose that the type-C line is not due to conduction electrons of the metallic particles but rather to conduction electrons in the conduction band of the crystal which have been created by electron injection during the current passage process.

In order to populate the conduction band, we need to inject electrons. This was evident in our experiment as the intensity of the line seemed to increase with increasing current density. On the other hand we must not neglect the effect of the donors (oxygen vacancies) acting as electron traps.

CHAPTER-4

THEORY OF OPTICAL PROPERTIES

CHAPTER 4

THEORY OF OPTICAL PROPERTIES

4.1 Introduction

The concepts of the optical properties, in relation to the experiments given in Chapter 6, will be given here. Interband transitions, the absorption edge and the optical constants are stressed most.

4.2 Background theory to optical properties of YSZ

4.2.1 Band structure of transition metal oxides

Most of the general features of the optical properties of these materials have not been extensively studied. Reviews of the electronic structures of the transition metal and rare earth compounds can be found in the references of Morin (1958), Adler (1968a, 1968b), Methfessel (1969), Falicov (1971).

4.2.2 Interband transitions

The behaviour of the optical constants near interband edges, in other words at the absorption edge, concern us mostly.

The predictions of the Quantum theoretical calculations for the direct and indirect transitions near interband edges are based on the well known band theory, resulting from studying the one-electron approximation problem in a spatially periodic field of the pure crystalline semiconductors Callaway (1964), McLean (1960).

The energy dependences of the absorption constant, K, which is proportional to the imaginary part of the complex dielectric constant ϵ'' for the direct and indirect transitions are given below.

Direct transitions

With direct transitions, the absorption of electromagnetic radiation is explained as the interaction between radiation and the electrons in the material.

1. Direct-allowed transitions

$$K \propto (\hbar w - Eg)^{\frac{1}{2}} / \hbar w \qquad 4.1$$

2. Direct-forbidden transitions

$$K \propto (\hbar w - Eg)^{3/2} / \hbar w \qquad 4.2$$

Indirect transitions

Transitions of the indirect type involve simultaneous interaction of electrons with the electromagnetic radiation and the lattice vibrations.

3. Indirect-allowed transitions

$$K \propto (\hbar w - Eg \pm Ep)^{2} / \hbar w \qquad 4.3$$

4. Indirect-forbidden transitions

$$K \propto (\hbar w - Eg \pm Ep)^{3} / \hbar w \qquad 4.4$$

These power laws can be checked against experimental data to see whether a fit to one type of transition is obtained. This has been attempted for both 8 and 12 mole % as grown YSZ samples as will be seen in Chapter 6, section (6.2.2).

The problem of how to apply these theoretical results to YSZ, which has yttria as an impurity in zirconia, is somewhat unclear. To consider the exact optical absorption in the presence of perturbations such as impurities, it is necessary to set up the more general formulation of the Kubo approach, Bonch-Bruevich (1966).

4.2.3 Absorption edge

The rapid increase in absorption which occurs over a small energy range is a common feature of the optical absorption spectrum to all semiconductors when the absorbed radiation has an energy roughly equal to the energy gap of the semiconductor or insulator. This is called the absorption edge, Eg, of the material.

The large increment of absorption is due to onset of absorption in which electrons are raised from the valence band across the forbidden energy gap to the conduction band. A study of the position of this edge and the internal structure may give some information about the energy gap and the properties of electron states just above the conduction band edge and below the valence band edge. Because these states close to the conduction and valence band edges also determine the electrical properties of the material the exploration of the absorption edge becomes extremely useful.

For photon energies larger than Eg, the material is opaque; for energies smaller than Eg, transparent. Here the work has been devoted to the investigation of the region of transparency which gives us information about various imperfections in the lattice (e.g. impurities, defects, phonons, charge carriers).

The optical absorption edge is characterized by an exponential (or Urbach) behaviour of the absorption constant with photon energy. An Urbach (1953) absorption edge obeys the relation

$$K = K_0 \exp (\gamma' (\hbar w - Eg)/kT) \qquad 4.5$$

the value of γ' in the above empirical relation appropriate for Urbach edges is observed to be nearly always close to 0.5 corresponding to a rate of fall off in K at room temperature by about a factor of 10 per 0.1 ev. (see Davies and Shaw (1970), Fig.16).

The Urbach effect is observed in many crystalline solids notably the Alkali Halides. A unique explanation for the effect has not yet been found. However, several explanations have been offered for the Urbach edge: Hopfield (1968), Toyazawa (1964), Mahr (1963) suggest that it is the low energy side of a temperature broadened exciton line. Redfield (1965) proposes an electric field broadening of the absorption edge. In the absence of exciton formation this is the Franz-Keldysh effect. Dexter (1967) considers a quadratic stark effect, the electric field arising from and hence varying with the lattice vibrations. Davydov (1968) proposes excitation from vibrational sublevels of the lattice to account for the exponential edge and its change of slope with temperature. Dow and Redfield (1970) have solved the problem of absorption with exciton formation in the presence of an electric field and propose that the Urbach effect arises from an electron field broadening of an exciton.

4.2.4 Optical constants

Optical measurements do not determine the material constants ϵ' and ϵ'' directly, but determine related quantities, the so called optical constants: the refractive index n, and the attenuation index k. They are real and positive numbers.

For optically isotropic materials, such as cubic YSZ, the optical constants describe an electromagnetic plane wave in the medium. This can be considered as follows

$$\underline{E}\ (t,\ x) = E_o \exp\left[-\ iw\ (t - x\ (n - ik)/c\right] \qquad 4.6$$

where the electric vector $\underline{E}$ lies in the yz-plane, the refractive index n gives the phase shift of the wave, the attenuation index k gives the attenuation of the wave.

Instead of n and k we may use the complex refractive index

$$N = n + ik \qquad 4.7$$

The functions n(w) and k(w) can be connected by a dispersion relation (called sometimes after their discoverers Kramers-Kronig relations) and various useful modifications are discussed by Moss (1959).

In practice, the absorption coefficient K(cm^{-1}) is used instead of the attenuation index k

$$K = \frac{4\pi}{\lambda} k \qquad 4.8$$

if the wave equ.(4.6) is substituted into the Maxwell equations

$$N^2 = \epsilon\ (w) \qquad 4.9$$

is obtained from which real and imaginary parts of the dielectric constant is found to be respectively

$$\epsilon'' = 2nk \qquad 4.10$$

$$\epsilon' = n^2 - k^2 \qquad 4.11$$

Normal incidence reflectivity

In the case of normal incidence, the complex vectors of the reflected and incident waves $\underline{E}_{or}$, $\underline{E}_{oi}$ are connected by the relation

$$\underline{E}_{or} / \underline{E}_{oi} = r(w) \qquad 4.12$$

where

$$r(w) = \frac{N(w) - 1}{N(w) + 1} \qquad 4.13$$

The ratio of the intensities of the waves are measured in the experiments. We obtain

$$R(w) = \left|r(w)\right|^2 = \frac{(n - 1)^2 + k^2}{(n + 1)^2 + k^2} \qquad 4.14$$

where r(w) can be expressed as complex number

$$r(w) = R(w)^{\frac{1}{2}} \exp\left[i\varphi(w)\right] \qquad 4.15$$

R(w) is the reflection constant. The phase angle $\varphi(w)$ is given by the relation

$$\tan\varphi = \frac{2k}{n^2 + k^2 - 1} \qquad 4.16$$

which is connected with the amplitude R(W) by a dispersion relation which was first obtained by Jahoda (1957)

$$\varphi(w) = -\frac{w}{\pi}\int \frac{\mathrm{Ln}\, R(\xi)}{\xi^2 - w^2}\, d\xi \qquad 4.17$$

Thus the phase angle $\varphi(w)$ can be calculated if the function R(w) is measured over the entire spectral region and n and k can then be obtained from equ.(4.16) and equ.(4.14).

Normal incidence transmission

When the crystal is transparent in order to obtain the optical constants two quantities such as the reflectance and transmittance of the same crystal slice (RT-method) or the transmittance of the sample for two different thicknesses (TT-method) are measured at each wavelength.

The complete formulae for the transmitted and reflected intensities I_t and I_r respectively for incident intensity

$I_o = 1$ are given by Stratton (1941) ·

$$\frac{I_t}{I_o} = \frac{e^{-Kd}\left[(1 - R)^2 + 4R\,\sin^2\varphi\right]}{(1 - R\,e^{-Kd})^2 + 4R\,e^{-Kd}\,\sin^2(\varphi + \alpha)} = T \qquad 4.18$$

$$\frac{I_r}{I_o} = \frac{R\,(1 - e^{-Kd})^2 + 4\,e^{-Kd}\,\sin^2\alpha}{(1 - Re^{-Kd})^2 + 4R\,e^{-Kd}\,\sin^2(\varphi + \alpha)} = D \qquad 4.19$$

where K is the absorption coefficient; d is the layer thickness, R is the coefficient of surface reflection; T and D are the transmission and reflection coefficient of the entire layer.

If no interference fringes are observed because of for example surface roughness, the equ.(4.18) and equ.(4.19) take the form of;

$$\frac{I_t}{I_o} = \frac{(1 - R)^2\,e^{-Kd}\,(1 + \frac{k^2}{n^2})}{1 - R^2e^{-2Kd}} = T \qquad 4.20$$

$$\frac{I_r}{I_o} = \frac{(R\,(1 - e^{-2Kd})}{1 - R^2e^{-2Kd}} = D \qquad 4.21$$

These equations show that n and K can be found from T and D. For most transmission experiments $k^2 \ll n^2$. If d is further chosen to ensure that $R^2e^{-2Kd} \ll 1$, equ.(4.20) takes the extremely simple form of

$$T = (1 - R)^2\,e^{-Kd} \qquad 4.22$$

Hence K can be found simply from the transmission of two samples of different thickness without knowing the surface reflection of the sample, provided the reflectivity of both samples is the same.

We have applied this (TT-method) to our as grown both 8 and 12 mole % YSZ and current blackened samples as they will be seen in Chapter 6.

RT-method

This method differs from the TT-method in that T, R are directly measured quantities.

The initial formulae are equ.(4.20) and equ.(4.21) the shortcoming of this method compared with the TT-method is the need for preparing a sample thick enough with one polished surface. Only then can one determine R by eliminating reflection from the opposite face, in this special case D becomes equal to R. Absorption coefficient, K, is obtained from equ.(4.20).

$$K = \frac{1}{d} \mathrm{Ln} \frac{2TR^2}{-(1-R)^2 + \sqrt{(1-R)^4 + 4T^2R^2}} \qquad 4.23$$

calculating k from equ.(4.23) and equ.(4.8) we determine the refractive index from

$$n = \frac{1 + R + \sqrt{4R - (1-R)^2 k^2}}{1 - R} \qquad 4.24$$

which was derived from equ.(4.14). This method was applied to current blackened samples at room temperature, see Chapter 6, section (6.5.1.2).

CHAPTER 5

EXPERIMENTAL TECHNIQUES AND SAMPLE PREPARATION

CHAPTER 5

SAMPLE PREPARATION AND EXPERIMENTAL TECHNIQUES FOR OPTICAL SPECTROSCOPY

5.1 Introduction

In this chapter we are concerned with the instrumentation, techniques and sample preparation for the measurement of optical absorption coefficient, reflection coefficient and refractive index of the as grown and blackened 8 and 12 mole % YSZ. The electron probe microanalysis results are also included as part of the search for information on the character of the blackened crystals.

5.2 SAMPLE PREPARATION

5.2.1 Polishing procedure

5.2.1.1. Polishing procedure for the as-grown samples

The order of the absorption coefficient, K, may be estimated using the approximate criteria of $K.d \sim 1$, Tauc (1966). For the single crystal K is about 10^3 cm^{-1}, (this value may increase up to 10^6 cm^{-1} for the thin films of the material) so the sample thickness around or less than 100 microns can be chosen as a reasonable value.

Successive abrasives were used for surface polishing, finishing with 1/4 micron diamond. A Logitech lapping machine was used. The parallelism of opposite faces of the crystal slice was good, giving a wedge angle of less than 0.05 degrees. Using Olsen's data (Olsen (1964), fig.8) and knowing that the refractive index was 2.18, the error in the transmission spectra was estimated as 1%.

5.2.1.2 Polishing procedure for the current blackened samples

During the first experiments on current passage, using samples about 100 micron thick, both polished faces were used for applying platinum paste contacts; the experiments always failed, due to cracking near the cathode end, whatever the current density. Later 1 x 4 x 8 $(mm)^3$ samples (in which the thickness was increased) were prepared from unoriented single crystal piece and current blackened following exactly the same procedure as explained in Chapter 2, section (2.2.3). For current densities of 20, 60 and 80 mA/cm^2 no blackening was observed in the cathode region. Further investigation showed that a current density of 0.1 A/cm^2 seemed the lowest value (with 2.5 volts potential difference applied across the 8 mm long sample) for blackening due to d.c. current passage.

For transmission experiments samples were prepared with current densities of 0.1 A/cm^2, 1 A/cm^2 and 5 A/cm^2. The last value (i.e. 5 A/cm^2) also seemed the highest applicable current density still yielding uncracked samples. The blackened samples were later polished following the procedure explained for the as grown ones. When the friable character of the material after current passage is borne in mind, limitations due to the difficulty of preparing thin samples (especially for the second thickness measurements on the same sample) may be appreciated.

5.2.2 Sample quality examination

The polished crystal slices used for the transmission experiments were examined under an ordinary microscope (magnification x 100) and no pull out or scratches havebeen observed. The polarizing microscope with crossed polaroids was used to examine possible departures from isotropy, by rotating the stage of the microscope. In as grown crystals no anisotropy was observed. Similar experiments could not be made for the current treated samples, because they were not transparent to the visible light.

The two Laue-Back reflection photographs taken on the same surface of the sample 1A15d (8 $^{m}/o$ YSZ) which had blackened (cathode) and unblackened (anode) regions indicates that no major change is observed on the perfection of the sample.

5.2.3 Electron probe microanalysis

With the Geoscan electron probe microanalyser made by Cambridge Instrument Company the following as grown and current blackened samples were analysed by Dr. A. Pechett, University of Durham, Department of Geology. The conditions used were.

analysis at : 15 kV
standards : pure Y and Zr, oxygen stoichiometric.
corrected for : dead time, mass absorption, fluorescence, atomic number.

The current passage procedure was applied as explained in Chapter 2. Then the samples were ground down, polished to a 1 micron finish, stuck on a glass microscope slide with 'Lake side 70' cement and coated with carbon.

The analysis results are given below.

1. Sample 1A15e, as grown 8 $^{m}/o$ YSZ

	Zr(%)	Y(%)	ZrO_2 ($^{w}/o$)	Y_2O_3 ($^{w}/o$)
Edge	63.294	11.468	85.498	14,563
Centre	63.040	11.766	85.154	14.942
Centre	62.976	11.427	85.068	14.511
Edge	63.028	11.735	85.138	14.902

Result: The differences between the various point analyses are not significant and may be attributed to experimental error.

2. Sample 1A14, 8 $^{m}/o$ YSZ, current blackened, 5 A/cm^2

	Zr(%)	Y(%)	ZrO_2 ($^{w}/o$)	Y_2O_3 ($^{w}/o$)
Anode end (yellow)	63.011	11.479	85.116	14.577
Junction(brown)	63.754	11.376	86.119	14.446
Cathode end (black)	64.318	11.013	86.880	13.985

Result: There is a slight suggestion that there is a gradient in composition across the specimen, but the error in experimental method may be misleading.

3. Sample 2A22d, 12 $^{m}/o$ YSZ, current blackened, .1 A/cm^2

The analysis of this sample showed 19.00 $^{w}/o$ yttria content and was also uniform across the unblackened and blackened parts.

In these experiments the estimated precision was better than ± 2 % relative, e.g. Zr = 63.04 ± 1.16 %.

As a conclusion, it may be said that, for both 8 and 12 mole % current blackened YSZ samples, no noticeable change was observed in the amounts of the Zr and Y compared with as grown crystals. This result seems consistent with the almost non-observable cation conduction (10^6 times less than oxygen) for calcia stabilized zirconia.

5.3 EXPERIMENTAL TECHNIQUES

5.3.1 The spectrophotometers

Several different spectophotometers were used for transmission measurements depending on the spectral range chosen. The other instruments used for reflectivity and refractive index measurements are also described below.

1. Optica CF4 -DR

Most of the transmission measurements were made by using this instrument in the range of .25 to 2.5 microns.

The instrument is a double beam, grating, spectrophotometer with a chart pen recorder. Two kinds of lamps; Deuterium (.185-.360 microns) and tungsten (.360-3 microns) are incorporated with the two photomultipliers for the ranges of .2-.7 microns and .7-3 microns respectively. For the principles of operation and more details, the reader is referred to the manuals.

2. Model 457 (Perkin-Elmer)

This spectrophotometer was used for the transmission measurements in the range of 2.5-40 microns. This instrument was favoured to the Spectromaster partly because of the large range of wavelength scanned and partly because of having a better resolution (4 cm^{-1} at 3000 cm^{-1}).

3. Hilger and Watts

This monochromator was used for reflectivity and refractive index measurements in the range of visible wavelengths.

4. Monochrom (Grubb-Parsons)

This monochromator, type PM 2, No.3 was used for the reflectivity measurements in conjunction with a glass prism and quartz iodene lamp in the range of .6-2.5 microns.

5.3.2 Experimental performance and data handling

5.3.2.1 Transmission measurements

Measurements of the spectral distribution of the transmission of 8 and 12 mole % YSZ as grown and d.c. blackened samples have been made at room temperature and temperatures close to that of the liquid nitrogen. The wavelength range covered in the measurements was from .25 to 2.5 microns.

The measurements were made using an Optica CF4 -DR continuously recording spectrophotometer. To use small crystals for transmission measurements, some kind of sample holder was necessary. It was covered with a matt black sticking tape to minimize unwanted reflections.

The procedures followed, covering several lamp, detector and filter change-over points, are given below:

Lamps are aligned

0 and 100 % sets at .350 microns

Red filter in, photomultiplier changed at .610 microns and 0 and 100 % sets made

Grating changed, new 0 and 100 % sets with red filter at 1 micron

Green filter in at 1.2 micron

Yellow filter in at 1.8 micron

End at 2.5 micron

Low temperature experiments

For low temperature experiments, the crystal slices were fixed with silicone compound to the 'copper finger' which formed the bottom of the liquid nitrogen reservoir of the cryostat, which had silica windows. It was held under evacuation continuously during the experiment and one filling with nitrogen lasted 40 minutes. The temperature was measured with a copper-constantan thermocouple attached to the copper 'finger' close to the sample. Normally the temperature ranged around 97 ^{o}K.

5.3.2.1.1 Derivation of the absorption coefficient with Transmission-Transmission method (TT-method)

This was applied to as grown and current blackened samples in the range of .25-2.5 microns.

Without knowing the reflection coefficient, the equ. (4.22) is used for this purpose. The transmissions were recorded for two different thicknesses of the same crystal d_1 and d_2 which were measured with a dial gauge.

In order to make the calculations to obtain absorption coefficient, K, a computer programme was written using Fortran - 4; one of the versions is shown in Table (5.1). The bulk of the data input is pairs of numbers corresponding to the sample transmission at each wavelength, the reading interval was so chosen with the absorption in mind that the longest wavelength points are separated by 100 A^{o}, the shorter ones by 50 A^{o} and the shortest by 20 A^{o}. The output consists of a row for each point with columns containing the wavelength, energy in ev, absorption constant, K, in cm^{-1} and several powers of K in order to find out the type of band-to-band transition.

5.3.2.1.2 Derivation of the absorption coefficient with Reflectivity-Transmission method (RT-method)

This method was applied only to the current blackened sample examined at room temperature in the range of .6-2.5 microns. After the surface reflection coefficient R was measured on the one polished surface of the 2 mm thick sample (using the method mentioned in section (5.3.2.2)).

TABLE (5.1)

```
      DIMENSION IW(90),E(90),AK(90),AK12(90),EAK12(90),EAK2(90)
      DIMENSION T1(90),T2(90)
      WRITE(6,20)
      WRITE(6,21)
      WRITE(6,22)
   20 FORMAT(15HXTALS COMPARED:)
   21 FORMAT(15HTEMPERATURE   :)
   22 FORMAT(15HDATE          :)
      WRITE(6,13)
   13 FORMAT(4X,6HWAV(A),5X,5HE(EV),4X,6HAK(CM),2X,8HAK12(CM)

     1,1X,11HEAK12(EVCM),1X,10HEAK2(EVCM)/)
      READ(5,3) IMAX,IWAV
    3 FORMAT(2I6)
      READ(5,1) (T1(I),I=1,IMAX)
      READ(5,1) (T2(I),I=1,IMAX)
    1 FORMAT(20F4.1)
      READ(5,4) D1,D2
    4 FORMAT(2F7.4)
      DIF=D2-D1
      WRITE(6,7) D1,D2,DIF
    7 FORMAT(3F7.4)
      IW(1)=IWAV
      E(1)=1.24/IW(1)
      E(1)=10000*E(1)
      DO 10 I=1,IMAX
      IW(I+1)=IW(I)+20
      E(I+1)=1.24/IW(I+1)
      E(I+1)=10000*E(I+1)
   10 CONTINUE
      DO 15 I=1,IMAX
      AK(I)=ALOG(T1(I)/T2(I))
      AK(I)=AK(I)/DIF
      AK12(I)=SQRT(AK(I))
      EAK12(I)=SQRT(E(I)*AK(I))
      EAK2(I)=EAK12(I)**4.0
      WRITE(6,2) IW(I),E(I),AK(I),AK12(I),EAK12(I),EAK2(I)
    2 FORMAT(I10,F10.3,F10.1,F10.2,F12.1,F11.1)
   15 CONTINUE
      RETURN
      END
 FILE
```

[illegible] less than about 100 microns and both surfaces were polished to a 1/4 micron finish. The transmission was then recorded in the same wavelength range.

The absorption coefficient is calculated from equ.(4.23) in chapter 4, knowing the measured values of reflection coefficient R, transmission T and the sample thickness d. The computer programme written to make the calculations exists. See Table (5.2).

5.3.2.2 Reflectivity measurements

5.3.2.2.1 Reflectivity measurements in the near I.R. region

The Monochrom Grubb Parsons, type PM 2, No.3 monochromator was used with the glass prism and quartz iodene lamp.

The sample, polished to a 1/4 micron finish, was fixed with durofix onto the glass slide beside two pieces of glass which had silver evaporated on them. Care was taken to ensure the parallelism of the three pieces by observing the continuous reflection of an object from the three surfaces.

An ordinary lamp is used, chopped with 10 c/s chopper. The light is detected with a photo diode in order to have a reference signal for the phase sensitive detecting system. Another light beam, which is also chopped with 10 c/s chopper, comes from quartz iodene lamp source which required a current of about 6 ampere.

The rectangular area of the monochromatized beam is so adjusted that, using a lever, the beam is allowed to reflect once from the sample and then from silver, accepted as a standard. Reflections are read as millivolts from the standard and sample respectively, for each wavelength. In order to calibrate the reflections, a light beam of the same area was reflected from the sample and the standard at a wavelength

TABLE (5.2)

```
1 rt
C       A COMPUTER PROGRAM IN ORDER TO CALCULATE
C       THE ABSORPTION CONSTANT AND THE REFLACTIVE INDEX
C       USING RT-METHOD
      DIMENSION W(100),E(100),R(100),T(100),AK(100),
     1AK12(100),AN(100),E1(100),E2(100),
     2R1(100),U(100),V(100),V1(100),V2(100),
     3T1(100),Z1(100),Z2(100),Z3(100),Y(100),
     4EX(100),EX2(100),R3(100),R4(100),R5(100),
     5R6(100),AN2(100),R2(100),EX1(100)
      WRITE(6,40)
      WRITE(6,41)
      WRITE(6,42)
      WRITE(6,43)
      WRITE(6,44)
   40 FORMAT(6H XTAL:)
   41 FORMAT(11H C.DENSITY:)
   42 FORMAT(11H THICKNESS:)
   43 FORMAT(6H DATE:)
   44 FORMAT( 8H TEMP:RT)
      WRITE(6,30)
   30 FORMAT(5X,1HW,5X,1HE,5X,1HR,5X,1HT,4X,2HAK,
     1 2X,4HAK12,4X,2HAN,6X,2HE1,5X,2HE2)
      READ(5,1) IMAX
      READ(5,2) (W(I),I=1,IMAX)
      READ(5,2) (R(I),I=1,IMAX)
      READ(5,2) (T(I),I=1,IMAX)
      READ(5,5) D
    5 FORMAT(F6.4)
    1 FORMAT(I5)
    2 FORMAT(10F5.3)
      D1=1.0/D
      DO 11 I=1,IMAX
      R1(I)=R(I)**2
      U(I)=2.0*T(I)*R1(I)
      V(I)=1.0-R(I)
      V1(I)=V(I)**2
      V2(I)=V1(I)**2
      T1(I)=T(I)**2
      Z1(I)=4.0*T1(I)*R1(I)
      Z2(I)=SQRT(V2(I)+Z1(I))
      Z3(I)=Z2(I)-V1(I)
      Y(I)=ALOG(U(I)/Z3(I))
      AK(I)=D1*Y(I)
      AK12(I)=SQRT(AK(I))

   11 CONTINUE
      DO 10 I=1,IMAX
      E(I)=1.24/W(I)
      E1(I)=E(I)*AK(I)
   10 CONTINUE
      G1=4.0*3.1416
      G2=1.0/G1
      DO 12 I=1,IMAX
      EX(I)=G2*AK(I)*W(I)
      EX(I)=0.0001*EX(I)
      EX2(I)=EX(I)**2
   12 CONTINUE
      DO 13 I=1,IMAX
      R2(I)=4.0*R(I)
```

TABLE (5.2) Contd.

```
      EX1(I)=EX(I)**2
      R3(I)=V1(I)*EX1(I)
      R4(I)=R2(I)-R3(I)
      R5(I)=SQRT(R4(I))
      R6(I)=1.0+R(I)+R5(I)
      AN(I)=R6(I)/V(I)
      AN2(I)=AN(I)**2
      E1(I)=AN2(I)-EX2(I)
      E2(I)=2.0*AN(I)*EX(I)
      WRITE (6,100) W(I),E(I),R(I),T(I),AK(I),AK12(I),
     1 AN(I),E1(I),E2(I)
  100 FORMAT(4F6.3,F6.1,F6.2,F6.3,F8.5,F7.4)
   13 CONTINUE
      RETURN
      END
ND OF FILE
```

of .6 microns.

5.3.2.2.2 Reflectivity measurements in the visible region

The apparatus used during these measurements was described by Burton (1967).

Measurements were made over the wavelength range of .390 to .640 microns. The polished sample to be examined was levelled by a press on a metal plate and transferred to a small stage where it was kept in a fixed position by small magnets throughout the measurements. This sample carrier stage was fitted on the microscope stage.

The black glass No: 31023 standard, calibrated by National Physics Laboratory was used because of its reflectivity (about 10%) being much closer that of to the samples under investigation.

The reflectivities were measured as intensities of light reflected from the 'black box,' standard and the sample respectively by a photomultiplier in conjunction with a digital voltmeter.

All measurements were taken in air and at room temperature. In order to correct for the primary glare due to reflection from the back of the objective, a 'black box' reading was taken each time and subtracted from the measured standard and sample readings. All readings were taken as maximum and minimum and the reflectivities were calculated using the following equation for both maximum and minimum

$$R = (D_s \times R_{std}) / D_{std} \qquad 5.1$$

where D_s and D_{std} are the digital voltmeter readings after the subtraction of the 'black box' reading.

The experimental er[illegible]pected to be ± 0.5%.

5.3.2.3 Refractive index measurements

In conjunction with the Bellingham & Stanley Ltd. table spectrometer and a Hilger & Watts monochromator, the refractive indices were measured in the visible range, applying the minimum deviation method.

When the light passes through a piece of transparent solid bounded by two faces making an included angle, A, with one another, the light is deviated through an angle at which the light falls on the first face of the prism formed by the inclined faces. When within the prism the light travels in a direction equally inclined to the two faces, the deviation is a minimum and the relation of A and D to the refractive index n is given by

$$n = \mathrm{Sin}\,((A + D)/2) \,/\, \mathrm{Sin}\,A/2 \qquad 5.2$$

Since the maximum value of Sin $1/2\,(A + D)$ is unity there is a limiting value of A equal to $2\,\mathrm{Sin}^{-1}(1/n)$.

The prisms of both 8 and 12 mole % YSZ were cut from the large single as grown crystals. Because the crystal had a cubic structure and was therefore isotropic no special account was taken of orientation. The apex angle A of the prisms was so chosen that it should be less than 30^o according to the above criteria. The prisms were cut by a diamond cutting machine and were polished to a 1/4 micron finish.

CHAPTER 6

EXPERIMENTAL RESULTS AND DISCUSSIONS

CHAPTER 6

EXPERIMENTAL RESULTS AND DISCUSSIONS ON THE PROPERTIES OF AS GROWN AND CURRENT BLACKENED YSZ SAMPLES

6.1 Introduction

This chapter is concerned with the measurements and evaluation of the optical constants of as grown and current blackened YSZ crystals, from their absorption edge down to some lower energy where the phonons are dominating.

The absorption spectra were observed in the wavelength region of .25-2.5 microns. The TT-method (for as grown samples only) or both TT- and RT-methods (for current blackened samples) were used. One part of this study was to determine the energy gap and ultimately to obtain some information on the band structure. The applicability of transition laws based on pure semiconductor crystalline material to a disordered YSZ is discussed.

For transmission, the wavelength region was extended up to 40 microns. The recordings were made generally on single crystal slices though for some details powder forms were also used.

Reflectivities were measured from .39 to 2.5 microns.

The refractive indices were measured at visible wavelengths using the minimum deviation method and a single crystal in the form of a prism.

6.2 Optical absorption spectra of as grown YSZ samples and discussions

6.2.1 Absorption

To determine the position of electronic transitions in YSZ the absorption spectra of the material was examined in the wavelength region of .25 to 2.5 microns.

For this purpose, the absorption coefficient, K, v.s. wavelength curves were derived for both as grown 8 and 12 mole % YSZ samples, (using the TT-method as explained in Chapter 5), from the transmissions recorded for two different thicknesses of the same unoriented samples.

Figure (6.1) shows the positions of both 8 and 12 mole % YSZ curves at room temperature. For both crystals, the absorption constants show a sharp increase at around .271 and .278 microns and have a broad tail extending to .500 and .530 microns respectively.

The sharp increase (absorption edge) will be analysed in section (6.2.2.). The most interesting experimental result is the appearance of an optical tail occurring at the absorption edge. This tail corresponds to the absorption of low energy photons, ($\hbar w < E_g$ where E_g is the forbidden gap energy) and could be interpreted as arising from transitions between localized states; if the density of states varies exponentially with energy, an absorption edge of this form would be expected, Tauc (1969).

Low temperature absorption spectra

At low temperatures the absorption spectra may reveal certain absorption bands due to optical transitions between

---

Fig.(6.1) Absorption coefficient versus wavelength in 8 and 12 mole % YSZ crystals, 1A15e and 2A22j, as grown, at room temperature.

Fig.(6.1)

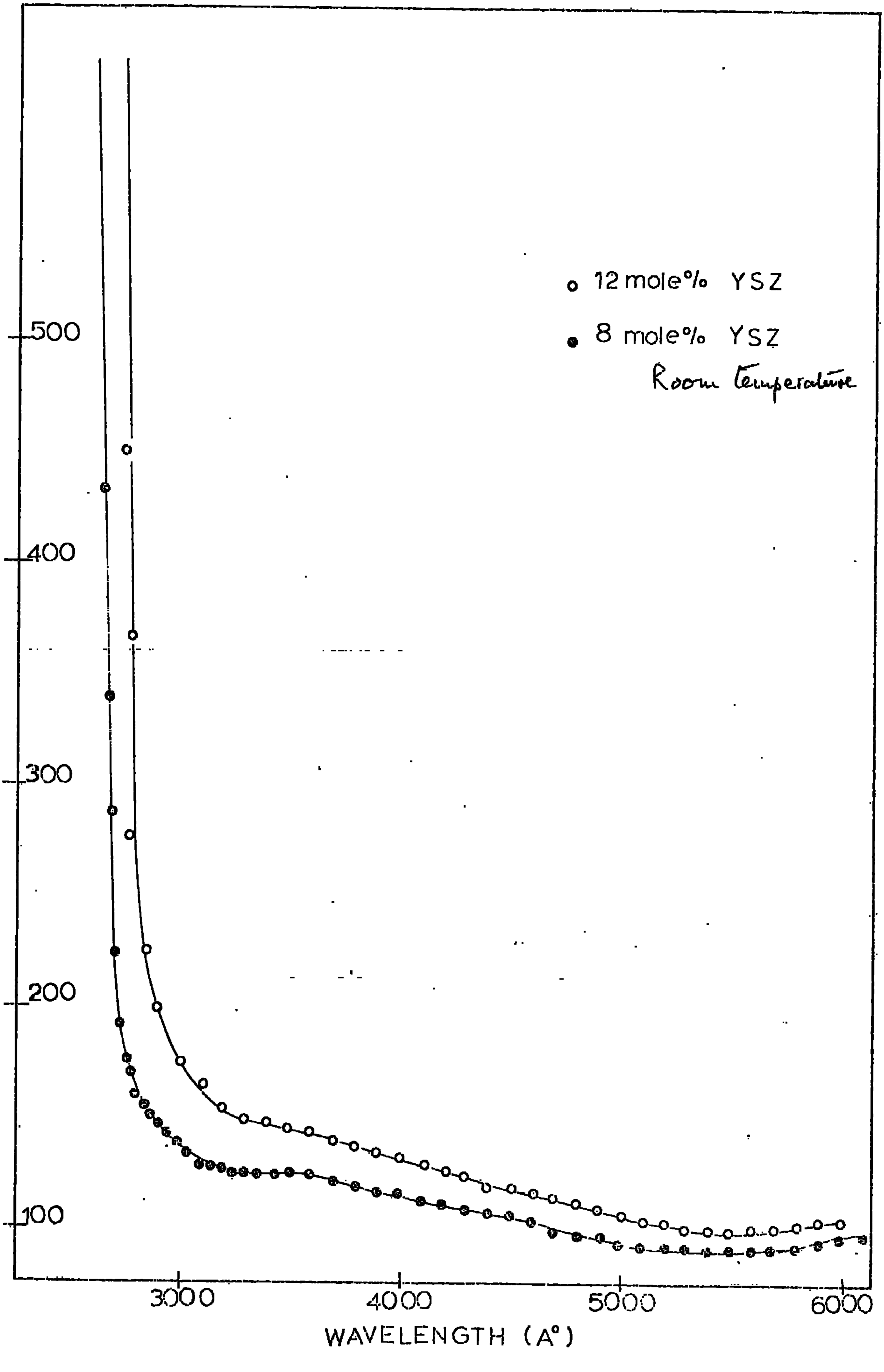
○ 12 mole% YSZ
● 8 mole% YSZ
Room temperature
Absorption Coefficient K (cm^{-1})
500
400
300
200
100
3000
4000
5000
6000
WAVELENGTH (A°)

the ground state and excited energy levels of the impurity in the material. As mentioned in Chapter 3, the expected impurity ions were Zr^{3+} or Y^{2+} which were assigned as the paramagnetic ions causing the type-B line. In fact, the optical spectra of Y^{2+} in CaF_2 reported by O'Connor and Chen (1963) showed four absorption bands at wavelength .225, .335, .400 (the strongest) and .580 microns at 20 °K.

However, the low temperature (~87 °K) absorption spectra of 12 mole % YSZ as grown sample shown in figure (6.2) gave no detectable change; apart from the slight shift of the position of absorption edge, from .278 microns to .268 microns. Thus there is no evidence for the impurities just mentioned. However the experiment should be repeated at temperatures around 20 °K or less to be sure about this interpretation.

6.2.2 Absorption edge

The absorption edge is defined as the point where the slope of the absorption coefficient is a maximum, Moss (1959), p.40. The energy gap determined by extrapolating the short wavelength part of the curve and then finding where the actual absorption coefficient is half the extrapolated value. Thus, on the $\hbar wK$ v.s. $\hbar w$ plots of the two crystals, drawing the extrapolations on the steepest part of the curves, we obtained two band gap energies $Eg_1 = 4.50$ ev and $Eg_2 = 4.45$ ev for the 8 and 12 mole % YSZ samples respectively. The optical energy gap of monoclinic ZrO_2 was found to be .240 microns (4.99 ev) by Bendoraitis and Salomon (1965),

---

Fig.(6.2) Absorption coefficient versus wavelength in 12 mole % YSZ crystal, 2A22j, as grown, at 87 °K.

Fig.(6.2)

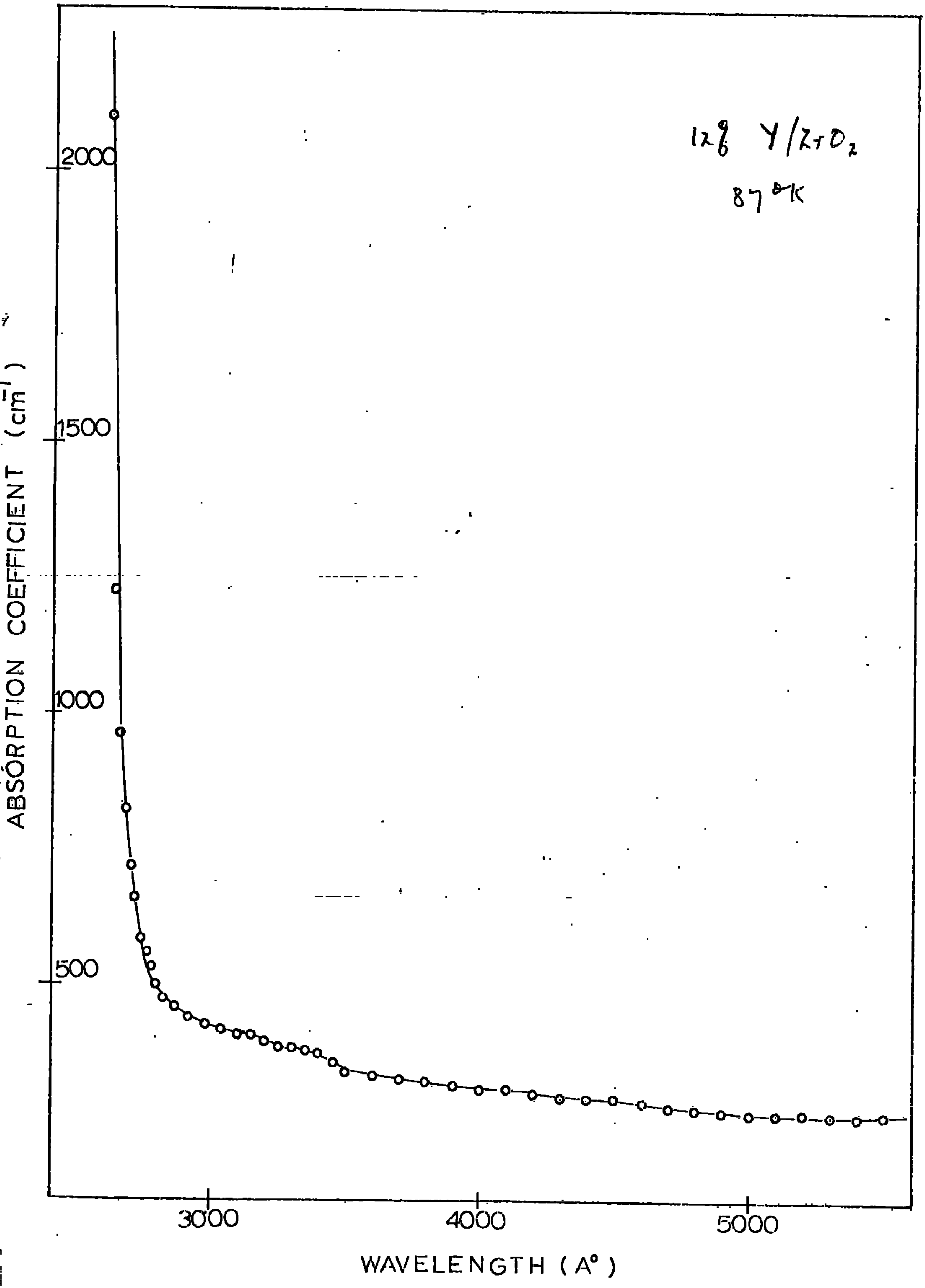
12% Y/ZrO2
87°K
ABSORPTION COEFFICIENT (cm⁻¹)
2000
1500
1000
500
3000
4000
5000
WAVELENGTH (A°)

.230 microns by Conlon and Doyle (1965), which are comparable.

Attempts have been made to fit the curves to the conventional formulae for semiconductors with parabolic bands. The most frequent used expression is (see Chapter 4, section (4.2.2)).

$$K \propto (\hbar w - Eg)^n/\hbar w \qquad 6.1$$

Plots of $\hbar w K$ as a function of photon energy have been drawn (figure (6.3) and figure (6.4) for both 8 and 12 mole % YSZ samples) in an attempt to find a fit with one of the transition laws. The gradients of the separate parts of the curves show that:

For 12 mole % YSZ

Two gradients, n_1 and n_2, change between 3.6 and 1.87 respectively. Hence neither the direct allowed, direct forbidden or indirect forbidden transition rules are satisfied. The only possibility is for an indirect allowed transition for which the gradient should be $n = 2$. Even so, this only seems to be satisfied for the tail region.

For the right hand side of the curve, the gradient n_3 is well above the values which could be fitted to any one of the transition laws.

For 8 mole % YSZ

The same sort of extrapolations give the following gradients, $n_1' = 2$ and $n_2' = 1.4$.

For the highest energy part of the curve, the gradient n_3', is also well above the values to be expected for one of

Fig.(6.3) $\hbar w K$ versus $\hbar w$ curve in 8 mole % YSZ crystal, 1A15e, as grown, at room temperature.

Fig.(6.4) $\hbar w K$ versus $\hbar w$ curve in 12 mole % YSZ crystal, 2A22j, as grown, at room temperature.

Fig.(6.3)

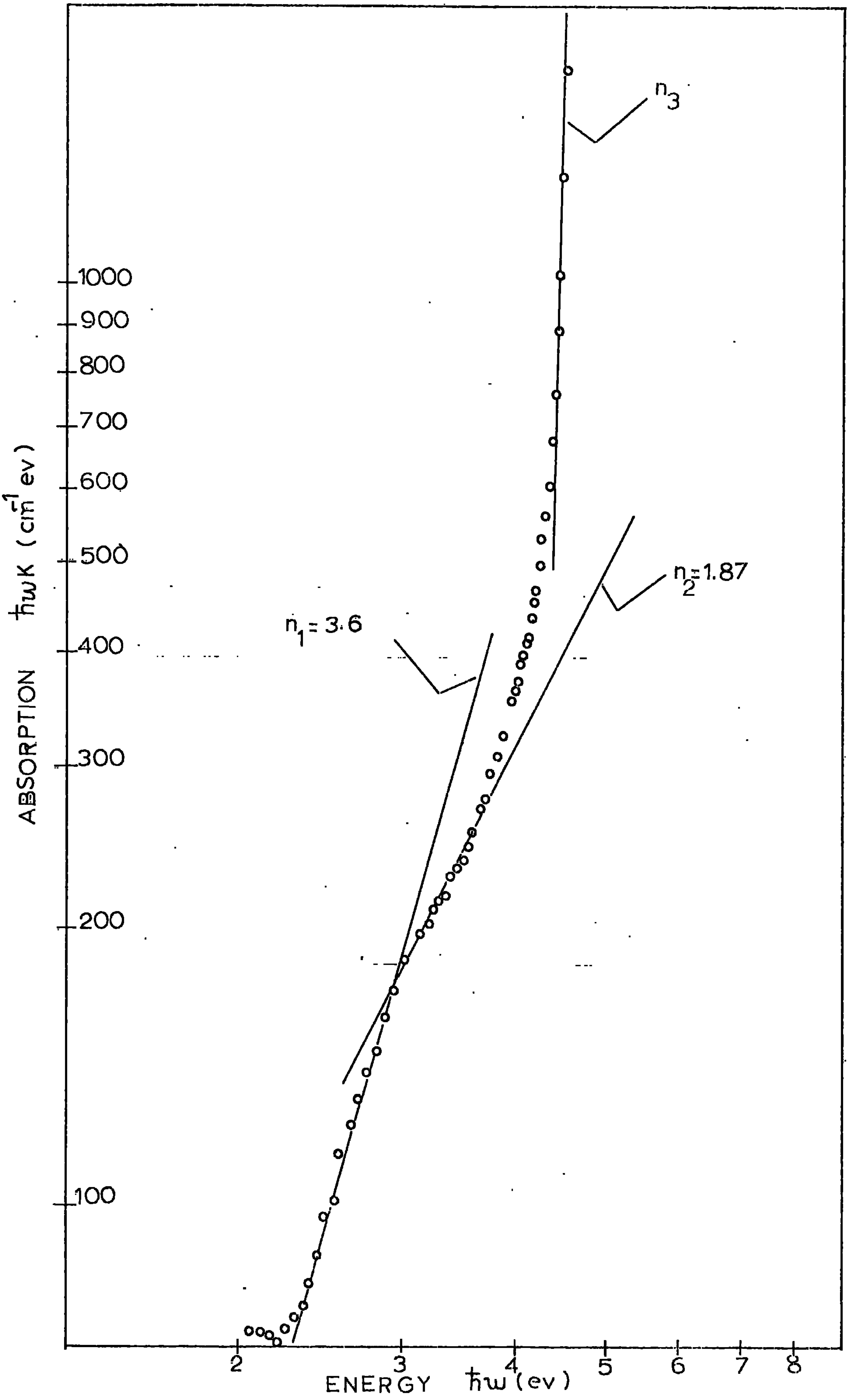

n_3
$n_2 = 1.87$
$n_1 = 3.6$
1000
900
800
700
600
500
400
300
200
100
ABSORPTION $\hbar\omega K$ (cm^{-1} ev)
2
3
4
5
6
7
8
ENERGY $\hbar\omega$ (ev)

Fig.(6.4)

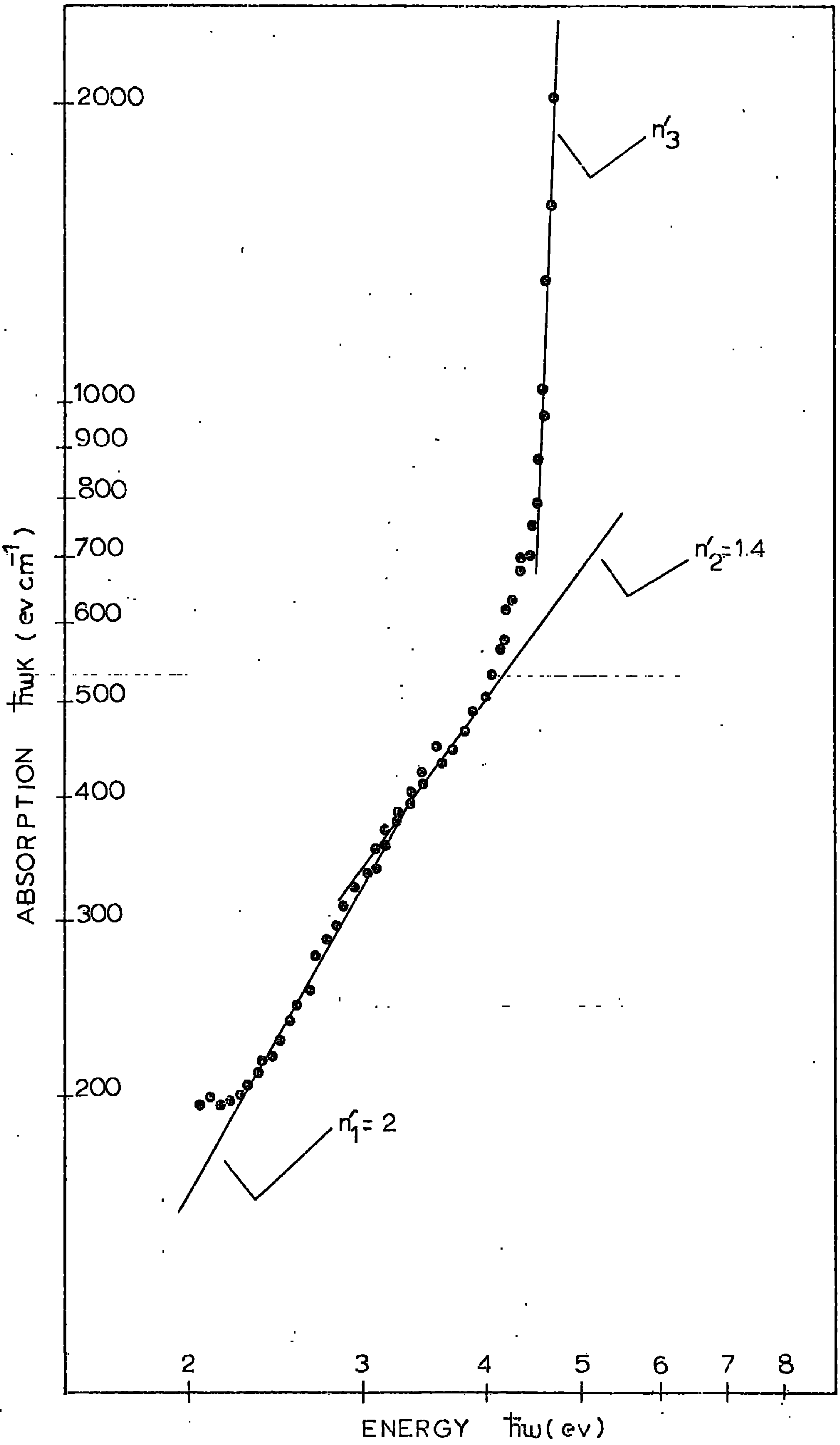
2000
1000
900
800
700
600
500
400
300
200
ABSORPTION ħωK (ev cm^{-1})
n'_3
n'_2=1.4
n'_1= 2
2
3
4
5
6
7
8
ENERGY ħω(ev)

the transition laws.

These results show that the assignment of an optical gap from fitting to formulae of the type given above is a dubious procedure. Furthermore the range of absorption constants accessible to analysis was rather small making it difficult to choose between possible values of n. But it was definitely established that for the slope in the highest energy region n_3 and $n_3' \gg n$ where $n = \frac{1}{2}$ or $n = 2$. This immediately disqualifies the possibility of direct or indirect allowed transitions.

Calculations by Lanyon (1961) and Tauc (1969) show that the variation of the absorption coefficient as a function of photon energy should reflect the rate at which the valence band states fall off with energy into the gap. The slopes of the steepest portion of the edges fall exponentially with photon energy, falling in the ratio e : 1 for a change in energy of 0.06 ev for both types of as grown sample.

Because YSZ crystals are cubic, no orientation dependent changes are to be expected on the absorption edge. The recordings made on the three-fold and four-fold oriented samples showed no difference from the unoriented ones.

6.2.3 Transmission spectra of as grown and current blackened samples in the wavelength region of .25-40 microns

The transmission spectra of as grown 8 and 12 mole % YSZ and current blackened samples were measured on thin single crystal slices in the wavelength region of 0.25-40 microns, using the Optica CF4-DR and Perkin-Elmer model 457 spectrophotometers.

As seen from figure (6.5) the spectra for 8 mole % YSZ

Fig.(6.5) Transmission versus wavelength in 8 mole % YSZ as grown and current blackened crystals, at room temperature.

Fig. (6.5)

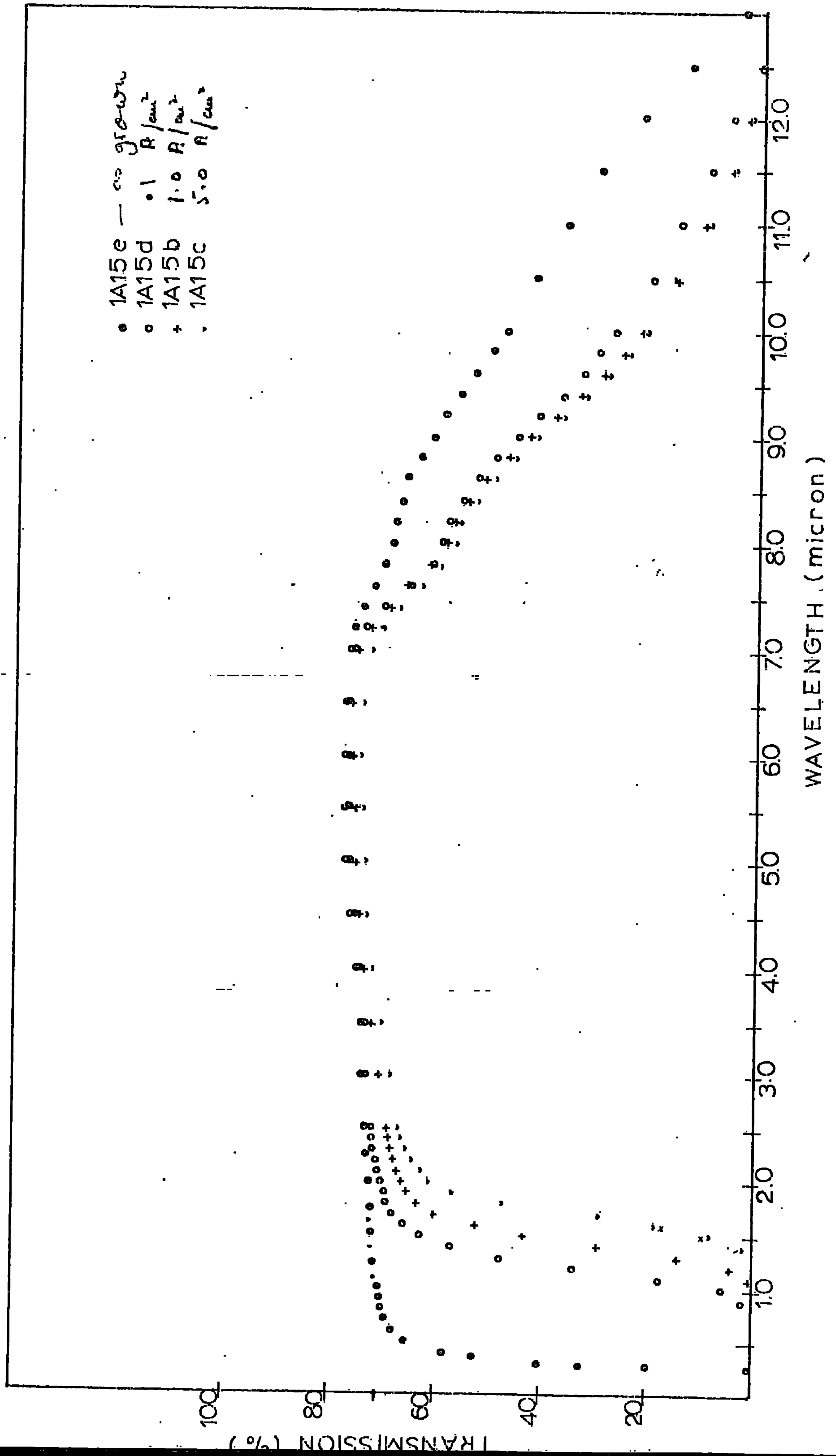

● 1A15e — as grown
○ 1A15d ·1 R/cm²
+ 1A15b 1.0 R/cm²
, 1A15c 5.0 R/cm²
WAVELENGTH (micron)
1.0
2.0
3.0
4.0
5.0
6.0
7.0
8.0
9.0
10.0
11.0
12.0
TRANSMISSION (%)
20
40
60
80
100

are found to be very simple in nature, (similar curves were obtained for 12 mole % YSZ).

The incorporation of OH^- has been shown to occur in a number of materials grown as single crystals by flame fusion, Wickersheim (1961). However, no such band appearing at 2.75 microns was detected in our samples. This is maybe because of the electrofusion growing process. The transmissions go on decreasing in going to the higher wavelength region. The maximum absorption is not clearly observed because of the finite thickness of the available thin samples (less than 32 microns). However thin films of powdered forms of these crystals may be recorded in order to overcome this limitation. This has been done and will be mentioned soon.

The transmission cut offs are listed in Table (6.1) and Table (6.2) together with the thicknesses and the current densities applied to both 8 and 12 mole % YSZ samples respectively. All cut off values were chosen as the values at 1 % transmission. It was found that cut off's were dependent on the crystal thicknesses, for instance, for the thicknesses ranging from 55 to 288 microns of as grown samples, the first cut offs ranged between .255 to .278 microns.

TABLE (6.1)

Transmission cut off values for the as grown and current blackened 8 mole % YSZ samples with different current density and thicknesses at room temperature.

sample	current density (A/cm^2)	thickness (microns)	transmission cutoffs (microns) (first)	(second)
1A15e	as grown	53	0.27	13.0
1A15d	0.1	55	0.90	12.3
1A15b	1.0	65	1.10	12.1
1A15c	5.0	62	1.38	12.1

TABLE (6.2)

Transmission cutoff values for as grown and current blackened 12 mole % YSZ samples with different current density and thicknesses at room temperature.

sample	current density (A/cm^2)	Thickness (microns)	Transmission Cutoffs (microns) first	(second)
2A22j	as grown	54	0.27	13.0
2A22d	0.1	90	0.9	12.1
2A22c	1.0	60	1.1	12.1
2A22b	5.0	140	1.7	9.8

In order to see the comparable transmissions of blackened samples having unblackened and blackened parts, the transmission spectra were recorded, at the junction of both anode and cathode ends, in the wavelength region of 0.25 to 2.5 microns using the Optica spectrophotometer.

The two comparable overlapping transmission curves of the samples (1A15d (8 mole %) and 2A22d (12 mole %)) are seen in figure (6.6). The unblackened, anode end, transmissions increase sharply at around .27 microns in the same way as for as grown samples, and another noticeable but less sharp increase corresponding to the blackened, cathode end, part of the crystal begin at about .65 and .70 microns for the 8 and 12 mole % YSZ respectively.

In semiconductors, absorption due to free, conduction, electrons becomes much more noticeable at long wavelengths. Bearing the possibility of colloidal Zr metal in mind, (created in the current blackened samples), an attempt was made to fit a λ^2-dependence to the absorption curves of our samples Moss (1959), p.29.

Figure (6.6) Transmission versus wavelength in 8 and 12 mole % YSZ crystals, 1A15d and 2A22d, at the junction of the blackened and unblackened parts, at room temperature.

Fig.(6.6)

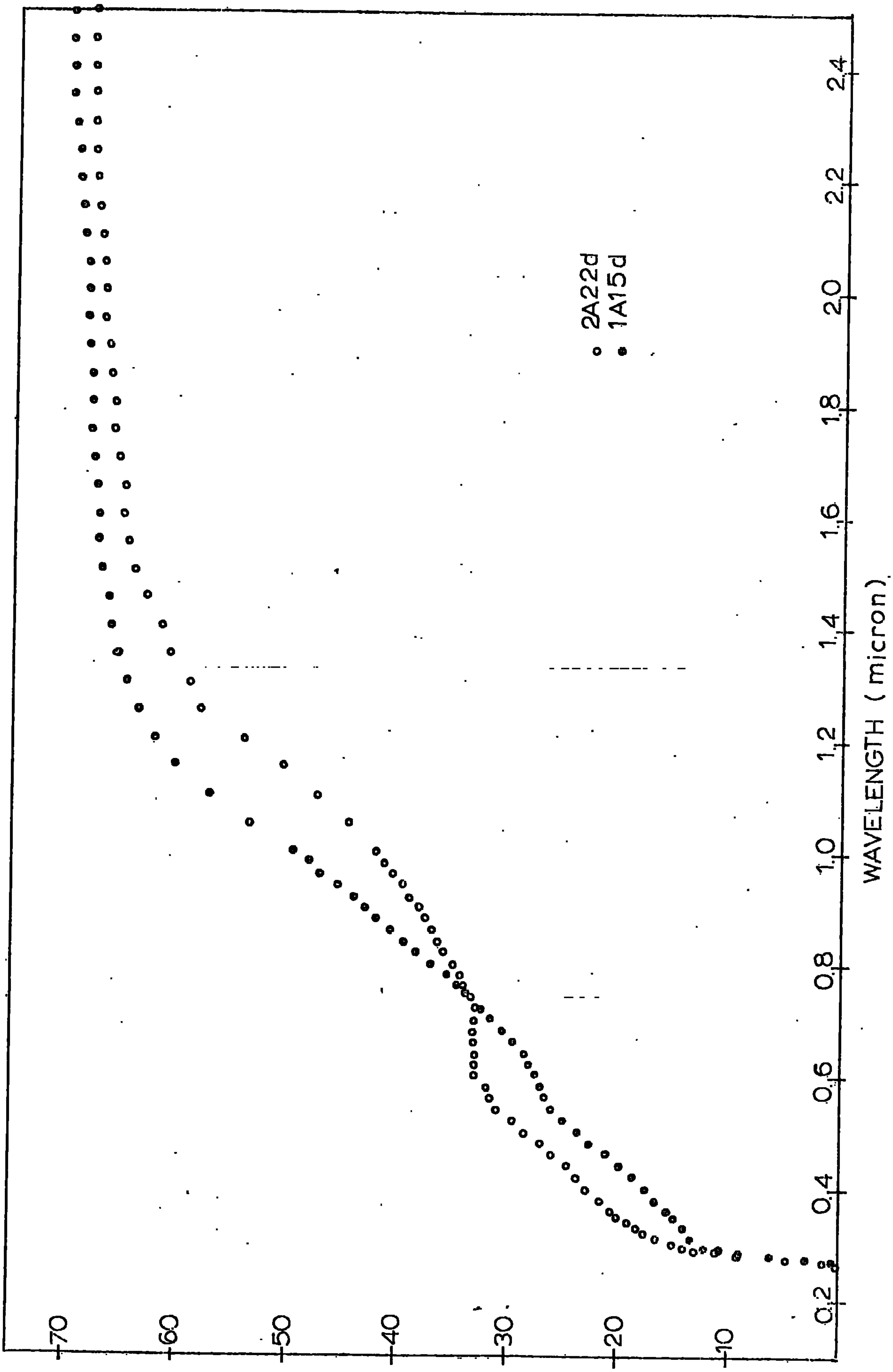
TRANSMISSION (%)
70
60
50
40
30
20
10
WAVELENGTH (micron)
0.2
0.4
0.6
0.8
1.0
1.2
1.4
1.6
1.8
2.0
2.2
2.4
○ 2A22d
● 1A15d

The absorbance v.s. λ^2 curves were drawn on Ln-Ln scales for 8 mole % (as grown 1A15e and blackened 1A15d, 0.1 A/cm^2) and 12 mole % (as grown 2A22j and blackened 2A22d, 0.1 A/cm^2) YSZ samples.

Because YSZ is an insulator no free carrier absorption is expected to be present for the as grown samples. This is verified by the non-linear line shape and the lack of fit of the curves to a square-law dependence.

For blackened samples the slopes of the curves do not satisfy the square-law dependence but straight line is obtained with a gradient of four.

We are inclined to think that the change of the shape and slope on blackening may be explained in the following way. The curvature of the plot for the as grown sample is being perturbed by effects due to free carriers. Hence a straight line is observed for the blackened samples though its slope is greater than two.

Derivation of Debye temperature Θ(I.R.) from infrared transmission data

One definition of a Debye temperature, Θ, is that it is equal to $h\nu/k$ where ν is a characteristic frequency or some average frequency.

A great deal of confusion exists about the assumption that Θ values obtained from different physical properties of a solid should be equal. The simplest case is that Θ (elastic) i.e. the Θ value derived from the elastic constants of a solid, is equal to Θ_D, the value derived from specific heat measurements, if both are measured at sufficiently low temperatures. The measurements made on the reflection of infrared from the surface of crystals and the position of the maximum of the reflection is chosen to evaluate the frequency. The position of the reflection maximum is related to that of the transmission minimum. It is determined principally by the maximum of the reflection coefficient which is found on the short wavelength side of the transmission minimum, Born and Huang (1954), p.123. Hence if one terms the two θ values θ_A(IR) and θ_R(IR) it is found that θ_R(IR) agrees remarkably well with the average value of θ_D whereas the θ_A(IR) values are lower.

"In cubic crystals of the NaCl, of the CsCl type there is only one vibration active in the infrared. In this transverse vibration the positive and negative ions are in antiphase and the wavelength is equal to that of the incident radiation. This natural frequency can best be equal to that of the incident radiation and can best be observed by studying the transmission of infrared through a very thin film of the sample, the minimum of the transmission occurring at the characteristic frequency." Blackmann (1955), p.375.

So the transmission spectra of thin films of powdered YSZ crystals were recorded. The samples were prepared by Mrs. Dubson in the Chemistry Department. A small amount of the sample was powdered and a few milligrams of this powder was mixed with spectroscopically pure CsI. The spectra were recorded on a Perkin-Elmer 457 model double beam grating spectrophotometer. The region was scanned from 250 cm^{-1} to 4000 cm^{-1} and extra care was given to the lower region (250 cm^{-1} to 600 cm^{-1}).

The spectra were found to be similar to the single crystal results and the transmission minimuma were clearly observed at 460 ± 8 cm^{-1} and 464 ± 8 cm^{-1} respectively for

8 and 12 mole % YSZ as grown samples. The corresponding Debye temperatures Θ_Λ(IR) derived from these transmission results and the θ (elastic) values obtained by Pace et al. (1969) for our samples are compared in Table (6.3).

TABLE (6.3)

Comparison of Debye temperatures for 8 and 12 mole % YSZ as grown crystals obtained from I.R. measurements and from elastic constant extrapolated to 0 °K.

Crystal	Debye temperature (in °K) Θ_Λ(IR)	θ_o(elastic)
8 mole % YSZ	660 ± 12	595
12 mole % YSZ	666 ± 12	604

The Debye temperatures derived from IR transmission data are bigger than the values obtained with the ultrasonic methods though theory suggests they should be lower.

In similar measurements on a current blackened 12 mole % YSZ sample (2A22e, 20 A/cm^2, 15 m, 800 °C, in argon) the spectrum was found to include an extra absorption band peaking at 1080 cm^{-1}. However there was only shift or shape distortion of the wide band centred at 464 ± 8 for the single crystal slices with the low current densities.

6.3 Reflectivity spectra of as grown and current blackened samples

6.3.1 Visible region (.39-.66 microns)

The reflectivities of as grown and current blackened samples of both 8 and 12 mole YSZ samples were measured in the wavelength region of .39-.66 microns using the instrument mentioned in Chapter 5 section (5.3.2.2.2). The standard chosen was black glass no: 31025 because of having the closest reflectivity to YSZ.

The measurements for as grown transparent material were made on prism shaped samples, polished to a 1/4 micron finish so that multiple reflections would be prevented. However the measurements on the current blackened samples were made on thin polished slices because they were not transparent in the visible wavelengths.

As grown samples

Figure (6.7) shows that the reflectivities of 8 and 12 mole % YSZ as grown samples, being around 12 and 14 % in the visible region. An increase is observed for the lower wavelength-end of the spectra for both kinds of samples. This is in agreement with the expected rise in the neighbourhood of the absorption edge. In fact the diffuse reflectance spectra of 8 mole % YSZ recorded in the wavelength region of 0.3-1.0 microns gave sharp rise between 0.3 and 0.6 microns. The spectra were recorded at room temperature with ring-type reflectance attachment to the instrument SP.500; $MgCo_3$ was used as the standard.

The refractive index measurements in the same wavelength region using the minimum deviation method also gave consistent results for the reflection coefficients see section (6.4).

Current blackened samples

The reflectivities of the current blackened 8 and 12 mole % YSZ samples, for the current densities of 0.1 A/cm^2, 1.0 A/cm^2, 5.0 A/cm^2 were measured using the same method and apparatus.

The reflection coefficients for 8 and 12 mole % YSZ

Fig.(6.7) Reflection coefficient versus wavelength in 8 and 12 mole % YSZ crystals, as grown, visible region.

Fig.(6.7)

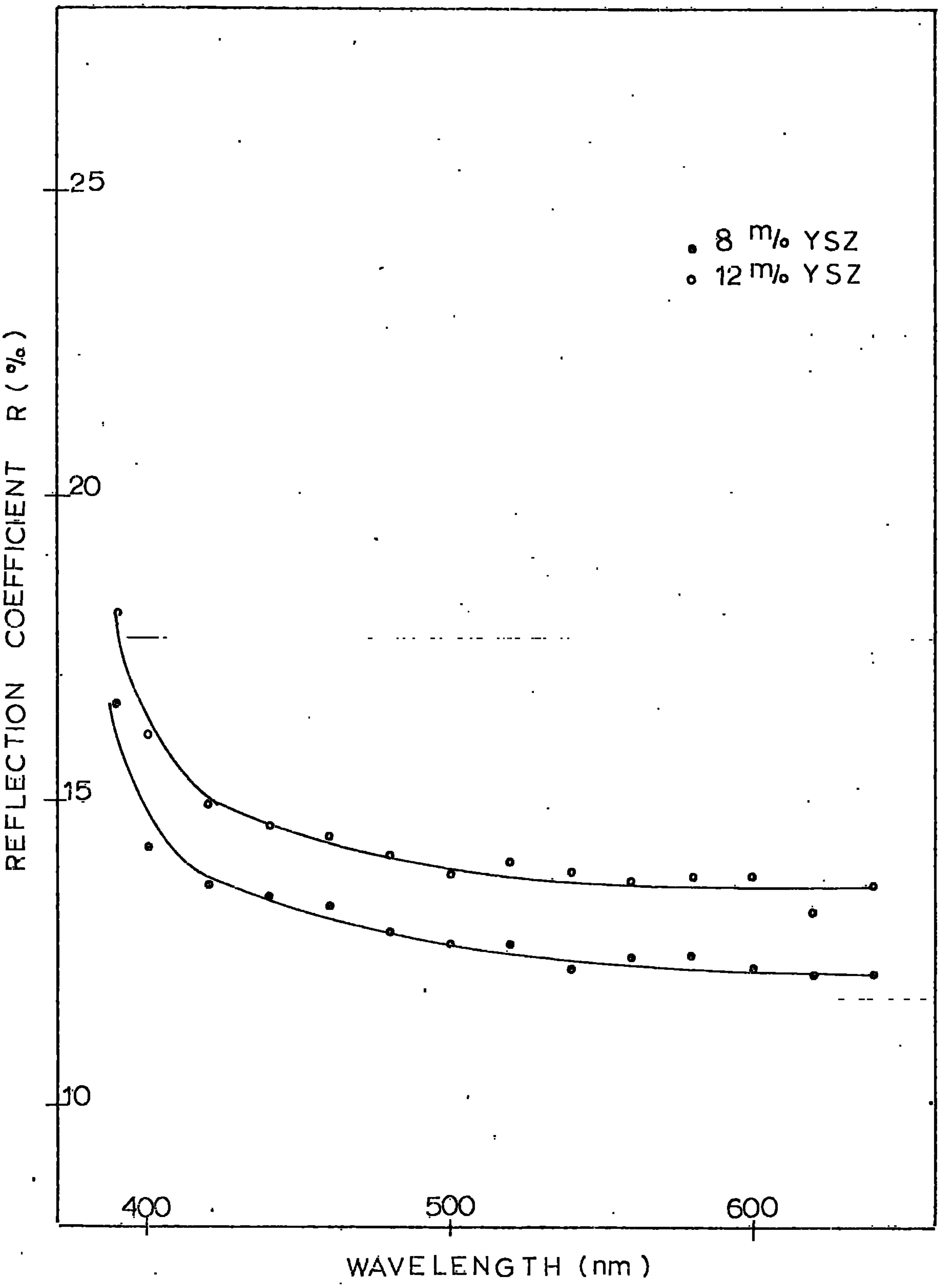

● 8 m/o YSZ
○ 12 m/o YSZ
25
20
15
10
REFLECTION COEFFICIENT R (%)
400
500
600
WAVELENGTH (nm)

samples blackened to different degrees are given in Table (6.4).

TABLE (6.4)

Average reflectivities of 8 and 12 mole % YSZ crystals, current blackened, visible region

Wave-length (nm)	8 mole % YSZ			12 mole % YSZ		
	1A15d	1A15b	1A15c	2A23c	2A22c	2A22i
390	14.64	15.18	14.00	15.27	14.54	15.59
400	15.29	14.70	14.05	14.81	14.47	14.67
420	14.72	15.23	13.74	14.86	14.23	14.62
440	14.61	14.54	13.68	14.68	14.13	14.74
460	14.56	14.48	13.47	14.56	13.93	15.02
480	14.40	14.49	13.36	14.37	13.75	14.82
500	14.33	14.36	13.45	18.17	13.61	14.59
520	14.11	14.18	13.94	13.99	13.62	14.52
540	13.80	14.06	13.29	13.89	13.57	14.61
560	13.85	14.06	13.36	13.77	13.82	14.51
580	13.91	14.19	13.42	14.15	13.79	14.58
600	13.96	14.21	13.60	13.93	13.60	14.48
620	13.84	14.18	13.50	13.79	13.84	14.38
640	13.31	14.05	13.67	13.86	13.74	14.98
660	13.74	13.79	13.46	13.93	13.76	-
Current density (A/cm^2)	.1	1.0	5.0	.1	1.0	5.0

6.3.2 Near Infrared region (0.6-2.5 microns)

In this section, only reflectivity measurements of current blackened 8 and 12 mole % YSZ samples will be mentioned.

The sample preparation and the method employed are described in Chapter 5, section (5.2.1.2) and section (5.3.2.2.1).

In Table (6.5) reflection coefficients are given for both groups of samples. There was no structure in the spectra. The fluctuations ranging within 0.4% may be considered due to experimental errors.

TABLE (6.5)

Reflection coefficients of 8 and 12 mole % YSZ crystals current blackened, near infrared region

Wave-length (microns)	8 mole % YSZ			12 mole % YSZ		
	1A15d	1A15b	1A15c	2A22d	2A22c	2A22b
0.659	13.80	13.80	13.35	13.95	13.65	14.40
0.675	13.80	13.80	13.35	13.95	13.60	14.40
0.696	13.75	13.70	13.35	13.30	13.60	14.40
0.715	13.80	13.80	13.35	13.80	13.50	14.45
0.740	13.85	13.75	13.40	13.85	13.65	14.45
0.760	13.75	13.85	13.40	13.75	13.65	14.45
0.797	13.90	13.85	13.30	13.80	13.65	14.50
0.826	13.95	13.90	13.55	13.85	13.75	14.55
0.861	13.30	14.10	13.60	13.95	13.80	14.65
0.898	13.85	14.15	13.50	14.05	13.80	14.65
0.939	13.85	14.15	13.35	14.05	13.75	14.55
0.984	13.80	14.05	13.25	14.05	13.65	14.50
7.024	13.80	13.95	13.25	14.00	13.60	14.50
1.078	13.75	13.95	13.20	13.95	13.60	14.50
1.127	13.75	13.90	13.30	13.95	13.60	14.50
1.180	13.75	13.85	13.30	13.85	13.50	14.50
1.227	13.75	13.80	13.20	13.80	13.50	14.50
1.284	13.75	13.80	13.20	13.80	13.50	14.50
1.347	13.75	13.75	13.20	13.75	13.50	14.50
1.409	13.75	13.75	13.20	13.75	13.50	14.50
1.485	13.75	13.75	13.20	13.75	13.50	14.50
1.550	13.80	13.85	13.20	13.75	13.50	14.50
1.642	13.75	13.70	13.20	13.65	13.50	14.50
1.722	13.75	13.80	13.20	13.70	13.50	14.50
1.837	13.80	13.85	13.25	13.70	13.55	14.55
1.937	13.80	13.85	13.25	13.70	13.55	14.55
2.049	13.80	13.80	13.20	13.70	13.55	14.55
2.179	13.75	13.20	13.20	13.65	13.55	14.50
2.339	13.80	13.75	13.20	13.65	13.55	14.50
2.530	13.80	13.80	13.20	13.70	13.55	14.55
Current density (A/cm^2)	.1	1.0	5.0	.1	1.0	5.0

6.4 Refractive indices of as grown samples

The prisms of 8 and 12 mole % YSZ with apex angles of 22°44' and 23°04' were cut from large single as grown crystals. Because the crystals had a cubic structure and were therefore isotropic no special account was taken of orientation.

For crystal preparation and the method employed see Chapter 5, section (5.3.2.3).

The results of refractive indices for both types of samples are given in Table (6.6).

TABLE (6.6)

The refractive indices of 8 and 12 mole % YSZ crystals, as grown, minimum deviation method, visible region

Wavelength (millimicrons)	Refractive indices 8 mole % YSZ	12 mole % YSZ
490	-	2.194 ∓ 0.004
500	-	2.193
510	-	2.188
520	2.191 ∓ 0.004	2.185
530	2.191	2.181
540	2.191	2.177
550	2.188	2.174
560	2.188	2.172
570	2.183	2.171
580	2.180	2.166
590	2.183	2.166
600	2.180	2.158
610	2.166	2.158
620	2.175	2.156
630	2.170	2.155
640	2.177	2.154
650	2.167	2.154
660	2.160	2.152
670	2.159	2.154

6.5 Optical absorption spectra of current blackened samples and discussions

6.5.1 Absorption (wavelength region .25-2.5 microns)

The absorption spectra of current blackened samples showed several new features compared with as grown ones.

The two methods (TT and RT) were applied in order to derive the absorption curves. They are in agreement with each other and are given in the following section (6.5.1.1) and section (6.5.1.2) respectively.

6.5.1.1 TT-method

Transmission recordings for two different thicknesses of each current blackened sample enabled the absorption v.s. wavelength curves to be derived for several values of current density.

Figure (6.8) shows the absorption plots of current blackened and as grown 8 mole % YSZ samples at room temperatures.

Several features stucking to the attention at first sight may be given as follows.

1. Absorption spectra of as grown and unblackened part of the current passed samples gave overlapped wavelength dependence as will be seen on the far left of figure (6.8).
2. Absorption spectra of differently current blackened samples (1A15d, 1A15b, 1A15c see Table (6.1) for current densities) showed certain shifts between themselves, shifting to the longer wavelengths as the current densities applied increased.
3. The absorption spectra of all the blackened samples seemed shifted from .27 microns to beyond the 1 micron.
4. The sample current treated with the current density of .1 A/cm^2 was blackened and this value was found the lowest limit value for the observable shift of the absorption spectra. The samples current passed with the densities of 20, 40, and 80 mA/cm^2 were not blackened and they did not show any shift at all.

The measurements made at low temperatures (87 ^{o}K),

Fig.(6.8) Absorption coefficient versus wavelength in 8 mole % YSZ crystals, 1A15d, 1A15b, 1A15c, current blackened, TT-method at room temperature.

Fig. (6.8)

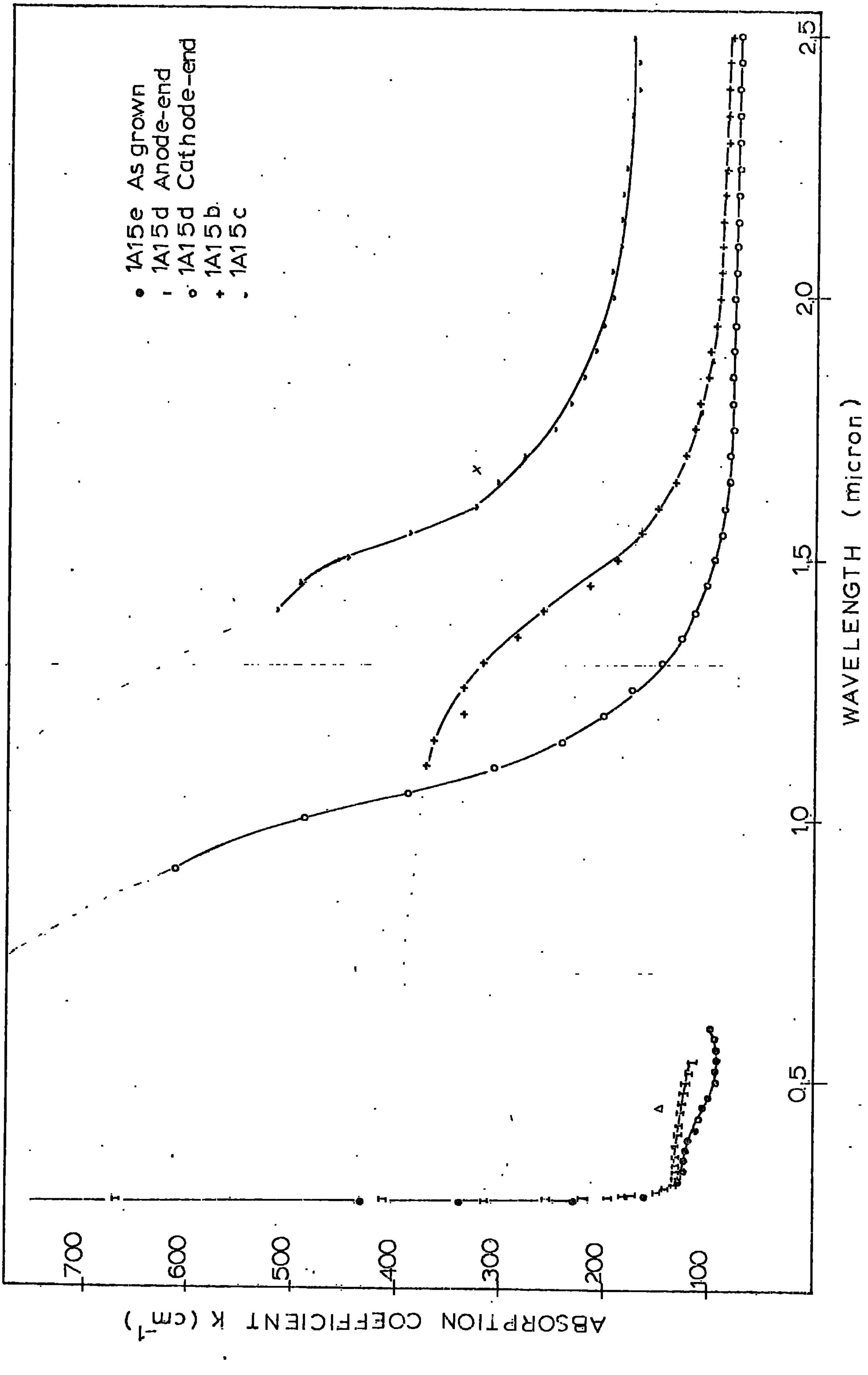
● 1A15e As grown
ı 1A15d Anode-end
o 1A15d Cathode-end
+ 1A15b
, 1A15c
ABSORPTION COEFFICIENT K (cm^{-1})
100
200
300
400
500
600
700
WAVELENGTH (micron)
0.5
1.0
1.5
2.0
2.5

gave similar results of the room temperature (Figure (6.9)). They seemed there were no intensity changes.

Similar spectrum was observed for current blackened 12 mole % YSZ crystal 2A22c (1.0 A/cm^2), at room temperature. The same conclusions said for the 8 mole % YSZ can be said to 12 mole % YSZ as well.

Some discussable points about blackened sample spectra will be delayed for the time being until the RT-method results of absorption spectra are presented in the following section (6.5.1.2).

6.5.1.2 RT-method

In order to get alternative results for the spectral distribution of the absorption, to compare with those obtained from the application of the TT-method, the RT-method was used. See Chapter 5, section (5.3.2.1.2).

The samples were 8 mole % YSZ 1A15d, 1A15b, 1A15c. First, as seen in section (6.3.2) of this chapter, the reflection coefficients were measured on one polished surface. Then the samples were ground down to thicknesses around 100 microns and polished to 1/4 micron, and the transmissions were recorded. From the resulting spectra, using the computer programme mentioned in Chapter 5, Table (5.2), the absorption constants, K, were measured. The same procedure was applied to the 12 mole % YSZ samples 2A22d, 2A22c, 2A22b.

Fig.(6.9) Absorption coefficient versus wavelength in 8 mole % YSZ crystals, 1A15d, 1A15b, 1A15c, current blackened, TT-method, at 87 °K.

Fig.(6.9)

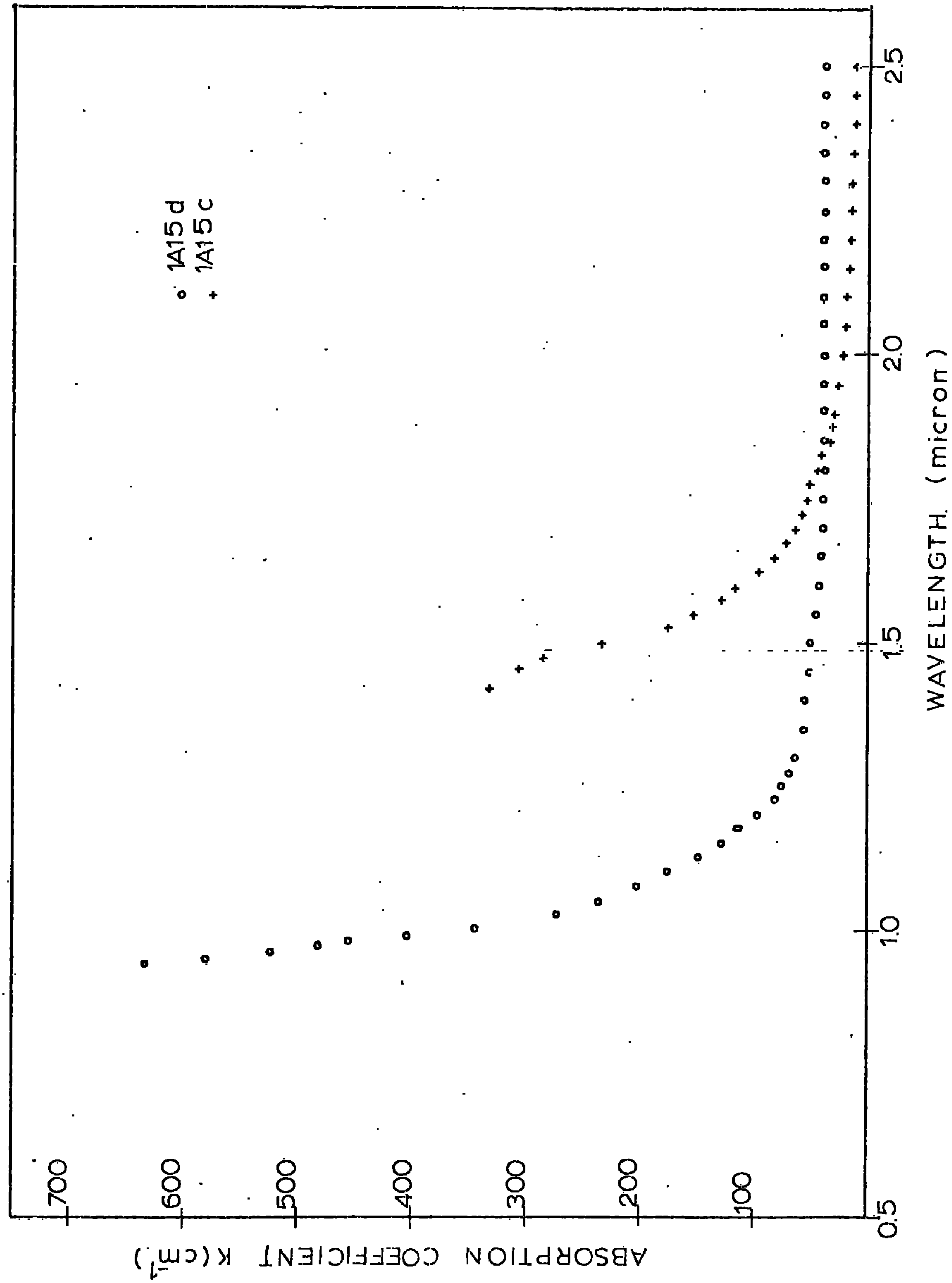

o 1A15 d
+ 1A15 c
ABSORPTION COEFFICIENT K (cm^{-1})
700
600
500
400
300
200
100
WAVELENGTH (micron)
0.5
1.0
1.5
2.0
2.5

In Figure (6.10) and Figure (6.11) absorption coefficient versus wavelength curves are seen for the 8 and 12 mole % current blackened (see Table (6.1) and (6.2) for blackening conditions) YSZ samples respectively. For comparison, the spectra which were obtained for as grown samples using the TT-method are also included.

The spectra obtained with both the RT-method and the TT-method gave non-linear shifts of the absorption curves for the current blackened samples, as compared with the as grown crystal spectra of both 8 and 12 mole % YSZ. This must be connected with absorption band broadening due to some change in the material. Interpretation of these shifts as due to a change in position of the genuine absorption edge is not tenable because the crystal lattice parameter is known from x-ray evidence to remain unaltered by current blackening.

The reflectivity measurements of the blackened samples in the visible region were most interesting because, as was seen in section (6.2.3) of this chapter, the transmission spectra recorded in this wavelength region gave 0 % transmission, so that we could not observe any absorption by the material.

Fig.(6.10) Absorption coefficient versus wavelength in 8 mole % YSZ crystals, 1A15d, 1A15b, 1A15c, current blackened, RT-method, at room temperature.

Fig.(6.11) Absorption coefficient versus wavelength in 12 mole % YSZ crystals, 2A22d, 2A22c, 2A22b, current blackened, RT-method, at room temperature.

Fig. (6.10)

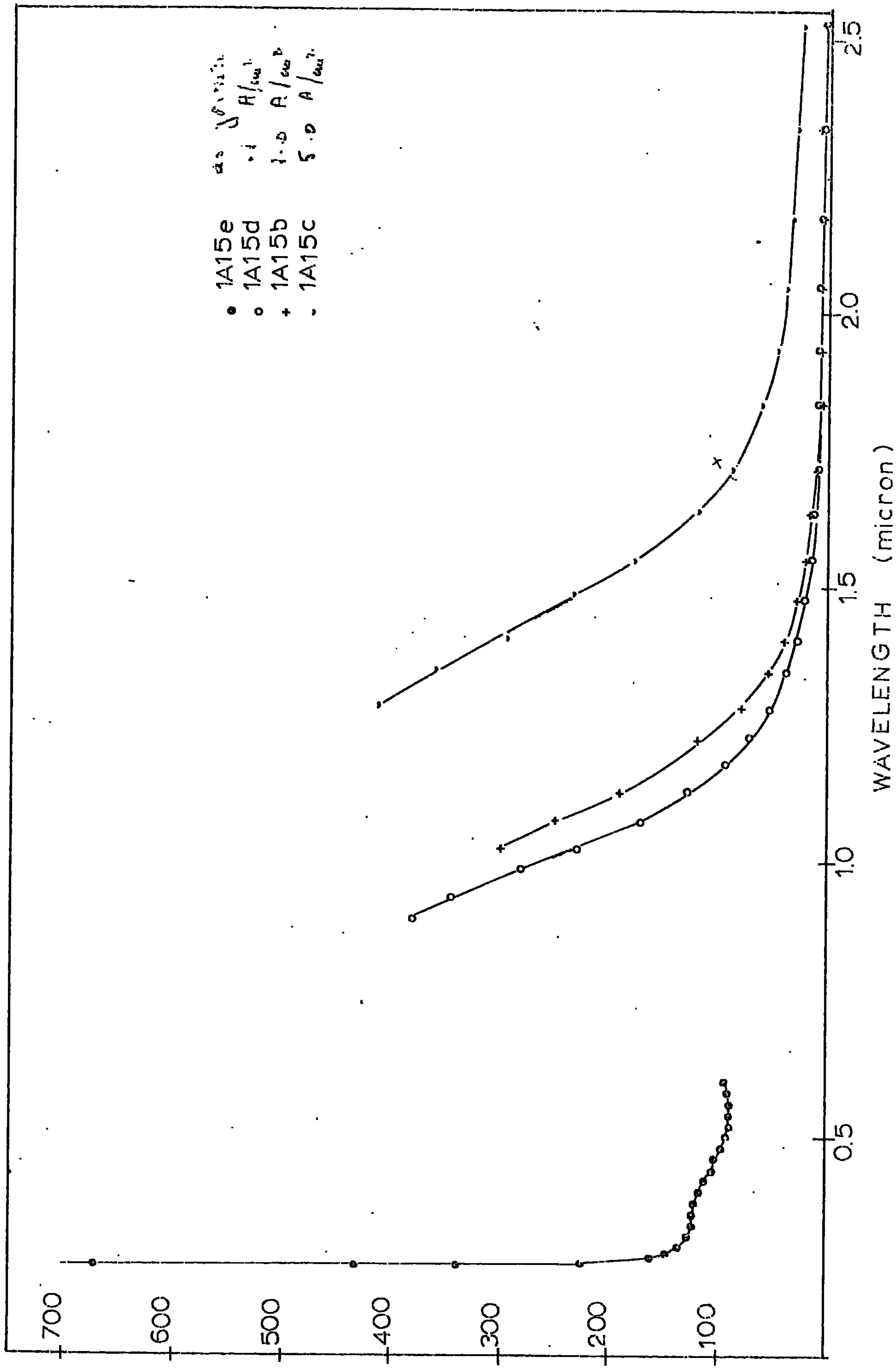

ABSORPTION CONSTANT K (cm^{-1})
700
600
500
400
300
200
100
WAVELENGTH (micron)
0.5
1.0
1.5
2.0
2.5
● 1A15e as grown
○ 1A15d 0.1 A/cm^2
+ 1A15b 1.0 A/cm^2
, 1A15c 5.0 A/cm^2

Fig. (6.11)

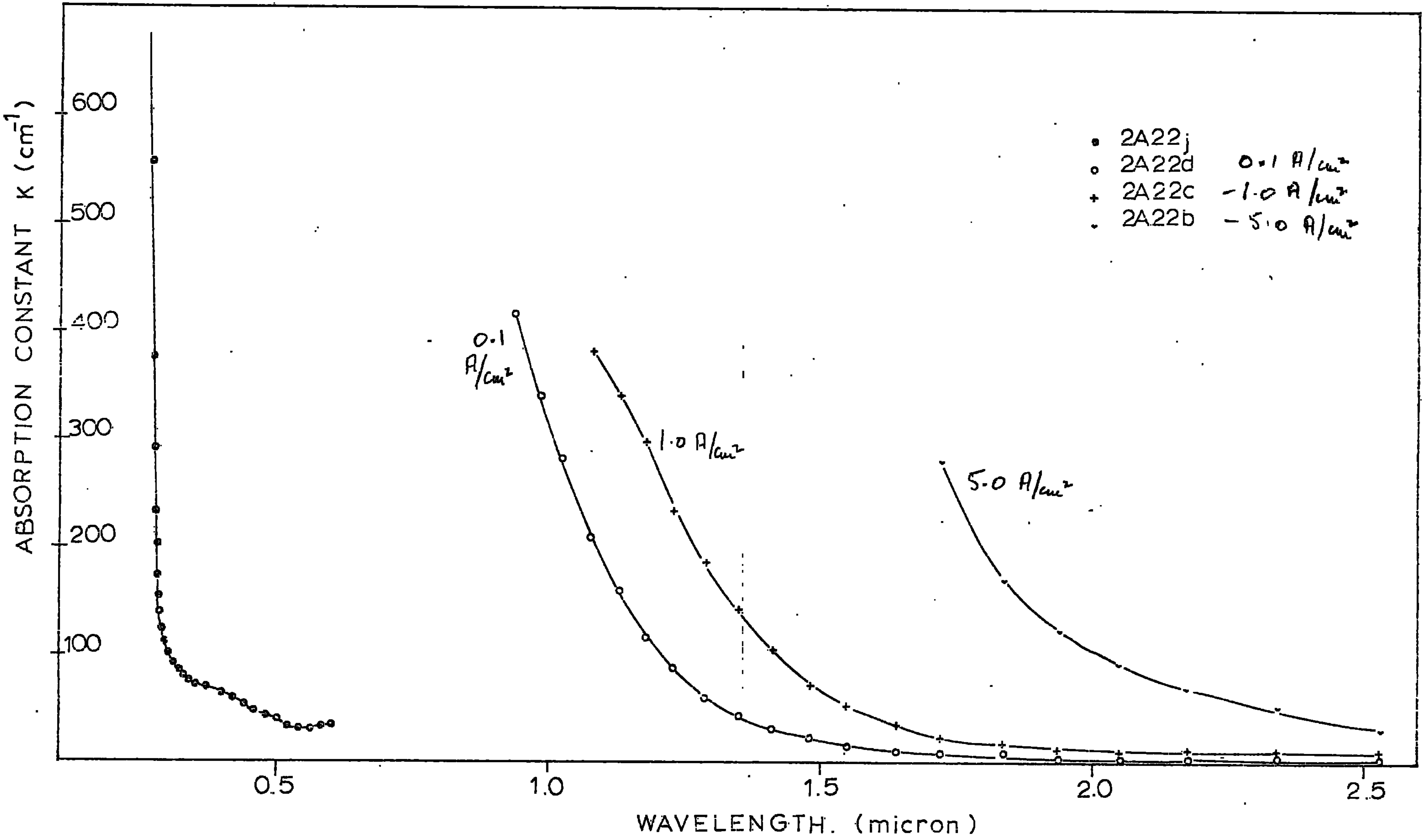
ABSORPTION CONSTANT K (cm^{-1})
600
500
400
300
200
100
0.5
1.0
1.5
2.0
2.5
WAVELENGTH. (micron)
• 2A22j
○ 2A22d 0.1 A/cm²
+ 2A22c -1.0 A/cm²
· 2A22b -5.0 A/cm²
0.1 A/cm²
1.0 A/cm²
5.0 A/cm²

The conservation of energy dictates that Kruse et al. (1963), p.139, the following equation is satisfied.

$$T + R + K = 1 \qquad 6.2$$

where T, R and K are given by the meanings in equ.(4.13) and equ.(4.14) respectively in Chapter 4. It is immediately clear that because of the T is zero for blackened samples in the visible region, R is about 14% and it is likely that K is roughly the same as in as grown crystals, there must be some other type of compensating contribution in the equ.(6.2), such as scattering, which it is not possible to detect in the present transmission or reflectivity measurements.

CHAPTER 7

GENERAL CONCLUSION

CHAPTER 7

GENERAL CONCLUSION

In the present work the main interest was to attempt to elucidate the nature of blackened YSZ. By comparison of the properties of as grown crystals with those of material blackened by current passage.

It is convenient to summarize the main conclusions.

The present e.p.r. work showed that:

1. Oxygen vacancies

The existence of oxygen vacancies, which has previously been assumed, (due to charge compensation arising from the structure of the solid solution and by inference from the observed electrical properties) has been confirmed with e.p.r. The observation of a trapped electron, its symmetry properties, the ways of destroying and recreating this centre by heat treatment, vacuum reduction and current passage processes very closely established that type-A lines were due to oxygen vacancies with trapped electrons.

2. Valency change of constituent cations of YSZ

The assignment of the type-B spectra observed in as grown samples has not been easy. This was because of its structureless, asymmetrical appearance. The stability of its behaviour despite heat treatments shows that it is not a colour centre and allowed us to consider that the most probable candidates were the transition metal ions Zr^{3+} or Y^{2+}. Confirmation of the presence of these ions might come from the optical absorption spectra. Unfortunately 4d ions are not observed as easily as rare earth or 3d ions as sharp and narrow bands.

3. Conduction electrons of Zr-metal

From the e.p.r. point of view the only major difference between as grown and blackened material was the occurrence of a single type-C line, whose intensity increased with increasing applied current density. Interpretation of this line seemed to be more reasonable if it is assigned as due to conduction electrons, most likely of Zr-metal.

The study of the optical properties showed that:

1. Shift of apparent absorption edge

Non-linear shifts of the absorption curves were observed for the blackened material compared with the absorption edge position for the as grown crystals. Explanation of these shifts as due to a change in position of the genuine absorption edge is not tenable because the crystal lattice parameter is known to remain unaltered.

However, a parallel can be found in the way that the "change" during the blackening, effecting the intensity increment of the type-C line and the shift of the optical absorption curves with increasing current density is due to the same origin. That is, both observations from the two different methods (epr and optical) can be considered to be due to the same "cause."

2. Transmission minimuma in the near I.R. wavelength region allowed the same unchanged Debye temperatures in room temperature to be calculated for both as grown and blackened crystals. However there was broadened appearance of the absorption band in the case of blackening which may be attributed due to perturbation by the conduction electrons. On the other hand the extra band observed at 1080 cm^{-1} (Θ_A(IR) = 1050 °K) does not seem related with Zr-metal. Because Debye temperature of Zr-metal is 292°K see Kittel

(1966), p.180.

3. Reflectivity in the visible region does not change for as grown and current blackened crystals.

Previous work Casselton et al.(1971) indicated that blackening might be associated with the formation of colloidal particles of Zr-metal. In blackened samples pronounced optical scattering was observed.

Thus a major objective was to see whether this colloidal model could explain the e.p.r. and optical results. Before attempting this, it is helpful to keep in mind the results from complimentary experiments relating to the nature of blackened YSZ.

These results are summarized below.

1. Ultrasonic measurements

The elastic constants of as grown YSZ were found from ultrasonic measurements Pace et al. (1969).

Recently, the corresponding elastic constants have been measured in a current blackened 8 mole % YSZ single crystal by J. S. Ross and T. M. Farley by the ultrasonic pulse superposition technique. The elastic constants are the same for as grown and blackened material. The ultrasonic data also confirms that the lattice is unchanged and hence indicates that in the optical work, the position of the genuine band edge should remain unaltered on blackening.

2. Dielectric constant

Dielectric constant measurements have been made by J. S. Ross and H. M. Buckley on as grown and blackened YSZ.

In as grown material measurements at 10^3 Hz showed that the relative dielectric constant ϵ_r is about 32 for both 8 and 12 mole % YSZ. There was however a considerable variation between nominally identical as grown samples.

Other measurements made by microwave methods at 35 GHz show that on blackening the dielectric constant increases very considerably e.g. from about 40-50 for an as grown single crystal to about 100 after current blackening. The interest will be to see if the increase in ϵ_r is consistent with the postulate of the formation of metallic particles within the dielectric.

An explanation of absorption curves for blackened material can be suggested. Assume that the colloidal particles are Zr-metal. At very low current densities the particle size will be small. As the current density increases, the particle size will tend to increase and the result will be a distribution of particle size.

The effects of particle size on absorption and scattering characteristic are discussed by Savostianova (1930) who applied the Mie (1908) theory to the case of colloidal sodium in rock salt and obtained the curves for absorption and scattering shown in figure (7.1).

The suggestion is that in the blackened crystal we are observing the resultant of a genuine absorption curve on which a scattering curve is superimposed, figure (7.2). Where (a) is the absorption curve of the as grown material (see fig.(6.1)), (b) is the scattering curve of current blackened material, (see Casselton et al. (1971) figure (7) and (c) is the absorption curve of the blackened material with the lowest current density (see fig.(6.10)).

The apparent shift of (c) to longer wavelengths at higher current densities can be explained by assuming that the particle size increases and that the width of the

Fig.(7.1)

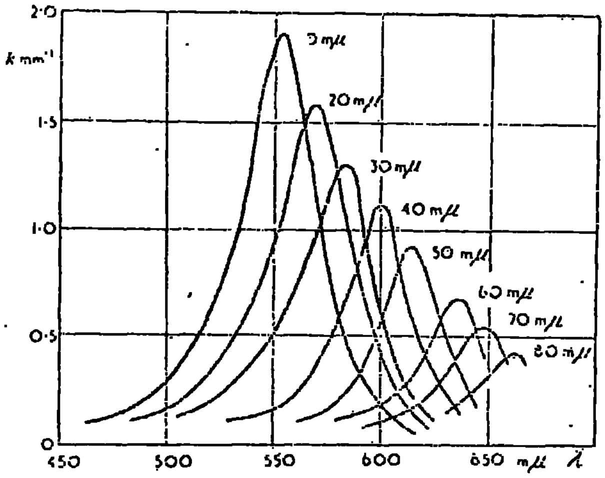

Fig. 26. Absorption curves of the system Na-NaCl for a volume ratio of Na to NaCl 10^{-6} (after SAVOSTIANOWA)

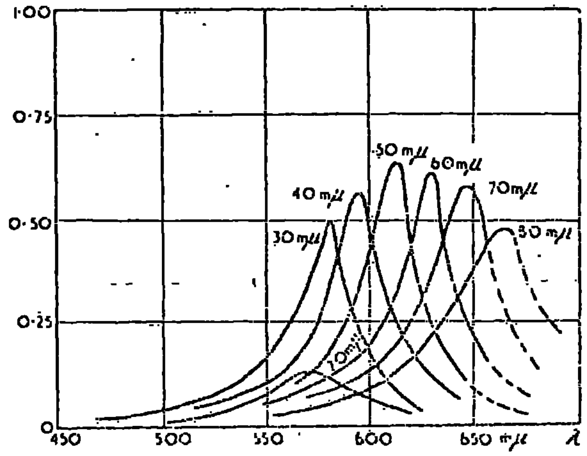

Fig. 27. Scattering curves for the system Na-NaCl per cm^3: vol. conc. 10^{-6} (after SAVOSTIANOWA)

Fig. (7.2)

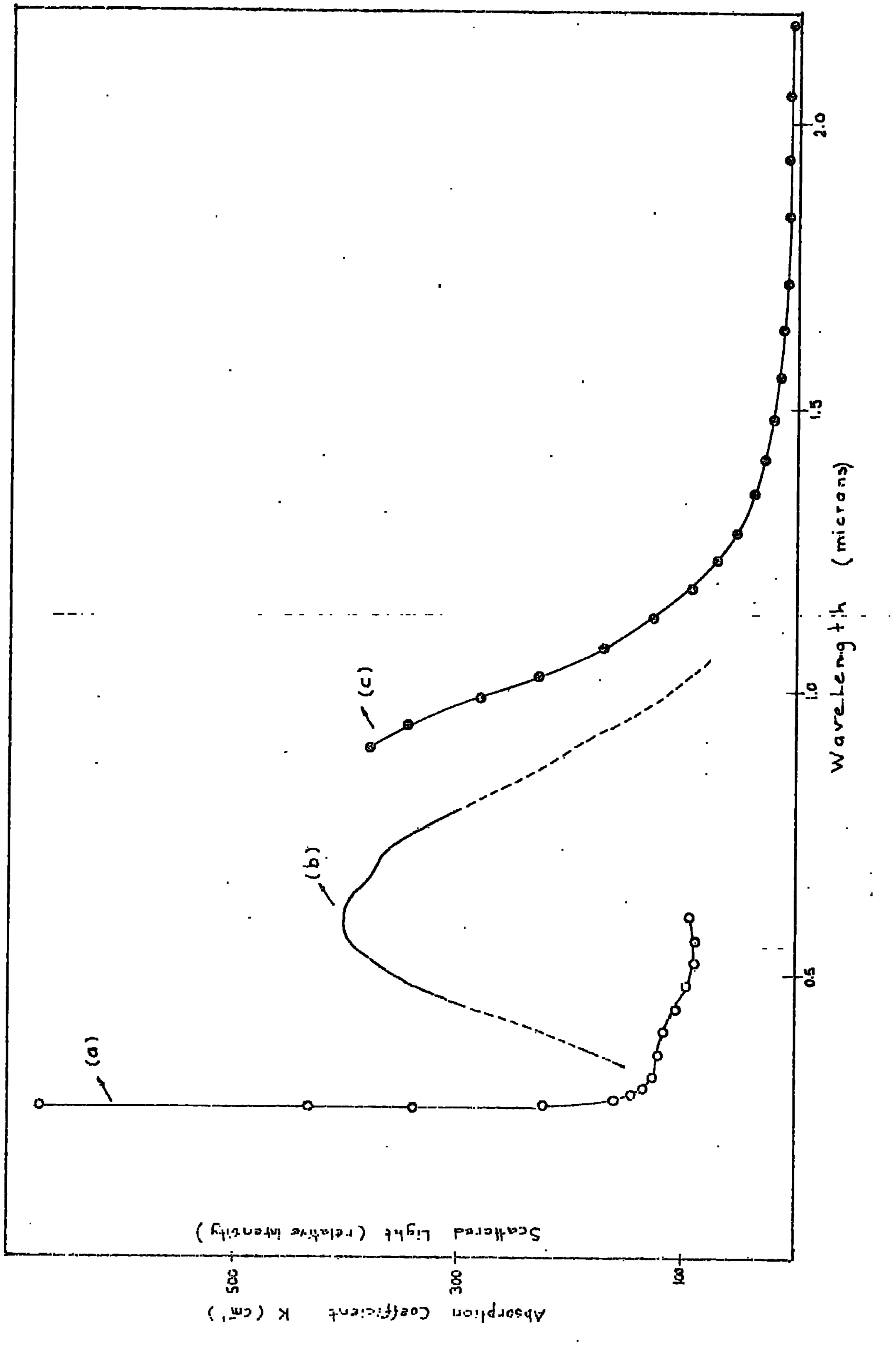
(a)
(b)
(c)
Wavelength (microns)
0.5
1.0
1.5
2.0
Absorption Coefficient K (cm^{-1})
500
300
100
Scattered Light (relative intensity)

scattering curve (b) also increased towards the longer wavelength side. The validity of this explanation depends on the magnitude of the scattered intensity. Time has not permitted this to be measured yet but the integrating sphere method of Bastin et al. (1959) would form the basis of the experiment.

APPENDICES

APPENDIX - 1

Lattice Parameters

X-Ray diffraction photographs were obtained with a 11.4 cm Debye-Schrerrer camera on a Phillips diffraction unit using Cu Kα radiation with a Ni filter.

Single phase cubic fluorite-type structures were observed for both compositions of (8 and 12 m/o) YSZ in as grown, current blackened, oxygen heated and vacuum reduced specimens.

The lattice parameters were observed by measuring diffraction lines with $2\theta > 115^{\circ}$. Results were computed for both (λ_1) and (λ_2) components with the computer programme (written by M. C. George, M.Sc., Department of Geology, University of Durham) based on the Nelson and Riley extrapolation and the least squares method. This included standard deviations in the final result.

8 m/o YSZ: (as grown)

crystal	Lattice parameters
S10	$a(\lambda 1) = 5.1392 \pm 0.0002$ A°
"	$a(\lambda 2) = 5.1392 \pm 0.0008$ A°
1A2(2)	$a(\lambda 1) = 5.1386 \pm 0.0008$ A°
"	$a(\lambda 2) = 5.1387 \pm 0.0017$ A°
1A3	$a(\lambda 1) = 5.1373 \pm 0.0006$ A°
"	$a(\lambda 2) = 5.1368 \pm 0.0009$ A°
	$a(\text{average}) = 5.138 \pm 0.001$ A°

Unit cell size calculation by hand for the as grown crystal 1A3 is

$a = 5.139$ A°

12 m/o YSZ (as grown)

crystal	Lattice parameters
2A1	$a(\lambda 1) = 5.1487 \pm 0.0009$ A°
"	$a(\lambda 2) = 5.1484 \pm 0.0013$ A°
	$a(\text{average}) = 5.1485 \pm 0.001$ A°

Calculation by hand (same crystal)

$a = 5.149$ A°

8 m/o YSZ: (baked in oxygen)

Conditions: 175 cc/m, for 4 hrs., at 960^oC.

colour: white and grey

crystals Lattice parameters

S7(1) (White): $a(\lambda 1) = 5.1403 \pm 0.0006$ A^o
" " $a(\lambda 2) = 5.1401 \pm 0.0020$ A^o

S7(2) (Grey) $a(\lambda 1) = 5.1397 \pm 0.0010$ A^o
" " $a(\lambda 2) = 5.1402 \pm 0.0010$ A^o

$a(\text{average}) = 5.140 \pm 0.002$ A^o

Result: 0.03% change does not seem reliable increase according to the standard deviation ± 0.002 A^o.

12 m/o YSZ (baked in oxygen)

Conditions: 75 cc/m. for 3.5 hrs. at 1085^oC

Colour: white.

crystal Lattice parameters

S9(1) $a(\lambda 1) = 5.1486 \pm 0.0006$ A^o
$a(\lambda 2) = 5.1493 \pm 0.0014$ A^o

$a(\text{average}) = 5.1489 \pm 0.0014$ A^o

Result: no change observed.

8 m/o YSZ (vacuum reduced)

Conditions: 1-2 x 10^{-4} mmHg, at 2200±20°C for 2.5 hrs. (heated in air at 800°C for 6 hrs. before vacuum reduction).

Colour: grey

crystal Lattice parameters

S2(1)

$a(\lambda 1) = 5.1384 \pm 0.0012$ A°
$a(\lambda 2) = 5.1378 \pm 0.0007$ A°

$a(\text{average}) = 5.1381 \pm 0.0012$ A°

Result: no change observed on lattice parameter.

12 m/o YSZ (vacuum reduced)

Conditions: exactly same as S2(1)

crystal Lattice parameter

S12

$a(\lambda 1) = 5.1488 \pm 0.0011$ A°
$a(\lambda 2) = 5.1486 \pm 0.0003$ A°

$a(\text{average}) = 5.1487 \pm 0.0011$ A°

Result: no change observed on lattice parameter.

8 m/o YSZ (current blackened)

Crystal: 1A14j

Conditions: 1A/cm^2 at 800^{o}C for 35 hrs. in argon gas flow.

Lattice parameters

$a(\lambda 1) = 5.1399 \pm 0.0013\ A^{o}$
$a(\lambda 2) = 5.1398 \pm 0.0010\ A^{o}$

$a(\text{average}) = 5.1399 \pm 0.0013\ A$

Crystal: 1A14h

Conditions: 5A/cm^2, 15 m, 800^{o}C, in argon.

Lattice parameters

$a(\lambda 1) = 5.1397 \pm 0.0008\ A^{o}$
$a(\lambda 2) = 5.1396 \pm 0.0007\ A^{o}$

$a(\text{average}) = 5.1396 \pm 0.0008\ A^{o}$

Result: No noticeable changes have been observed on the lattice parameters due to the current blackening.

Conclusions

1. For both 8 and 12 m/o YSZ no noticeable unit cell size change has been observed among the as grown, current blackened, vacuum reduced or oxygen heat treated within the accuracy limit of ± 0.001 A°.
2. For both types of crystals, no extra lines due to the zirconium metal have ever been observed, although this had been seen for heavily blackened polycrystal line yttria-zirconia by Casselton and Watson (1968c). The addition of zirconium metal to 8 m/o YSZ showed that Zr diffraction lines can only be noticeable for more than 5% of zirconium metal. This shows that the X-Ray diffraction technique is not very sensitive. We have also been limited by the highest value of current density that could be applied.
3. The lattice parameters for both two crystals are in good agreement with the values obtained by Duwez et.al. (1951), Strickler and Carlson (1965), J. Lefevre (1963), Baukal and Scheidegger (1968).

APPENDIX - 2

TABLE-1

A large piece of black opaque as grown 12 mole % YSZ crystal was cut into three parts which were heated in oxygen, argon and vacuum. The conditions are given below.

Sample	Oxygen (cc/m)	Argon (cc/m)	Vacuum	Temp. (^{o}C)	Time (hr.)	Result
2A4	(as grown)					black, opaque
2A4.a	75			1075	3.5 + 1	white, translucent
2A4.b		75		1075	3.5 + 1	black, yellowish transparent
2A4.c			✓	1075	3.5 + 1	black, slightly transparent
2A4.aa			(75)	1045	3.5 + 00	white → grey
2A4.ab		(75)		900	2.5 + 00	white → white

Results:

It is postulated that the colour centres causing the crystals' opaqueness are affected by the heat treatment in the following way.

(a) Heating in oxygen causes oxygen atoms to fill the vacancies, as oxygen ions, at the expense of trapped electrons (F-centres).

(b) Heating in argon indicates that a very small amount of oxygen, (leaking through the furnace or in the argon gas itself) causes an effect similar to (a) which may be explained as a very early stage of whitening.

(c) Heating in vacuum shows that temperature alone is not effective for the release of centres or alternately that it is effective but the electrons released are trapped again.

The tendency of the sample to absorb oxygen at high temperatures may also be indicative of the excess of oxygen vacancies initially present.

(d) Fifth sample shows that a previously oxygen heated whitened sample (2A4.a) is heated in vacuum, its colour becomes grey, indicating that the newly created colour centres may be attributed to the following reaction.

$$O^{2-} \longrightarrow O_2 + 2e$$

The electrons would be trapped in the vacancies which were left by O^{2-} leaving the sample as O_2. This explanation also fits the EPR results.

TABLE-2

A piece of black opaque as grown 8 mole % YSZ crystal was cut into three, and heated in oxygen, argon and vacuum. The conditions are given below.

Sample	Oxygen (cc/m)	Argon (cc/m)	Vacuum	Temp. (^oC)	Time (hr)	Result (colour etc.)
1A1	(as grown)					black, opaque
1A1.a	75			1075	3.5 +1	white, translucent
1A1.b		75		1075	3.5 +1	black yellowish transparent
1A1.c				1075	3.5 +1	black, slightly transparent

Result:

The statements given for Table-1 of 12 mole % YSZ are also valid for this 8 mole % YSZ.-

TABLE-3

The heat treatment of 12 mole % YSZ samples in oxygen.

Sample	Oxygen (cc/m)	Temp. (^{o}C)	Time (hrs.)	Result
2A2	(As grown)			black, opaque
2A2.a	25	545	2.5 + 1	" "
2A2.aa	"	675	$2.5 + \infty^{(*)}$	" "
2A2.ab	"	800	" ∞	" "
2A2.ac	"	900	" ∞	" "
2A2.ad	"	7000	" ∞	white, blackish part slightly transparent
2A2.ae	"	1050	" ∞	White + grey translucent
2A2.af	"	1100	" ∞	Completely white translucent
2A2.ag	"	1080	" ∞ -	White + grey translucent

(*) indicates that the samples were left under the oxygen flow in the furnace until the temperature dropped to the room temperature after the heat treatment.

Result: for a fixed oxygen flow rate and time, the samples (approx. 50 mm^3) were completely whitened at temperature 1100 ^{o}C.

APPENDIX - 3

For the conversion between the cavity scale and the magnet turntable, the following formula was derived. According to the Figure (App.1) and the symbols given below, it can be seen that:

C_1, C_2: Two crystal face readings e.g. $[100]$ on the cavity scale.

D_1, D_2: Two datum line readings on the cavity scale.

Mo : The magnet scale reading when the datum line is parallel to the pole pieces. Experimentally it was found $0^{\circ} \mp 1$.

M : The magnet scale reading when the magnetic field is in the required crystal direction.

The cavity scale increases counter clockwise while magnet scale increases in the reverse way.

The angle, θ_o, between the crystal orientation and the magnetic field is:

$$\theta_o = 90^{\circ} - (D_1 - C_1)$$

Any angle, θ_1, deviation of the magnetic field from $[100]$ direction, counter clockwise will result:

$$\theta_1 = \theta_o - (M - Mo)$$

$$\theta_1 = 90 - (D_1 - C_1) - (M - Mo)$$

for the required ($[100] + \theta_1$) crystal direction, the magnet reading M becomes, substituting Mo = 0

$$M(\theta_1) = 90 - \theta_1 - (D_1 - C_1)$$

in the special case of 90 - θ_1 becomes zero, the magnet lies along ($[100]$ + 90°) another fourfold direction, so M$[100]$

$$M\,[100] = -(D_1 - C_1)$$

In fact, in practice, we used a kind of "alignment aid" based on this formula in order to make the calculations easily and quicker.

Fig. (App - 1)

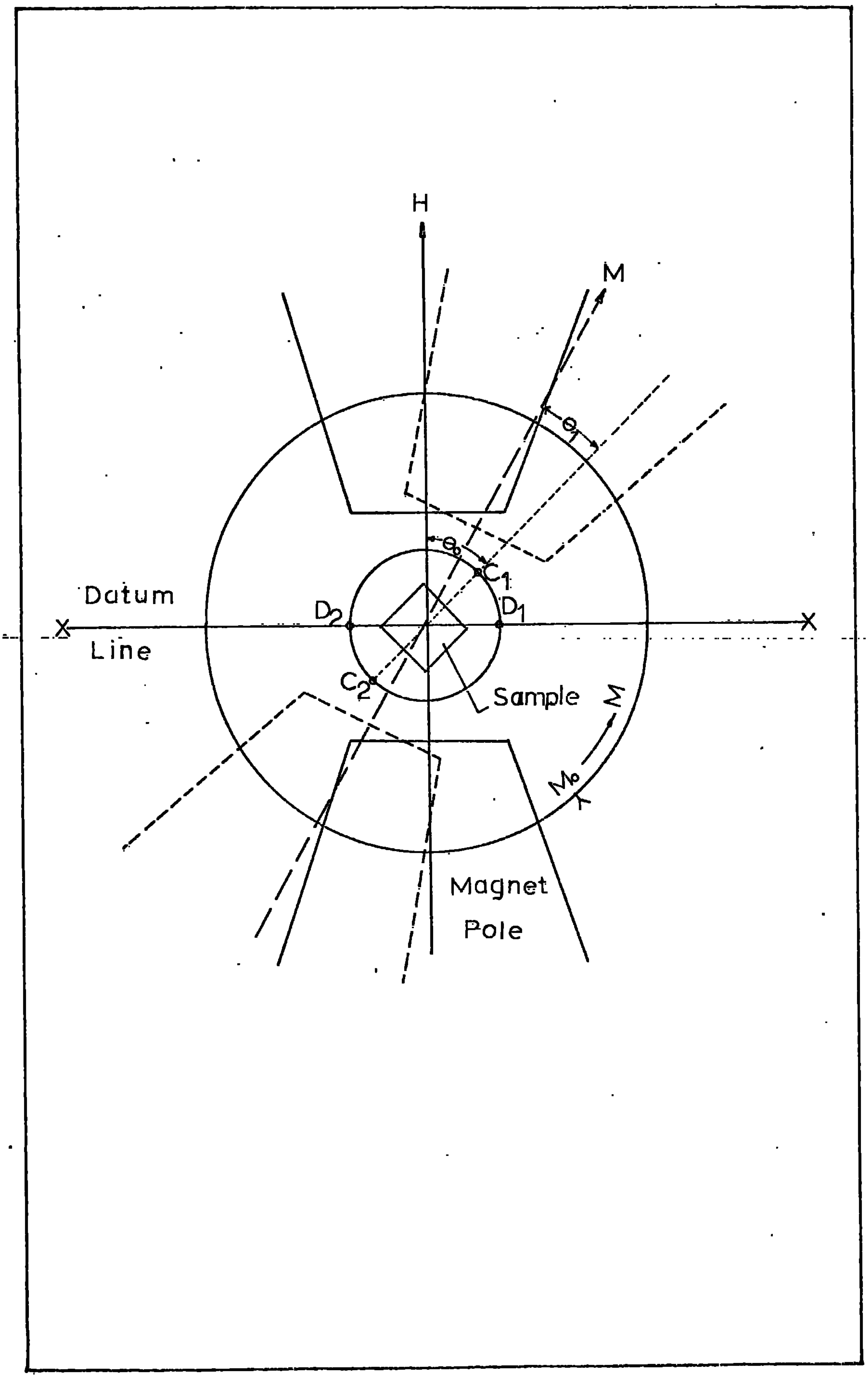
H
M
θ_1
θ_0
C_1
D_1
D_2
C_2
X
X
Datum
Line
Sample
M
M_0
Magnet
Pole

APPENDIX - 4

The magnetic field value B_D, at which DPPH EPR was observed, was calculated according to the equ.(1.8) and using the following numerical values

$$B_D = h\nu / g_D \beta$$

$h = 6.6252 \times 10^{-34}$ joule. sec

$\nu = 35.5$ GHz resonance frequency

$g_D = 2.0036$ (Holden et.al.(1950))

$\beta = 9.2732 \times 10^{-24}$ Joule. $m^2.Wb^{-1}$

The magnetic field B_D is for DPPH line is found to be

$$B_D = 1.2559 \text{ Tesla.}$$

If equ.(1.8) is written twice for both DPPH and the sample rearrangement gives, for the same frequency value the g-value of the sample

$$\text{i.e. } g = g_D/(1 + (B - B_D)/B_D)$$

where;

g: The g-factor to be calculated of the sample for several magnetic field orientations.

$B - B_D$: The magnetic field difference between the sample and the DPPH resonances.

In the following four tables the numerical details of the anisotropic type-A lines are given with the calculated g-values of as grown (1A10a) in two perpendicular (100)-planes.

TABLE-1

The g-values of the upper curve of Fig.(3.4)

Crystal orientation	Field orientation	$(B - B_D)$		g
		inches	mT	values
	130	4	45.2	1.935
	140	3.2	36.2	1.948
	150	2.65	29.9	1.957
	155	2.5	28.3	1.960
	160	2.4	27.1	1.962
[110]	165	2.3	26.0	1.963
	170	2.35	26.6	1.963
	180	2.65	29.9	1.957
	190	3.25	36.7	1.947
	200	3.9	44.1	1.936
[100]	210	4.8	54.2	1.921
	220	4.0	45.2	1.935

TABLE-2

The g-values of the lower curve of Fig.(3.4)

Crystal orientation	Field orientation	$(B_S - B_D)$		g
		inches	mT	values
	130	5.8	65.5	1.905
	140	6.3	71.2	1.897
	150	6.8	76.8	1.889
	160	7.4	83.6	1.879
[110]	165	7.2	81.4	1.883
	180	7.1	80.2	1.884
	190	6.4	72.3	1.895
	200	5.9	66.7	1.903
[100]	210	4.8	54.2	1.921
	220	4.0	45.2	1.935

TABLE-3

The g-values of the upper curve of Fig.(3.5)

Crystal orientation	Field orientation	$(B_S - B_D)$		g values
		inches	mT	
[010]	320	6.3	71.2	1.897
	330	5.6	63.3	1.908
	340	4.5	50.8	1.926
	350	4.1	46.3	1.933
	360	3.4	38.4	1.945
[011]	10	2.75	31.1	1.957
	20	2.3	26.0	1.963
	30	2.3	26.0	1.963
	40	2.4	27.1	1.962
	50	2.7	30.5	1.957
	60	3.15	35.6	1.949

TABLE-4

The g-values of the lower curve of Fig.(3.5)

Crystal orientation	Field orientation	$(B_S - B_D)$		g values
		inches	mT	
[010]	320	2.8	31.6	1.955
	330	3.5	39.6	1.943
	340	4.55	51.4	1.926
	350	5.1	57.6	1.916
	360	5.7	64.4	1.907
[011]	10	6.7	72.3	1.891
	20	6.8	76.8	1.889
	30	7.35	82.1	1.880
	40	7.0	79.1	1.886
	50	6.45	72.9	1.895
	60	5.65	63.8	1.907
	70	4.45	50.3	1.927

REFERENCES

REFERENCES

Abragam, A., and Bleaney, B., 1970, *Electron Paramagnetic Resonance of Transition Ions*, (Oxford, Clarendon Press).

______, Pryce, M. H. L., 1951, Proc. Roy. Soc., A205, 135

Ackermann, R. J., and Thorn, R. J., 1964, *Symposium on High Temperature Technology*, (Butterworth)

Adams, S. K., and Casselton, R. E. W., 1970, J. Am. Ceram. Soc., __, 117.

Adler, D., 1968a, *Solid State Physics*, vol.21, Ed. F. Seitz, D. Turnbull (N.Y., Academic Press), p.1.

______, 1968b, Rev. Mod. Phys, 40, 714.

Ahrens, L. H., 1952, Geochimica, et. Cosmoschimica. Acta, 3, 1.

Alper, A. M., 1970, *High Temperature Oxides*, (N.Y., Academic Press)

Al'tschuler, S. A. and Kuzyrev, B. M., 1964, *Electron Paramagnetic Resonance*, Ed. C. P. Poole, Jr. (N.Y., Academic Press)

Anthony, A. M., 1965, C.R. Acad. Sc. Paris, 260, 1936.

Assenheim, H. M., 1966, *Introduction to ESR*, (London, Hilger and Watts Ltd.) p.181, 65.

Barker, W. W., 1967, Material Science and Engineering, 2, 208.

______, Williams, L. S., 1968, J. Australian Ceram. Soc., 4, 1.

Baukal, W., and Scheidegger, 1968, Ber. Deut. Keram. Ges. 45, 611.

Bauerle, J. E., 1969, J. Phys. Chem. Solids, 30, 2657.

______, Hrizo, J., 1969, J. Phys. Chem. Solids., 30, 565.

Baur, E., and Preis, H., 1937, Z. Elektrochem., 43, 727.

Bendoraitis, J. G. and Salomon, R. E. S., 1965, J. Phys. Chem., 69, 3666.

Bethe, H., 1929, Ann. Phys. **3**, 133.

Bevan, D. J. M. et al., 1965, *Rare Earth Research III*, ed. L. Eyring (N.Y., Gordon and Breach)

Blackman, M., 1955, *Handbuch der Physik*, *vol.7*, Ed. S. Flugge (Berlin, Springer Verlag), part 1, p.375.

Bleaney, B., 1951, Phil. Mag., **42**, 441.

_______, O'Brien, M. C. M., 1956, Proc. Phys. Soc., **B69**, 1216.

Bonch Bruevich, V. L., 1966, *The Electronic Theory of Heavily Doped Semiconductors*. (N.Y., Elsevier)

Born, M. and Huang, K., 1954, *Dynamical Theory of Crystal Lattices*, (Oxford,Clarendon Press), p.123.

Bowers, K. D., and Owen, J., 1955, Rept. Progr. Phys, **18**, 204.

Bowring, C. S., Smithard, M. A., Cousins, J. E., 1971, Phys. Stat. Sol.(b), **43**, 625.

Bray, D. J., and Merten, U., 1964, J. Electrochem. Soc., **111**, 447.

Brisse, F., and Knop, O., 1967, Can. J. Chem., **45**, 609.

Bruner, G., and Gradinger, H., 1951, Naturwissenschafter, **38**, 559.

Burton, C., 1967, Unsubmitted M.Sc. Thesis, University of Durham.

Caillet et al., 1968, Rev. Int. Temp. et. Refract., **5**, 173.

Callaway, J., 1964, *Energy Band Theory*, (N.Y., Academic Press)

Casselton, R. E. W., 1968a, *Electricity from MHD*, *Vol.5* (Vienna, I.A.E.A.) p.2951

_______, 1968b, *e.m.f. Measurements in High Temperature System*, Ed. C. B. Alcock (London, Inst. of Mining and Metallurgy)

_______, Watson, M. D. S., 1968c, Science of Ceramics, **4**, 349.

Casselton, R. E. W., 1970, Phys. Stat. Sol. **A2**, 571.

________, Thorp, J. S., Wright, D. A., 1971, Proc. Brit. Ceram. Soc., No.19, 265.

Collongues, R. et al., 1961, Bull. Soc. Chim. France, **1**, 70.

__________, 1965, Bull. Soc. Chim. France, __, 1140.

Conlon, D., and Doyle, W. P., 1965, J. Chem. Phys., **42**, 4315

Cotton, F. A., and Wilkinson, G., 1962, *Advanced Inorganic Chemistry*, (N.Y., Interscience)

Coullough, J. D. and Britton, J. D., 1952, J. Am. Ceram. Soc., **74**, 5225.

Cousins, J. E. and Dupree, R., 1965, Phys. Letters, **19**, 464.

Davis, E. A., and Shaw, R. F., 1970, J. Non-crystalline Solids, **2**, 406.

Davydov, A. S., 1968, Phys. Stat. Sol., **27**, 51.

Dexter, D. L., 1967, Phys. Rev. Lett., **19**, 1383.

Dietzel, A., and Tober, H., 1953, Ber. Deut. Keram. Ges., **30**, 47.

Dirac, P. A. M., 1930, *The Principles of Quantum Mechanics*, (Oxford, Univ. Press).

Dixon, J. M. et al., 1963, J. Electrochem. Soc., **110**, 276.

Dow, J. D., and Redfield, D., 1970, Phys. Rev., **B1**, 3358.

Doyle, W. T., Ingram, D. J. E., Smith, M. J. A., Proc. Phys. Soc., **74**, 540.

Duncan, W., and Schneider, E. E., 1964, *Proc. 7th Conf. on Semiconductors*, (Dunod, Paris) p.1171

Duwez, P., Odell, F. H., 1950, J. Am. Ceram. Soc., **33**, 274.

_____, Odell, F. H., 1951, J. Electrochem. Soc. **98**, 356.

Dyson, F. J., 1955, Phys. Rev., **98**, 349.

Elliott, R. J., 1954, Phys. Rev., **96**, 266.

Falicov, L. M., 1971, Semiconductor - metal and Magnetic Phase Transitions in Transition Metal and Rare Earth Compounds. (Montreal, Canada, MC Hill Summer School on Semiconductors).

Feher, G., and Kip, A. F., 1955, Phys. Rev., 98, 337.

Fisher, W. A., 1970, Z. Phys. Chem. (Frankfurt) 69 (1-2), 11.

Foex, M., and Rouanet, A., 1967, C. R. Acad. Sci. Paris, 264, 947.

Fu-kang Fan, Kuznetsov, A. K. and Keller, E. K., 1962, Izv. Akad. Nauk. SSSR, Otd. Khim. Nauk, No.7, p.1141.

__________, Kuznetsov, A. K. and Keller, E. K., 1963, Izv, Akad. Nauk. SSSR, Otd. Khim. Naum, No.4, p.601.

Geller, R. F. and Yavorsky, P. J., 1945, J. Res. Nat. Bur. Std., 35, 87.

Geusic, J. E. and Brown, L. C., 1958, Phys. Rev., 112, 64.

Gokhshtein, Ya.P., 1970, Teplofiz. Vys.-Temp., 8, 398.

Griffiths, J. S., 1963, The Theory of Transition Metal Ions, (Cambridge), p.365, 379.

Griswold, T. W., Kip, A. F., Kittel, C., 1952, Phys. Rev. 88, 951.

Gueron, M., and Ryter, Ch., 1965, Phys. Rev. Letts, 3, 338.

Guillou, M., Asquiedge, M. Palous, S., 1968, Electricity from MHD, Vol.5 (Vienna, I.A.E.A.)

Heffelfinger, R. E. Blasser, E. R., Henry, E. R., 1964, J. Am. Ceram. Soc., 47, 646.

Hepworth, M. A., and Arthur, G., 1963, M.H.D. Power Generation (London, I.E.E. Conference series, No.4)

Hester, P., 1965, Elements of Inorganic Chemistry, (N.Y., Benjamin Press) table 5.1

Hoch, M., 1964, J. Am. Ceram. Soc., 47, 630.

____, Yoon, H. S., Silberstein, A., 1967, Proc. Brit. Ceram. Soc. No.8, 247.

Holland, B. J., 1966, *Proc. 14. Colloque Ampere*, (Ljublyana) p.468.

Hopfield, J. J., 1968, Comments on Solid State Physics, 1, 16.

Hund, F., 1951, Z. Elektrochem., 55, 363.

____, 1952, Z. Physik. Chem., 199, 142.

____, 1965, Ber. Deut. Keram. Ges., 42, 251.

Jacquin, M., Guillou, M., Millet, J., 1967, C.R. Acad. Sci. Paris, 264, series c, 2101.

Jain, S. C., and Radhakrishna, S., 1968, J. Phys. Soc, Japan, 25, 1618.

Kamimura, M., 1956, J. Phys. Soc. Japan, 11, 1171.

________, 1960, J. Phys. Soc. Japan, 15, 1264.

Karpachev, S. V., and Filyaev, A. T., 1966, Elektrokhimiya, 2, 1330.

Kittel, C., 1966, *Introduction to Solid State Physics, 3rd ed.* (N.Y., John Wiley), p.446.

Kiukkola, K., and Wagner, C., 1957, J. Electrochem. Soc. 104, 379.

Kleitz, M., 1968, *Thesis*, Grenoble University.

Knight, W. D., 1951, *Solid State Phys. Vol.2*, Ed. F. Seitz, D. Turnbull (N.Y., Academic Press)

Kodera, H., 1964, J. Phys. Soc. Japan, 19, 915.

Kotani, M., 1949, J. Phys. Soc. Japan, 4, 293.

______, 1960, Progr. Theor. Phys., Osaka Suppl., No.14, p.1.

Kramers, H. A., 1927, Atti. Congr. Fis. Como., 545.

Kronig, R., 1926, J. Opt. Soc. Am., 12, 547.

Kruse, P. W., McGlauchlin, L. D., McQuistan, R.B., 1963, *Elements of Infrared Technology* (N.Y., John Wiley), p.139.

Kubo, R., 1962, J. Phys. Soc. Japan., 17, 975.

Lanyon, H. P. D., 1961, Phys. Rev., 130, 134.

Lefevre, J., 1963, Ann. Chem. 8 (1-2), 117.

Levy, R. A., 1956, Phys. Rev., 102, 31.

Lewis, R. B. and Carver, T. R., 1964, Phys. Rev. Letters, 12, 695.

Loup, J. P. Mihailovic, Z., Morvan, P., 1965, C.R. Acad. Sci. Paris, 261, 109.

Low, W., 1962, Solid State Physics, Suppl.2, Ed. F. Seitz, D. Turnbull (N.Y. Academic Press), p.170.

___, Offenbacher, E. J., 1965, Solid State Phys. Vol.17, Ed. F. Seitz, D. Turnbull, (N.Y., Academic Press), p.135.

Mahr, H., 1963, Phys. Rev. 132, 1880.

Markham, J. J., 1966, Solid State Physics, Suppl.8, Ed. F. Seitz, D. Turnbull, (N.Y., Academic Press), p.261

Matamura, O., and Koga, H., 1963, J. Phys. Soc. Japan, 18, Suppl.2, 312.

McClure, D. S., 1959, Solid State Physics Vol.9, Ed. F. Seitz, D. Turnbull (N.Y., Academic Press), p.428.

McLean, T. P., 1960, Progress in Semiconductors 5, 53.

Methfessel, S., and Mattis, D., 1969., Handbuch der Physik, 18A.

Mie, G., 1908, Ann. d. Physik (4), 25, 377.

Morin, F. J., 1958, Bell. Syst. Tech. J., 37, 1047.

Moss, T. S., 1959, Optical Properties of Semiconductors (London, Butterworth)

Mott, N. F., and Gurney, R. W., 1948, Electronic Processes in Ionic Crystals (Oxford, Clarendon Press)

Nerst, W., 1900, Z. Elektrochem., 6, 41.

O'Connor, J. R. and Chen, J. H., 1963, Phys. Rev., 130, 1790

Olsen, A. L., La Baw, K. B. and Nichols, L. W., 1964, J. Opt. Soc. Am., 54, 813.

Orton, J. W., 1959, Rept. Progr. Phys., 22, 204.

Pace, N. G. et al., 1969, J. Material Science, 4, 1106.

Pake, G. E., 1962, Paramagnetic Resonance (N.Y., Benjamin)

Pauling, L., 1927, J. Am. Ceram. Soc., 49, 763.

Pryce, M. H. L., 1950, Phys. Rev., 80, 1107.

Rabi, I. I., 1937, Phys. Rev., 51, 652.

_____, Ramsey, N. F., Schwinger, J., 1954, Rev. Mod. Phys., 26, 167.

Rach, G., 1942a, Phys. Rev., 61, 186.

_____, 1942b, Phys. Rev., 62, 438.

_____, 1943, Phys. Rev., 63, 367.

Redfield, D., 1965, Phys. Rev., 140, A2056.

Roberts, L. E. J., and Markin, T. L., 1967, Proc. Brit. Ceram. Soc. No.8, 201.

Roth, R. S., 1956, J. Res. Natl. Bur. Std., No.1, p.17.

Ruff, O., and Ebert, F., 1929, Z. Anorg. Allgem. Chem., 180, 19.

Ryschkewitch, E., 1960, Oxide Ceramics, (N.Y., Academic Press), p.350 etc.

Savostianowa, M., 1930, Z. Physik, 64, 262.

Sawyer, J., Hyde, B., and Eyring, L., 1965, Bull. Soc. Chim. France, 1190.

Schmidt, J., and Solomon, I., 1966, J. Am. Appl. Phys. 37, 3719.

Schottky, W., 1935, Wiss. Veroffentl. Siemens-Werken, 41, 1.

Schultz, S., and Latham, C., 1965, Phys. Rev. Lett. 15, 148.

Schultz, S., and Shanabarter, M. R., 1966, Phys. Rev. Letters, 16, 178.

Slichter, C. P., 1963, Principles of Magnetic Resonance, (N.Y., Harper and Row)

Smith, D. K., 1966, J. Am. Ceram. Soc., 49, 625.

Strattron, J. A., 1941, *Electromagnetic Theory*, (N.Y., McGraw Hill)

Strickler, D. W., and Carlson, W. G., 1964, J. Am. Ceram. Soc., 47, 122.

__________, ______________, 1965, J. Am. Ceram. Soc. 48, 286.

Sugano, S., 1960, Progr. Theor. Phys. Osaka. Suppl. No.14, p.66.

Tanabe, Y., 1960, Progr. Theor. Phys., Osaka. Supple. No.14, p.17.

Tauc, J., 1966, *The Optical Properties of Solids* Proc. Int. School of Physics Enrico Fermi, Course 34, Ed. J. Tauc (N.Y., Academic Press), p.63.

____, 1969, *Optical Properties of Solids*, Ed. F. Abeles (Amsterdam, North Holland)

Toyazawa, Y., 1964, Tech. Rept. of the Inst. for Solid State Physics (Univ. of Tokyo, Ser.A, No.119)

Urbach~~, F., 1953, Phys. Rev., 93~~, 1324.

Van Vleck, J. H., 1932, *Electric and Magnetic Susceptibilities* (Oxford Univ. Press)

__________, 1935, J. Chem. Phys., 3, 807.

__________, 1940, Phys. Rev. 57, 426.

Vescial, F., Vander Ven. N. S. and Shumacher, R. T., 1964, Phys. Rev., 134, A1286.

Wagner, C., 1943, Naturw., 31, 265.

Walsh, W. M., Rupp, L. W., and Schmidt, P. H., 1966a, Phys. Rev., 142, 414.

__________, __________, ____________, 1966b, Phys. Rev. Letters, 16, 181.

Weber, B. C., 1964, Aerospace Research Labs., Rept. ARL-64-205.

Weckersheim, K. A., and Lefever, R. A., 1961, J. Opt. Soc. Am., 51, 1147.

Weininger, J. L., and Zemany, P. D., 1954, J. Chem. Phys., 22, 1469.

Weissbart, J., and Ruka, R., 1962, J. Electrochem. Soc., 109, 723.

Yafet, Y., 1963, *Solid State Physics, Vol.14*, Ed. F. Seitz, D. Turnbull (N.Y., Academic Press), p.1.

Zavoisky, E. J., 1945, J. Phys. (USSR), 9, 211.